MESOSCALE TRANSDUCTION SYSTEMS AND APPLICATIONS TO ENERGY HARVESTING ONBOARD FLYING INSECTS

A Dissertation

Presented to the Faculty of the Graduate School

of Cornell University

In Partial Fulfillment of the Requirements for the Degree of

Doctor of Philosophy

by

Timothy Reissman

January 2013

© 2013 Timothy Reissman

MESOSCALE TRANSDUCTION SYSTEMS AND APPLICATIONS TO ENERGY HARVESTING ONBOARD FLYING INSECTS

Timothy Reissman, Ph. D.

Cornell University 2013

We begin this dissertation first by defining the mesoscale as the realm of feature sizes that span from the single micron to the centimeter range. The motivation for focusing on the mesoscale is that in terms of today's power applications, such geometric scale is required in order to allow for sufficient energy transduction within the larger devices that they serve. Thus, by further developing the models and fabrication techniques within the mesoscale, this collection of works aims to achieve a direct and immediate impact on advancing the state of the art within these facets of transduction technology.

The first chapter of this dissertation describes the derivation and first known experimental validation of a generalized analytical method for predicting the performance of a piezoelectric vibration energy harvesting devices with geometric discontinuities. Here we adapt the transfer matrix method to incorporate the direct piezoelectric effect, thereby predicting the electromechanical response of such devices. The significance of this work is that it a means to progress away from geometry specific solutions to a generalized analytical approach for design.

The next chapter describes the results of a fan-folded, i.e. discontinuous geometry, piezoelectric structure attached to a *Manduca sexta* hawkmoth. Here the design criteria are developed through empirical studies of insect's abilities and by the power requirements of the proposed miniaturized onboard devices. The significance of this work is that it provides the first known successful demonstration of in-situ harnessing of free, flapping flight on an insect capable of

powering technology such as radio transmissions.

The third chapter details the use of single-level lithography to simplify the microfabrication of stacked inductors used in power converter technology. By using such a technique and increasing the scale to the mesoscale range, the inductance of such devices can be increased to the necessary micro-Henry inductance level.

The fourth chapter describes the full conduction, convection, and radiation modeling of the classic thermal micro-actuator. Within this model, we extend beyond the conventional conduction-only approach to yield more accurate models and transfer functions needed for advancing controls applications in microscale technology.

BIOGRAPHICAL SKETCH

Timothy Reissman received a Bachelor's of Science degree in Mechanical Engineering from Cornell University in 2002. As an undergraduate, he was president of Cornell's American Society of Mechanical Engineers chapter and a researcher in the Cornell University Harley Davidson Laboratory, supervised by Professor Albert George. As a researcher, he designed experiments for measuring heat transfer properties of air-cooled engines. He also participated in the Formula SAE open-wheeled racecar team during his junior and senior years. During that time, he learned important hands-on skills in mechanical design and manufacturing, as well as taking on roles within leadership and management. As a result of his efforts, he led his team to two world championships within the Formula SAE competition.

Upon graduating, Timothy continued into the Master of Engineering program at Cornell University. After spending one semester within the Laboratory for Intelligent Machine Systems, directed by Prof. Ephrahim Garcia, he applied for and was admitted into the Master of Science program. During the same year, he worked on a multitude of projects such as engine-driven hexapods, meso-scale energetics, and compliant micro-scale flexures. For funding, he performed control design for Moog Aerospace, Inc and Active Signal Technology, Inc executing the first successful implementation of piezoelectric-driven pilot valves for hydraulics. In addition, he was a teaching assistant for a number of classes, including Mechatronics, System Dynamics, Vibration, and Mechanical Synthesis, in which he was awarded an honorable mention for "Best Teaching Assistant." In 2006, he applied for and was accepted into the Ph. D. program, becoming a researcher within the DARPA Hybrid-Insect MEMS program. Applying his background in micro-systems and electromechanical modeling, he conducted research on harvesting energy from the vibratory body motion induced by the flapping flight of insects. In January of 2008, he received his Master's of Science degree for his research entitled "Meso-Scale Transduction Techniques for Mechatronic Systems."

Subsequently, Timothy continued his research within the DARPA funded program focusing further on vibration-based energy harvesting. By 2010, he had co-authored two journal articles on transient charging techniques for piezoelectric energy harvesting systems and two more articles on micro-scale sensing techniques. The following chapters within his dissertation are his first-authored papers, including two articles towards novel techniques in energy harvesting and two more papers on micro-scale modeling.

ACKNOWLEDGMENTS

I want to thank my wife Megan, my parents, and friends for all their love and encouragement during this journey. My lab mates Adam Wickenheiser, Justin Manzo, and John Dietl for providing a friendly and fun, albeit sometimes too fun, atmosphere at work. My cycling team mates, especially Matt Latyszonek, Flint Richardson, Justin Rice, Luat Vuong, and Brian Lawney for introducing me to competitive biking and providing me with a healthy outlet for releasing life's stress. The Sibley School for supporting me through Teaching Assistantships when research money was tight. The DARPA HI-MEMS program for releasing me from teaching obligations and allowing me to focus on research, especially towards the end of my degree. My constant collaborators, Nic Lobontiu and Robert MacCurdy, for adding to the content of my work with your parallel skillsets. My committee members, Prof. David Erickson and Prof. Robert Gilmour, for providing helpful comments at my exams and on my thesis work. Last, but not least, I'd like to thank my advisor Prof. Ephrahim Garcia, for believing that I could be a Ph. D. and providing me with the opportunity to pursue my goals.

TABLE OF CONTENTS

LIST OF FIGURES

CHAPTER 1

CHAPTER 2

CHAPTER 3

CHAPTER 4

LIST OF TABLES

CHAPTER 1

CLOSED FORM ELECTROMECHANICAL MODELING AND EXPERIMENTAL VALIDATION OF PIEZOELECTRIC VIBRATION-BASED ENERGY HARVESTING STRUCTURES WITH NON-UNIFORM GEOMETRIES[1]

1. Abstract

Many single and multi-beam piezoelectric vibration-based energy harvesting (pVEH) structures appearing in the literature require custom analytical or finite-element models to compute their eigensolutions and electromechanical coupling effects. In this paper, we develop the use of the transfer matrix method to derive a general procedure for finding closed form electromechanical solutions of pVEH structures with uniform or non-uniform geometries composed of chain-like topologies. Moreover we aim to strengthen the widespread acceptance of this generalized method by providing the first experimental validation with respect to predicting the natural frequencies, mode shapes, and voltage frequency responses for a multitude of common pVEH structures, including partial length unimorphs, partial length bimorphs, with and without tip masses, as well as multi-beam devices. To summarize, our method first solves for the mechanical eigensolutions by decomposing such pVEH structures along their lengths into two general component types: (1) Euler-Bernoulli prismatic beam segments with constant material properties and (2) point-wise discontinuities with optional lumped inertias or masses at the end of each prismatic beam segment. For each component type, we develop transfer matrices in order to

---

[1] From Reissman, T., Wickenheiser, A. M., and Garcia, E., "Closed Form Electromechanical Modeling and Experimental Validation of Piezoelectric Vibration-based Energy Harvesting Structures with Non-Uniform Geometries"; manuscript originally submitted to *Smart Materials and Structures* through the Institute of Physics. This work was supported by the DARPA HIMEMS program.

formulate a computationally friendly linear algebraic approach to describe the distribution of the structure's state parameters along its length, making the procedure analogous to the state transition matrix of a linear system. Furthermore we limit the size of the required state vector to only four parameters: deflection, slope, shear force, and bending moment, by having the analysis consist of only bending modes with zero and 180 degree bend discontinuities. While acknowledged as a set of design constraints, we note that they are reasonable ones as many common pVEH structures lie within this subset. Having then solved the eigensolutions in a generalized closed form, the second part of the method incorporates the electromechanical effects and considers the case of the base excitation problem, or vibration source. To complete the analysis, we derive the decoupled modal equations in order to predict the electromechanical equations of motion, which are shown to be a generalization of existing analytical pVEH models. Thus within this work we both derive the method fully and validate showing less than 2.3 percent deviation in results from experiments investigating the first and second resonances. The magnitude of such work is to provide an acceptable approach for general analysis of many common pVEH structures within their linear regime.

2. Introduction

The last decade has seen a surge in the literature concerning renewable energy sources, specifically for remote, low-power applications. The field known as energy harvesting focuses on developing devices that convert available energy from the ambient environment into a useable electrical form [1-3]. The appeal of energy harvesting is greatest for long-term applications where it offers a potential financial advantage over wired and battery operated systems by reducing or eliminating maintenance costs. Although a variety of ambient energy sources are

available, vibration-based energy harvesting has received a significant amount of attention due to its ability to be implemented on man-made structures, where vibration is omnipresent [1]. A common transduction type for this renewable energy source has been piezoelectrics, which convert mechanical deformation into electrical energy via constitutive relations known as the direct piezoelectric effect.

For piezoelectric vibration-based energy harvesting (pVEH) devices, the piezoelectric materials are typically laminated onto a flexible structure. The energy harvested is determined by mechanically exciting the composite structure with the ambient vibration and measuring the resultant voltage output from the piezoelectric material across a resistive load, or stored into a capacitive device [2]. To make this technology competitive with present day battery technology, pVEH researchers have utilized micro-fabrication techniques to develop designs with small form factors to match or be smaller than many common battery sizes [3]. However, the small beam lengths associated with micro-fabricated pVEH devices have typically resulted in resonant frequencies well above the range of available ambient vibration, which in turn yield extremely low energy conversion efficiencies at the common ambient frequencies [4-7]. To achieve lower resonant frequencies while maintaining small form factors, a variety of design features including continuously variable cross-sections [8-10], variation of the ratio of the tip mass to beam mass [10], discontinuous geometries in the form of partial-length piezoelectric laminates, i.e piezoelectric patches [11-12], and multi-beam structures [13-14] have been explored. Despite the wide variety of designs, no single analytic method has been given and experimentally validated for predicting the eigensolutions and electromechanical behavior of such pVEH structures. Thus, the literature is bombarded with custom analytic and finite-element models specific to each design, making comparisons and geometric optimization difficult.

Scanning over the pVEH literature, we observed that two common analytic approaches are used to simulate pVEH devices: (1) lumped parameter models, typically single degree-of-freedom [15-16] and (2) distributed parameter models, or multiple degrees-of-freedom [17-20]. Lumped parameter methods provide simple and effective models when vibrating near a single resonant frequency, but are difficult to use in the physical design phase because their coefficients are typically determined experimentally. Distributed parameter models are more accurate, predicting geometric effects such as charge cancellation, and can be extended to include arbitrary degrees-of-freedom. The caveat however is that these models are typically much more complex and are designed for a specific geometry.

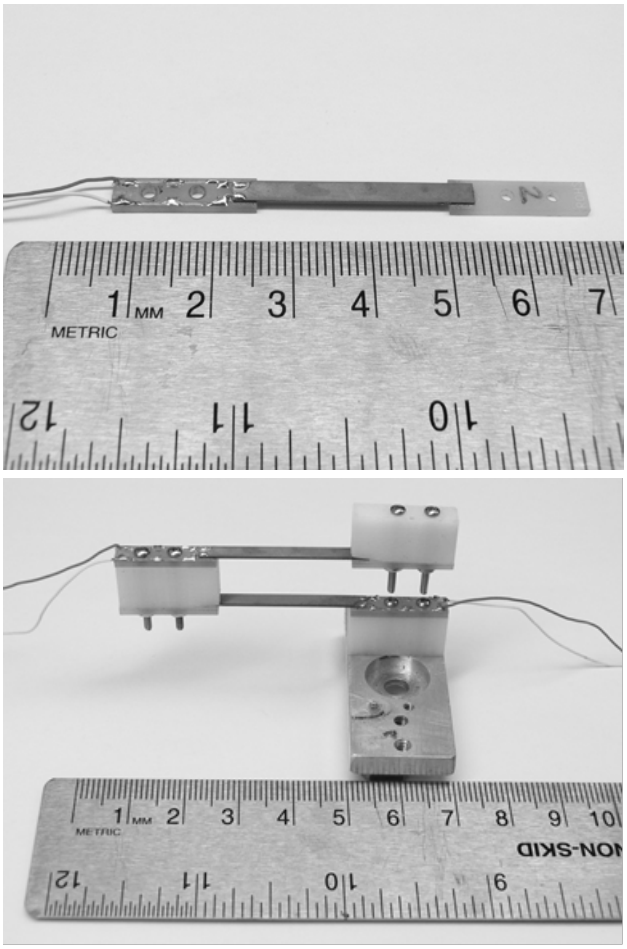

Figure 1.1: Top: Partial length bimorph device (Piezo Sys: D220-A4-103). Bottom: Multi-beam "folded-back" pVEH structure with ABS plastic and metal fastener masses. Note that both designs have predominant chain-like topologies with multiple geometric discontinuities.

In this article, we aim to broaden the versatility of distributed parameter models beyond geometry specific solutions by providing a derivation and an experimental electromechanical validation of a linear algebraic approach which allows for a generalized analysis of pVEH structures with chain-like topologies that consist of: varying cross-sectional geometry, single or multiple beam elements, and multiple discontinuities, including lumped masses. Examples of such pVEH devices can be seen in Figure 1.1 and are among some of the most commonly

implemented: partial length unimorphs, partial length bimorphs, with and without tip masses, as well as multi-beam devices. To summarize, the method is derived from an extension of the classical transfer matrix method (TMM) for purely mechanical structures [21] and an existing distributed-parameter pVEH model for prismatic, Euler-Bernoulli beam structural members [18]. Using these two models, we thus assume two major conditions: (1) the pVEH structure has a chain-like topology and (2) Euler-Bernoulli beam theory can be applied when decomposing the structure into prismatic beam elements. Here, we note that while similar TMM-based approaches have been previously used in the pVEH literature to calculate the eigensolutions, such as for torsional mode structures [14] or bending mode structures with arbitrary bend angles between elements [22], this article separates itself by contributing in two major ways: (1) its main importance is in it provides the first experimental validation of this method in terms of confirming beyond the natural frequencies to also comparing the predicted mode shapes and the electromechanical effect, or voltage output, generated from the piezoelectric laminates and (2) it shows a simplified analysis for those bending mode devices which can be modeled using only transverse deflections.

The paper itself is composed into three major sections. First we derive the equations of motion for a purely mechanical structure with non-uniform geometries using the TMM, initially ignoring any electromechanical effects of the piezoelectric material, i.e. assuming a short-circuit condition. Within this section we detail the TMM discretization of each pVEH structure into two basic components: (1) Euler-Bernoulli prismatic beam segments and (2) discontinuities with lumped masses and inertias. Formulations for two separate geometric discontinuities are explored for both the zero degree bends, or inline, and 180 degree bends, or folded-back cases, with each one representing the necessary chain-link topology for implementing the classical

TMM. By limiting the bend angles to these two common cases, the influence of axial deflections can be ignored and so our mechanical analysis can be reduced to solving for only four state variables. Moving forward, we combine the basic components in the order in which they appear along their length, in order to derive state transition matrices for each, which are then used to describe the distribution of the states. Using this linear algebraic approach, the combined sequential components represent a generalized approach for setting up the eigenvalue problem for such pVEH structures. Within the next section, we examine the typical pVEH cantilever boundary condition, so as to illustrate the eigensolutions from this matrix formulation and compare natural frequency solutions with pVEH devices in the literature. The 'implementation of the TMM for pVEH' section incorporates the TMM solutions found previously into a partial differential equation model that includes the linearized piezoelectric constitutive equations. This section is critical for pVEH analysis as it enables the solution of the coupled electromechanical dynamics. Finally the 'validation' section presents comparisons of our TMM-based results with experiments of multiple pVEH configurations containing zero and 180 degree bends, for not only the natural frequencies but also the mode shapes and voltage free response frequencies.

3. Transfer Matrix Method

3.1 Overview of TMM

The transfer matrix method (TMM) is introduced in order to familiarize the reader with this analysis form [21]. This method is used to calculate the natural frequencies and mode shapes, i.e. the eigensolutions, for piecewise continuous structures with chain-like topologies.

The structures depicted in Figure 1.2 serve as representative examples of pVEH designs that can be solved for their eigensolutions and electrical power output by implementation of our method. For example, evaluating the structures in Figure 1.2 we can segment each structure into a combination of 3 sets of prismatic beams with lengths L_i and discontinuities with lumped masses m_i connected to the tip of each beam segment. By discretizing the discontinuous structures into uniform components, we use the TMM as a means to separate these structures into two basic components: (1) segments of prismatic, beams and (2) discontinuities at the tips of each segment. It should be noted here that the reference frame sets the "base" of each segment as the end closest to the host structure, whereas the "tip' is the end furthest. Within this work, we analyze the closed-form solutions for two specific types of geometric discontinuities: those occurring along a straight, inline structure with zero degree bends and those occurring at 180 degree bends, as in the case of a folded-back structure. For either type, we allow for the optional presence of a lumped mass at each discontinuity.

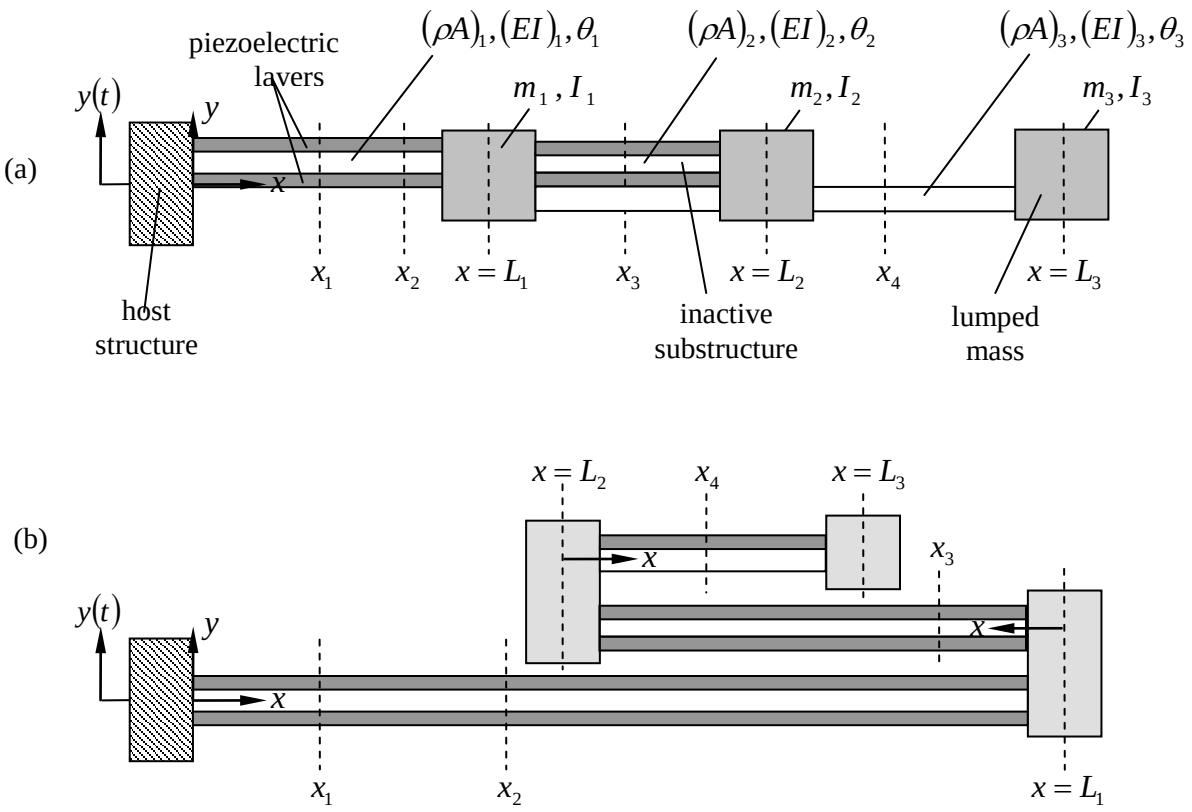

Figure 1.2: Layout and geometric parameters of example chain-like topology structures: (a) inline (b) folded-back. Note that the *x*-direction is defined as continuing along the length of the structure.

To begin, each beam segment is assumed to have constant geometric and material properties; however different segments may have different properties. Additionally, each segment may have a different number and arrangement of piezoelectric and substructure layering, as shown in Figure 1.2. We let $w(x,t)$ be the transverse, *y*-axis, deflection of the piecewise discontinuous structure, measured relative to the host structure position. Since the deflection is governed by Euler-Bernoulli beam theory, i.e. a partial differential equation, the method of separation of variables is adopted to decompose the deflection into spatial and temporal components

$$w(x,t) = \sum_{r=1}^{\infty} \eta_r(t)\phi_r(x) \tag{1}$$

where $\eta_r(t)$ is the r^{th} modal displacement and $\phi_r(x)$ is the r^{th} mode shape function. We henceforth drop the subscript r for simplicity, since the following discussion applies to any mode.

As will be further discussed in *Section 3.2 "Derivation of the Field Matrix,"* the Euler-Bernoulli beam theory used to describe the spatial response results in a fourth order equation, which requires four independent states to solve for the variation of ϕ with respect to x. These four states are the mode shape itself ϕ, its slope $d\phi/dx$, the internal bending moment M, and the internal shear force V. We assemble these four states into a 4 × 1 column, defined as the state vector $\mathbf{z}$.

$$\mathbf{z} = \begin{bmatrix} \phi & d\phi/dx & M & V \end{bmatrix}^T \tag{2}$$

From this state vector, a 4 × 4 linear system of the form

$$d\mathbf{z}/\mathrm{d}x = \mathbf{A}(x)\mathbf{z}(x) \tag{3}$$

is later derived. Applying the general solution to Eq. (3), we use the state transition matrix Φ to relate the state vectors at any two points along the structure.

$$\mathbf{z}(x_2) = \mathbf{\Phi}(x_2, x_1)\mathbf{z}(x_1) \tag{4}$$

At this point, the usefulness of the TMM becomes clear. Consider the problem of relating states between points x_1 and x_2 and between points x_3 and x_4, for either structure shown in Figure 2. In the next two sections, we derive state transition matrices for each beam segment, called *field*

matrices, and for each discontinuity, with or without a lumped mass, called *point matrices*. Denoting the field matrix for the j^{th} beam segment F_j and the point matrix for the j^{th} discontinuity $\mathbf{P}_j$, we can use the semigroup property of state transition matrices to write Eq. (4) as

$$\mathbf{z}(x_2) = \mathbf{P}_1\mathbf{F}_1(x_2 - x_1)\mathbf{z}(x_1) \tag{5a}$$

between points x_1 and x_2, where P_1 is the identity matrix since no discontinuity exists at the tip of this segment, and

$$\mathbf{z}(x_4) = \mathbf{P}_3\mathbf{F}_3(x_4 - L_2)\mathbf{P}_2\mathbf{F}_2(L_2 - x_3)\mathbf{z}(x_3) \tag{5b}$$

between points x_3 and x_4, where P_2 represents the lumped mass discontinuity at the tip of the beam segment from x_3 to L_2 and P_3 is the identity matrix since no discontinuity exists at the tip of L_2 to x_4. We note here that Eq. (5a-b) display a useful computational feature of the TMM: no matter how many beam segments and discontinuities are present along the structure, the problem never grows beyond the initial state transition matrix size, in our case a 4 × 4 linear system.

3.2 Derivation of the Field Matrix

To derive the transition matrix between two points along a uniform beam segment without the presence of a discontinuity, Euler-Bernoulli beam theory is used and electromechanical coupling effects are initially ignored. This omittance of coupling effects is equivalent to the assumption of Euler-Bernoulli beam mode shapes, a prevalent simplification appearing in the literature for single segment beams [16,18,19]. With these assumptions, we apply a balance of transverse

forces and moments on a differential element of an Euler-Bernoulli beam segment *j*, as depicted Figure 1.3.

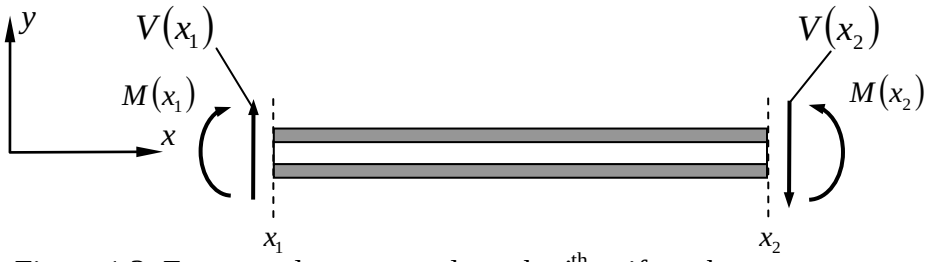

Figure 1.3: Forces and moments along the j^{th} uniform beam segment.

The transverse force balance for the free vibration of the differential element of beam segment *j* yields

$$\frac{\partial V(x,t)}{\partial x} = -(\rho A)_j \frac{\partial^2 w(x,t)}{\partial t^2} \tag{6}$$

where $(\rho A)_j$ is the mass per unit length of beam segment *j* (see Appendix A). A balance of moments on the same element gives

$$\frac{dM(x,t)}{dx} = -V(x,t) \tag{7}$$

By the Euler-Bernoulli slender beam and small deflection assumptions, we relate the bending moment to the stiffness of the element by

$$M(x,t) = (EI)_j \frac{\partial^2 w(x,t)}{\partial x^2} \tag{8}$$

where $(EI)_j$ is the effective bending stiffness of beam segment *j* (see Appendix). Thus, Eq. (6-8) represent the equations of motion for the beam segment *j*.

At this point, we apply Eq. (1) and assume harmonic motion. Each mode shape has a natural frequency ω associated with it. Here we once again drop the *r* subscript. With these substitutions, we rewrite Eq. (6) with relation to the mode shape.

$$\frac{dV(x)}{dx} = -(\rho A)_j \omega^2 \phi(x) \tag{9}$$

We continue in the same manner rewriting Eq. (7-8) with relation to the mode shape, which gives us the following four expressions for the linear system

$$\frac{d}{dx}\underbrace{\begin{bmatrix} \phi \\ d\phi/dx \\ M \\ V \end{bmatrix}}_{\mathbf{z}} = \underbrace{\begin{bmatrix} 0 & 1 & 0 & 0 \\ 0 & 0 & \frac{1}{(EI)_j} & 0 \\ 0 & 0 & 0 & -1 \\ -(\rho A)_j \omega^2 & 0 & 0 & 0 \end{bmatrix}}_{\mathbf{A}_j} \cdot \underbrace{\begin{bmatrix} \phi \\ d\phi/dx \\ M \\ V \end{bmatrix}}_{\mathbf{z}} \tag{10}$$

which is the same matrix form as in Eq. (3). Note that within beam segment *j*, the cross sections are constant along the length, which results in a constant state matrix $\mathbf{A}_j$ in Eq. (10).

Applying the general solution to Eq. (10) from linear system theory, we can relate the states at any two points within the beam segment *j* using

$$\mathbf{z}(x_2) = e^{\mathbf{A}_j \Delta x}\mathbf{z}(x_1) \equiv \mathbf{F}_j(\Delta x)\mathbf{z}(x_1) \tag{11}$$

where $\mathbf{F}_j$ is referred to as the field matrix for beam segment *j*. Therefore, if $\mathbf{F}_j$ is known, the variation in the state vector at different positions within a single beam segment can be found.

To find an explicit formula for $\mathbf{F}_j$, two steps are needed. First, we use the Cayley-Hamilton Theorem to write the field matrix $\mathbf{F}_j$ in polynomial form

$$\mathrm{F}_\mathrm{j}(\Delta x) = c_0\mathbf{I} + c_1(\mathbf{A}_\mathrm{j}\Delta x) + c_2(\mathbf{A}_\mathrm{j}\Delta x)^2 + c_3(\mathbf{A}_\mathrm{j}\Delta x)^3 \tag{12}$$

where $\mathbf{I}$ is the identity matrix and the coefficients $\{c_0, c_1, c_2, c_3\}_j$ are those of the characteristic polynomial of $\mathbf{A}_\mathrm{j}\Delta x$, which is found from the equation

$$\left|\lambda\mathbf{I} - \mathbf{A}_\mathrm{j}\Delta x\right| = \begin{vmatrix} \lambda & -\Delta x & 0 & 0 \\ 0 & \lambda & \dfrac{-\Delta x}{(EI)_j} & 0 \\ 0 & 0 & \lambda & \Delta x \\ (\rho A)_j\,\omega^2\Delta x & 0 & 0 & \lambda \end{vmatrix} = \lambda^4 - \left(\beta_j^4\Delta x\right)^4 = 0 \tag{13}$$

Here we define β_j as the eigenvalues per unit beam length of segment *j*, given by

$$\beta_j^4 = \frac{(\rho A)_j\,\omega^2}{(EI)_j} \tag{14}$$

which indeed match the eigenvalues of an Euler-Bernoulli beam [23]. The terms $\{c_0, c_1, c_2, c_3\}_j$ are functions of the eigenvalues and can be found by substituting $\lambda = \pm\beta_j\Delta x, \pm i\beta_j\Delta x$ into Eq. (12) in place of $\mathbf{A}_\mathrm{j}\Delta x$, resulting in

$$
\begin{aligned}
c_0 &= \frac{1}{2}\left[\cosh\left(\beta_j \Delta x\right) + \cos\left(\beta_j \Delta x\right)\right] \\
c_1 &= \frac{1}{2\left(\beta_j \Delta x\right)}\left[\sinh\left(\beta_j \Delta x\right) + \sin\left(\beta_j \Delta x\right)\right] \\
c_2 &= \frac{1}{2\left(\beta_j \Delta x\right)^2}\left[\cosh\left(\beta_j \Delta x\right) - \cos\left(\beta_j \Delta x\right)\right] \\
c_3 &= \frac{1}{2\left(\beta_j \Delta x\right)^3}\left[\sinh\left(\beta_j \Delta x\right) - \sin\left(\beta_j \Delta x\right)\right]
\end{aligned}
\tag{15}
$$

Substituting Eq. (15) and the definition of $\mathbf{A}_j$ into Eq. (12), we derive an explicit formula for the field matrix $\mathbf{F}_j$:

$$
\mathbf{F}_j\left(\Delta x\right) = \begin{bmatrix}
c_0 & \Delta x c_1 & \dfrac{\left(\Delta x\right)^2}{\left(EI\right)_j} c_2 & \dfrac{-\left(\Delta x\right)^3}{\left(EI\right)_j} c_3 \\
\dfrac{\left(\Delta x\right)^3 \left(\rho A\right)_j \omega^2}{\left(EI\right)_j} c_3 & c_0 & \dfrac{\Delta x}{\left(EI\right)_j} c_1 & \dfrac{-\left(\Delta x\right)^2}{\left(EI\right)_j} c_2 \\
\left(\Delta x\right)^2 \left(\rho A\right)_j \omega^2 c_2 & \left(\Delta x\right)^3 \left(\rho A\right)_j \omega^2 c_3 & c_0 & -\Delta x c_1 \\
-\left(\Delta x\right)\left(\rho A\right)_j \omega^2 c_1 & -\left(\Delta x\right)^2 \left(\rho A\right)_j \omega^2 c_2 & \dfrac{-\left(\Delta x\right)^3 \left(\rho A\right)_j \omega^2}{\left(EI\right)_j} c_3 & c_0
\end{bmatrix}
\tag{16}
$$

which gives the variation of the state vector along the length of a single, uniform geometry beam segment according to Eq. (11). A use of this matrix for that purpose is seen in Eq. (5a).

3.3 Derivation of the General Point Matrix

With the mechanical response of the uniform beam segments defined using the field matrix, we now define the general point matrix $\mathbf{P}$, which accounts for the geometric discontinuities and lumped masses at the tips of uniform beam segments. Referring to Figure 1.4, we apply a free-body diagram at the discontinuity $x = L_j$. Here we assume that at the point $x = L_j$ a point mass exists, which has the properties of a mass m_j and rotary inertia I_j. We further assume that the mass is infinitesimal in size and that the forces and moments can be evaluated at $x = L_j -$ and $x = L_j +$, meaning approaching $x = L_j$ from the left and from the right, respectively.

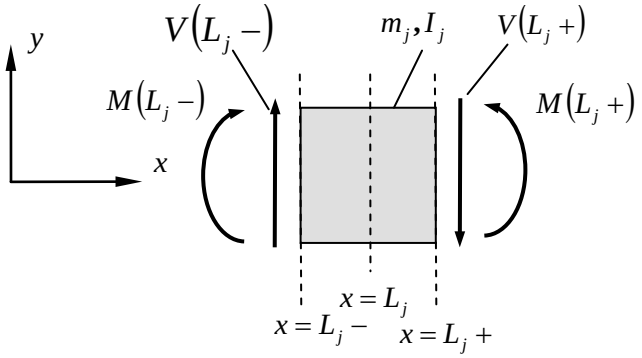

Figure 1.4: Forces and moments on a lumped mass located at $x = L_j$.

We assume the lumped mass to be non-deformable and so the mode shape deflection at the end of the adjoining beam segment is continuous across the lumped mass and equal in sign for zero degree, inline, discontinuities.

$$\phi(L_j +) = \phi(L_j -) \tag{17a}$$

However, since we define the *x*-direction as following continuously along the length of the structure, see Figure 1.2, the deflection is reversed in sign for the case of 180 degree bends.

$$\phi\left(L_j+\right)=-\phi\left(L_j-\right) \tag{17b}$$

To compensate for either the zero or 180 degree case, we define the deflection as the following

$$\phi\left(L_j+\right)=\phi\left(L_j-\right)\cos\left(\theta_j\right) \tag{17c}$$

,where θ_j is either zero or 180 degrees depending on the discontinuity present.

Continuing with this same reference frame, we define the mode shape slope as continuous and retaining the same sign, regardless of whether the discontinuity has a zero or 180 degree bend.

$$d\phi\left(L_j+\right)/dx = d\phi\left(L_j-\right)/dx \tag{18}$$

Unlike Eqs. (17-18), due to the lumped inertia, the shear forces and bending moments are not continuous. Applying a balance of moments on the lumped mass yields

$$M\left(L_j+\right)=-I_j\omega^2\frac{d\phi\left(L_j\right)}{dx}+M\left(L_j-\right) \tag{19}$$

for both types of discontinuities, while a balance of forces gives

$$V\left(L_j+\right)=-m_j\omega^2\phi\left(L_j\right)+V\left(L_j-\right) \tag{20a}$$

for the zero degree bend and

$$V\left(L_j+\right)=m_j\omega^2\phi\left(L_j\right)-V\left(L_j-\right) \tag{20b}$$

for the 180 degree bend, which is simply a sign reversal of the Eq. (20a). Again, to compensate for both cases, we define the shear force balance as

$$V\left(L_j+\right)=m_j\omega^2\phi\left(L_j\right)\cos\left(\theta_j\right)+V\left(L_j-\right)\cos\left(\theta_j\right) \tag{20c}$$

Assembling Eq. (17-20) together yields

$$\underbrace{\begin{bmatrix} \phi(L_j+) \\ d\phi(L_j+)/dx \\ M(L_j+) \\ V(L_j+) \end{bmatrix}}_{\mathbf{z}(L_j+)} = \underbrace{\begin{bmatrix} \cos(\theta_j) & 0 & 0 & 0 \\ 0 & 1 & 0 & 0 \\ 0 & -I_{m,j}\omega^2 & 1 & 0 \\ m_j\omega^2\cos(\theta_j) & 0 & 0 & \cos(\theta_j) \end{bmatrix}}_{\mathbf{P}_j} \underbrace{\begin{bmatrix} \phi(L_j-) \\ d\phi(L_j-)/dx \\ M(L_j-) \\ V(L_j-) \end{bmatrix}}_{\mathbf{z}(L_j-)} \tag{21}$$

which is a linear system of the form

$$\mathbf{z}(L_j+) = \mathbf{P}_j \mathbf{z}(L_j-) \tag{22}$$

and describes the general point matrix $\mathbf{P}_j$ of the j^{th} discontinuity, with a zero or 180 degree bend. To validate the components of this matrix, we compare our results with that of previous studies using the TMM for evaluating discontinuities with zero [24-25] and 180 degree bends [26-27]. At this point, it should be noted though that in none of these previous studies were the effects of a lumped mass evaluated. Therefore, to make an equal comparison we set $m_j = I_j = 0$ for these cases. In applying the values to Eq. (21), our general point matrix $\mathbf{P}_j$ reduces to the identity matrix for zero degree bends and to the diagonal $\{-1,1,1,-1\}$ for 180 degree bends, which matches exactly with the previously derived point matrices. Thus, our general point matrix for both types of discontinuities while providing the off-diagonal terms when in the presence of lumped masses, correcting for the mass's translational and angular inertia.

3.4 Composition Using the State Transition Matrix

As discussed in *Section 3.1*, we can use the state transition matrix $\mathbf{\Phi}(x_2, x_1)$ to relate the states of the system between any two points along the beam, recall Eq. (4). Depending on the locations of x_1 and x_2, the transition matrix is, in general, expressible as a product of field and point matrices, as illustrated by Eqs. (5a-b). To construct the state transition matrix for the entire

structure $\mathbf{\Phi}(L_n,0)$, we employ the semigroup property and form a successive matrix multiplication of all the field and point matrix pairs for each segmented section from one end of the structure $x=0$ to the other end $x=L_n$:

$$\mathbf{\Phi}(L_n,0)=\prod_{j=1}^{N}\mathbf{P}_{n\text{-}j+1}\mathbf{F}_{n\text{-}j+1}\left(L_{n-j+1}-L_{N-j}\right) \tag{23}$$

where n is the total number of beam segments used to describe the TMM. From this equation, our reasoning for defining the *x*-direction continuously along the structure's length is necessary in order to apply the semigroup property. Using Eq. (23) we can formulate the closed-form solutions for describing the four states for any point along a discontinuous structure with a chain-like topology as the following:

$$\begin{bmatrix}\phi(L_n)\\ d\phi(L_n)/dx\\ M(L_n)\\ V(L_n)\end{bmatrix}=\mathbf{\Phi}(L_n,0)\begin{bmatrix}\phi(0)\\ d\phi(0)/dx\\ M(0)\\ V(0)\end{bmatrix} \tag{24}$$

Here we show that the state transition matrix always remains four-by-four in size regardless of the number of field and point matrix pairs. This compact, linear algebra form proves to be quite helpful in analyzing the eigensolutions, we will show next.

4. Closed-form Eigensolutions

4.1 Determining Structural Natural Frequencies

At this point, we note that the natural frequency ω is still unknown; thus we cannot fully evaluate $\mathbf{\Phi}(L_n,0)$. However, we can use the boundary conditions at the ends of the structure to provide known values for the states at those locations. For example, if we examine the widely-

used cantilever, or "fixed-free", configuration of pVEH devices, the following four states are known at the boundary conditions:

$$\phi(0) = d\phi(0)/dx = 0 \qquad \text{(fixed condition)} \qquad (25a)$$

$$M(L_N) = V(L_N) = 0 \qquad \text{(free condition)} \qquad (25b)$$

Applying these boundary conditions to Eq. (24), we now have four equations and four unknowns, which we can use to solve for the structure's natural frequencies. Thus, by using the TMM, this matrix representation avoids needing the solutions of the state vector at intermediate points along the structure in order to solve for the structure's natural frequencies.

Using the cantilever configuration as an example to show the full solution, we substitute Eq. (25) into Eq. (24) and examining the 3rd and 4th equations of the resulting linear system find

$$\begin{bmatrix} 0 \\ 0 \end{bmatrix} = \begin{bmatrix} [\mathbf{\Phi}(L_n,0)]_{3,3} & [\mathbf{\Phi}(L_n,0)]_{3,4} \\ [\mathbf{\Phi}(L_n,0)]_{4,3} & [\mathbf{\Phi}(L_n,0)]_{4,4} \end{bmatrix} \begin{bmatrix} M(0) \\ V(0) \end{bmatrix} \qquad (26)$$

where $[\mathbf{\Phi}(L_n,0)]_{i,j}$ is the i, j component of the entire structure's state transition matrix $\mathbf{\Phi}(L_n,0)$ from Eq. (23). Using Eq. (26), we construct the characteristic equation as

$$[\mathbf{\Phi}(L_n,0)]_{3,3}[\mathbf{\Phi}(L_n,0)]_{4,4} - [\mathbf{\Phi}(L_n,0)]_{3,4}[\mathbf{\Phi}(L_n,0)]_{4,3} = 0 \qquad (27)$$

which we can then use to solve for the cantilever structure's natural frequencies ω, and hence, the conditions for the existence of non-trivial solutions to Eq. (26).

4.2 Piece-wise Continuous Mode Shapes

With the natural frequencies known, we compute the piece-wise continuous mode shapes and their slopes by evaluating Eq. (4). For the cantilever configuration, we can evaluate between the fixed end and an arbitrary point along the structure

$$\begin{bmatrix} \phi(x) \\ d\phi(x)/dx \\ M(x) \\ V(x) \end{bmatrix} = \mathbf{\Phi}(x,0) \begin{bmatrix} \phi(0) \\ d\phi(0)/dx \\ M(0) \\ V(0) \end{bmatrix} \tag{28}$$

To get the mode shape, we solve for the first equation in Eq. (28), which yields

$$\begin{aligned} \phi(x) &= \left[\mathbf{\Phi}(x,0)\right]_{1,3} M(0) + \left[\mathbf{\Phi}(x,0)\right]_{1,4} V(0) \\ &= \left\{ \left[\mathbf{\Phi}(x,0)\right]_{1,3} \left(\frac{-\left[\mathbf{\Phi}(L_n,0)\right]_{3,4}}{\left[\mathbf{\Phi}(L_n,0)\right]_{3,3}} \right) + \left[\mathbf{\Phi}(x,0)\right]_{1,4} \right\} V(0) \end{aligned} \tag{29a}$$

and to get the slope of the mode shape, we solve for the second equation in Eq. (28) which yields

$$\begin{aligned} d\phi(x)/dx &= \left[\mathbf{\Phi}(x,0)\right]_{2,3} M(0) + \left[\mathbf{\Phi}(x,0)\right]_{2,4} V(0) \\ &= \left\{ \left[\mathbf{\Phi}(x,0)\right]_{2,3} \left(\frac{-\left[\mathbf{\Phi}(L_n,0)\right]_{3,4}}{\left[\mathbf{\Phi}(L_n,0)\right]_{3,3}} \right) + \left[\mathbf{\Phi}(x,0)\right]_{2,4} \right\} V(0) \end{aligned} \tag{29b}$$

In Eqs. (29a-b), we do not retain the scaling factor $V(0)$, instead we rescale the mode shapes in order to satisfy the appropriate orthogonality conditions, as will be discussed in the *Section 5.1 "Modal Decoupling."*

Lastly, within the next section we show the expanded terms of the TMM analysis for a single cantilevered beam with a tip mass to verify that this method does indeed yield the correct eigensolutions from the matrix composition form.

4.3 Solution Comparison – Single Cantilever Beam with a Tip Mass

Here we show the TMM-based approach presented thus far collapses to the well-established modal solution derived directly from the boundary conditions. In this 'single cantilever beam with a tip mass' example, we construct the structure's state transition matrix using Eq. (23) as the product of one field matrix with a beam segment of length L_1, and one point matrix at $x = L_1$ with a zero degree bend and a tip mass, which gives us the compact form $\mathbf{\Phi}(L_1,0) = \mathbf{P}_1\mathbf{F}_1(L_1)$. Next, we calculate the eigenvalues by expanding out the structure's state transition matrix elements for Eq. (26), which give:

$$\begin{aligned}
\left[\mathbf{\Phi}(L_1,0)\right]_{3,3} &= c_0(L_1) \\
\left[\mathbf{\Phi}(L_1,0)\right]_{3,4} &= -L_1 c_1(L_1) \\
\left[\mathbf{\Phi}(L_1,0)\right]_{4,3} &= -\frac{m\omega^2 L_1^2}{(EI)_{eff}} c_2(L_1) - \frac{(\rho A)_{eff}\,\omega^2 L_1^3}{(EI)_{eff}} c_3(L_1) \\
\left[\mathbf{\Phi}(L_1,0)\right]_{4,4} &= \frac{m\omega^2 L_1^3}{(EI)_{eff}} c_3(L_1) + c_0(L_1)
\end{aligned} \tag{30}$$

We then evaluate the characteristic equation according to Eq. (27) and let $L_1 = L$ to get:

$$1 + \cosh(\beta L)\cos(\beta L) - \frac{m}{(\rho A)_{ef}\,L}(\beta L)\left[\cosh(\beta L)\sin(\beta L) - \sinh(\beta L)\cos(\beta L)\right] \tag{31}$$

which does indeed represent the eigenvalues of a cantilevered beam with a tip mass.

To confirm the mode shapes, we expand two more matrix elements of $\mathbf{\Phi}(L_1,0)$ starting at the fixed end, $x = 0$, and extending to any arbitrary point x along the beam:

$$\begin{aligned}\left[\mathbf{\Phi}(x,0)\right]_{1,4} &= \frac{-x^3}{(EI)_{eff}} c_3 \\ \left[\mathbf{\Phi}(x,0)\right]_{1,3} &= \frac{x^2}{(EI)_{eff}} c_2\end{aligned} \tag{32}$$

Substituting the expanded terms from Eqs. (30,32) into into Eq. (29a), we get the mode shape:

$$\begin{aligned}\phi(x) = &\frac{1}{2\beta^2(EI)_{eff}}\left[\cosh(\beta x) - \cos(\beta x)\right] \\ &- \frac{1}{2\beta^2(EI)_{eff}} \frac{\sinh(\beta L) - \sin(\beta L) + \frac{m}{(\rho A)_{eff} L}(\beta L)\left[\cosh(\beta L) - \cos(\beta L)\right]}{\cosh(\beta L) + \cos(\beta L) + \frac{m}{(\rho A)_{eff} L}(\beta L)\left[\sinh(\beta L) - \sin(\beta L)\right]}\left[\sinh(\beta x) - \cos(\beta x)\right]\end{aligned} \tag{33}$$

which, scaling factor aside, is the mode shape of a cantilevered beam with a tip mass.

Thus, this section has shown that the TMM formulation yields the known eigensolutions for a cantilevered beam with a tip mass and does so by evaluating the product of one field transfer matrix and one point transfer matrix. Other closed-form solutions, for example a tip mass with rotary inertia or an offset tip mass [28], can also be recovered by using a more complex point transfer matrix at the tip. Conversely, the solution for a cantilevered beam with no tip mass can be obtained from Eqs. (31,33) by setting $m = 0$.

In conclusion, the main advantage of the TMM is its generality and simple matrix format, which regardless of the number of geometric discontinuities can solve for the eigensolutions of complex, chain-like structures. In the next section, we show how to implement these

eigensolutions into an existing distributed parameter model for pVEH devices in order to determine the electrical output for discontinuous, chain-like designs.

5. Incorporating Electromechanical Coupling

5.1 Modal Decoupling

After the natural frequencies and mode shapes have been computed using the TMM based on the free response of the purely mechanical equations, we introduce the piezoelectric effects and the external forcing due to the base excitation, or vibration source, into the equations of motion for each segmented section. We then derive the frequency response by decoupling the partial differential equations into a system of ordinary differential equations for each mode. We concatenate these resultant coupled equations of motion for each segmented section, so as to apply them to everywhere along the structure. The following represents the general case of segmented beam structures for the discontinuous structures discussed thus far

$$\sum_{j=1}^{n}\left\{\left[\left(\rho A\right)_j\frac{\partial^2 w(x,t)}{\partial t^2}+\left(EI\right)_j\frac{\partial^4 w(x,t)}{\partial x^4}\right]\left[H\left(x-L_{j-1}\right)-H\left(x-L_j\right)\right]+\right.$$
$$\left.\vartheta_j\left[\frac{d\delta\left(x-L_{j-1}\right)}{dx}-\frac{d\delta\left(x-L_j\right)}{dx}\right]v(t)\right\}=f(x,t) \tag{34a}$$

$$f(x,t)=-\frac{d^2y(t)}{dt^2}\sum_{j=1}^{n}\left(\left\{\left(\rho A\right)_j\right\}\left[H\left(x-L_{j-1}\right)-H\left(x-L_j\right)\right]+m_j\delta\left(x-L_j\right)\cos\left(\sum_{i=0}^{j-1}\theta_i\right)\right) \tag{34b}$$

$$q(t) = \sum_{j=1}^{n} \vartheta_j \left[\left. \frac{\partial w(x,t)}{\partial x} \right|_{x=L_j} - \left. \frac{\partial w(x,t)}{\partial x} \right|_{x=L_{j-1}} \right] - \sum_{j=1}^{n} C_j v(t) \tag{34c}$$

, where $H(\cdot)$ is the Heaviside step function, $\delta(\cdot)$ is the Dirac delta function, and ϑ_j is the electromechanical coupling coefficient of the j^{th} beam segment, while C_j is the net clamped capacitance of the j^{th} beam segment. See Appendix for calculations of the effective (ρA), the effective (EI), ϑ and C for beam segments with unimorph and bimorph piezoelectric laminate configurations. Incorporating the base excitation into Eq. (34a), defined as the external forcing $f(x,t)$, we introduce the inertial loading in the vertical y-direction. Expanding out the forcing term in Eq. (34b), we account for the lumped masses and discontinuities, i.e. zero or 180 degree bends, in order to represent the applied transverse force along the entire structure. Implementing the piezoelectric electromechanical coupling, we introduce two additional states, the voltage output $v(t)$ across the output terminals of the pVEH structure and the electrical charge $q(t)$, which is dependent upon the external circuit applied to the pVEH structure.

Since typically pVEH literature utilizes orthonormal mode shapes in their solutions of Eq. (34a), we take the time here to show how to employ the orthogonality conditions onto TMM eigensolutions. Applying the modal decomposition from Eq. (1) into the free response of Eq. (34a) and assuming a sinusoidal time with response under a short-circuit condition, i.e. $v(t) \equiv 0$, yields

$$\omega_r^2 \sum_{j=1}^{n} \left\{ \left[(\rho A)_j \phi_r(x) \right] \left[H(x - L_{j-1}) - H(x - L_j) \right] \right\} = \sum_{j=1}^{n} \left\{ \left[(EI)_j \frac{\partial^4 \phi_r(x)}{\partial x^4} \right] \left[H(x - L_{j-1}) - H(x - L_j) \right] \right\} \tag{35}$$

for each r^{th} mode shape. Multiplying Eq. (24) by $\phi_s(x)$ and integrating from $x=0$ to $x=L_n$, we get the orthogonality conditions for the mode shapes by applying the boundary conditions at the ends of the structure and the intermediate conditions across each discontinuity

$$\sum_{j=1}^{n}\left\{\int_{L_{j-1}}^{L_j}(\rho A)_j\phi_r(x)\phi_s(x)dx+m_j\phi_r(L_j-)\phi_s(L_j-)+I_j\left.\frac{d\phi_r(x)}{dx}\right|_{x=L_j}\left.\frac{d\phi_s(x)}{dx}\right|_{x=L_j}\right\}=\delta_{rs} \tag{36}$$

where δ_{rs} is the Kronecker delta. The notation $\phi(L_j-)$ indicates that the mode shape should be evaluated on the side of each discontinuity closer to the $x=0$ coordinate of the structure. The mode shape slopes do not require this distinction since the slope of the structure is continuous at the discontinuities. If the mode shapes are scaled appropriately such that Eq. (36) is satisfied, then automatically

$$\begin{aligned}\sum_{j=1}^{n}(EI)_j\Bigg[&\int_{L_{j-1}}^{L_j}\frac{d^4\phi_r(x)}{dx^4}\phi_s(x)dx-\left.\frac{d^3\phi_r(x)}{dx^3}\right|_{x=L_j-}\left.\frac{d\phi_s(x)}{dx}\right|_{x=L_j-}+\left.\frac{d^3\phi_r(x)}{dx^3}\right|_{x=L_{j-1}+}\left.\frac{d\phi_s(x)}{dx}\right|_{x=L_{j-1}+}\\&+\left.\frac{d^2\phi_r(x)}{dx^2}\right|_{x=L_j-}\left.\frac{d\phi_s(x)}{dx}\right|_{x=L_j-}-\left.\frac{d\phi_r(x)}{dx}\right|_{x=L_{j-1}+}\left.\frac{d\phi_s(x)}{dx}\right|_{x=L_{j-1}+}\Bigg]=\omega_r^2\delta_{rs}\end{aligned} \tag{37}$$

is satisfied, thus decoupling Eq. (34a). Subsequently, we can adopt the TMM natural frequencies and mode shapes into existing pVEH models for evaluating continuous and discontinuous geometric structures.

5.2 Frequency Response Functions

Once the equations of motion are decoupled by mode, we can obtain the frequency response functions (FRFs) of the pVEH structure in a straightforward manner by using the continued assumption of a harmonic base excitation. Substituting the modal expansions from Eq. (1) into Eqs. (34a-c) and applying the orthogonality conditions from Eqs. (36) and (37), we are show the decoupled forms of Eqs. (34a-c) for the r^{th} mode

$$\frac{d^2\eta_r(t)}{dt^2} + 2\zeta_r\omega_r\frac{d\eta_r(t)}{dt} + \omega_r^2\eta_r(t) + \Theta_r v(t) = -(\rho A\gamma)_r\frac{d^2y(t)}{dt^2} \tag{38a}$$

$$\frac{dv(t)}{dt} + \frac{1}{R_l C_0}v(t) = \frac{1}{C_0}\sum_{r=1}^{\infty}\Theta_r\frac{d\eta_r(t)}{dt} \tag{38b}$$

where Eq. (38a) represents the pVEH mechanical equation, in which the modal short circuit frequencies ω_r are equal to the TMM natural frequencies. This can be shown by setting $v(t) \equiv 0$, i.e. the short-circuit condition, which is equivalent to decoupling the electrical dynamics from the mechanical dynamics. Within Eq. (38a), we define the modal electromechanical coupling by a difference of the mode shape slopes

$$\Theta_r = \sum_{j=1}^{n}\vartheta_j\left[\left.\frac{d\phi_r(x)}{dx}\right|_{x=L_j} - \left.\frac{d\phi_r(x)}{dx}\right|_{x=L_{j-1}}\right] \tag{38c}$$

and the modal influence coefficient of the distributed inertial force from Eq. (34b) as

$$(\rho A\gamma)_r = \sum_{j=1}^{n}\left[\int_{L_{j-1}}^{L_j}(\rho A)_j\phi_r(x)dx + m_j\phi_r(L_j -)\right]\cos\left(\sum_{i=0}^{j-1}\theta_i\right) \tag{38d}$$

Note that the modal damping term $2\zeta_r\omega_r\left(d\eta_r(t)/dt\right)$ is commonly added at this point, although the value of the modal damping ratio is usually determined experimentally.

Eq. (38b) represents the electrical equation dynamics, where here we assume the electrical terminals are only across an external resistor R_l. We define the net clamped, i.e. constant strain, capacitance of the piezoelectric material as

$$C_0 = \sum_{j=1}^{n} C_j \tag{38e}$$

in which the circuit's connections to the piezoelectric material are assumed to be configured in parallel so as to simply sum the capacitances of the beam segments. On the right hand side of Eq. (38b), the same Θ_r appearing in Eq. (38a) is used to couple the two modal equations. We note here that only under mass-normalized conditions, i.e. Eq. (36), are these two coupling coefficients equivalent.

To evaluate the FRFs of the pVEH structure, we assume a harmonic base excitation of the form $y(t) = Ye^{i\omega t}$, where $i = \sqrt{-1}$. Given that we derived the TMM's eigensolutions from Euler-Bernoulli beam theory, resulting in a linear partial differential equation, and the piezoelectric constitutive equations are also linearized (see Appendix), the resulting motion and voltage output are also harmonic. Thus, we get the relative transverse motion at a point x from the base as

$$w(x,t) = W(x)e^{i\omega t} = \sum_{r=1}^{\infty} \frac{\left(\rho A\gamma\right)_r \omega^2 Y - \Theta_r V}{\omega_r^2 - \omega^2 + i2\zeta_r\omega_r\omega}\phi_r(x)e^{i\omega t} \tag{39}$$

and we get the voltage output as

$$v(t) = Ve^{i\omega t} = \frac{\frac{1}{C_0}\sum_{r=1}^{\infty}\frac{i(\rho A\gamma)_r \omega^3 \Theta_r Y}{\omega_r^2 - \omega^2 + i2\zeta_r \omega_r \omega}}{i\omega + \frac{1}{R_l C_0} + \frac{1}{C_0}\sum_{r=1}^{\infty}\frac{i\omega {\Theta_r}^2}{\omega_r^2 - \omega^2 + i2\zeta_r \omega_r \omega}} e^{i\omega t} \quad (40)$$

Evaluating Eq. (40) at the short-circuit condition, or the limit as R_l goes to zero, we confirm that $v(t)$ does indeed converge to zero. Likewise, evaluating the opposite extreme, i.e. the open-circuit condition where the limit of R_l goes to infinity, we verify that the current output of the structure converges to zero. The current output was found by applying Ohm's law $i(t) = v(t)/R_l$ on Eq. (40). Finally, we can evaluate the power output from $p(t) = [v(t)]^2 / R_l$.

6. Validation

In this section, we decompose and analyze six separate pVEH topologies, as depicted in Figure 1.5, and compare the TMM-based results to either well-accepted distributed-parameter models within the literature and/or using physical experiments. The topologies include the popular prismatic unimorph and bimorph cantilevers, as well as partial length coverage piezoelectric laminates or patches, and assemblies of commercial multi-beam bimorphs. For each of the cases, all the parameters are provided and the modeling decompositions are fully described in order to allow for comparisons with other modeling techniques.

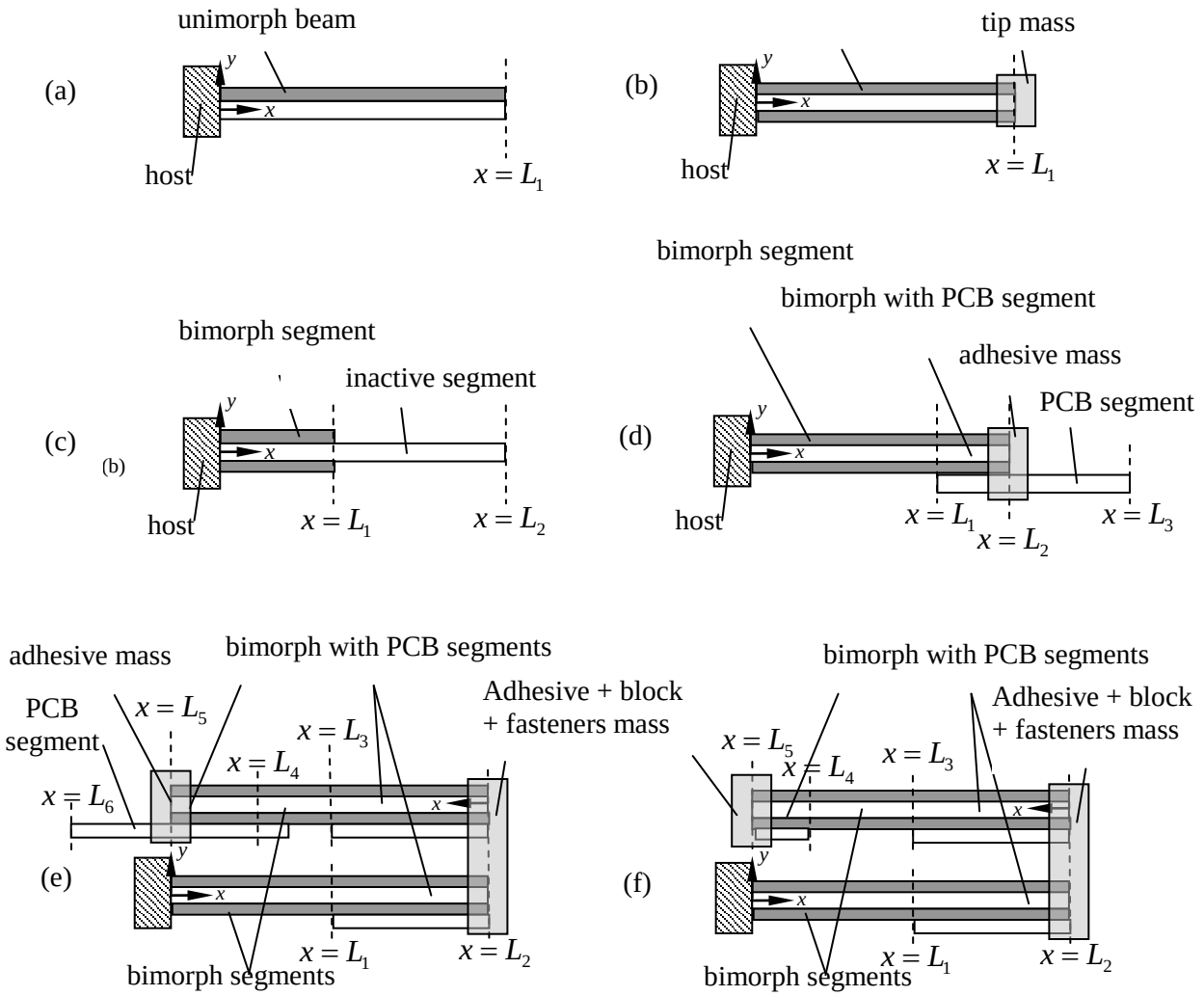

Figure 1.5: Six chain-link topology pVEH structures validated using the TMM model: (a) Unimorph without a tip mass (b) Bimorph with a tip mass (c) Partial-length bimorph without a tip mass (d) Multi-beam, inline bimorph without a tip mass (e) Multi-beam, folded-back bimorph without a tip mass (f) Multi-beam, folded-back bimorph with a tip mass

6.1 Uniform pVEH structures with only one beam (inline)

To begin, we compare our model with the well-accepted models of two uniform geometry pVEH structures: (1) the cantilevered unimorph [18] and (2) the cantilevered bimorph with a tip mass [20]. For each of the comparisons we relate our TMM-based natural frequencies at both short-

and open-circuit resistive loadings, thereby illustrating the matching of eigensolutions and incorporation of electromechanical behaviors.

6.1.1 Unimorph without a tip mass (Figure 1.5.a)

Using the same theoretical values as those described in [18], see Table 1.1, we first evaluate the cantilevered unimorph by decomposing it into a single uniform beam segment, which we represent as a single field matrix $\mathbf{F}_1$ that extends from the clamped condition to the free end. At the free end we consider, for generality, that a point matrix $\mathbf{P}_1$ exists but is equivalent to the identity matrix, since it has no mass and is considered inline. Thus for the solely unimorph topology, the field matrix $\mathbf{F}_1(L_1)$ is equivalent to the state transition matrix $\mathbf{\Phi}(L_1,0)$ for the entire structure, see Eq. (23). The clamped-free boundary conditions are used to solve Eqs. (26-29), yielding the short-circuit eigensolutions. These modal solutions are observed to be identical to that of a uniform geometry cantilevered beam without a tip mass. Implementing the electromechanical effects as described in *Section 4*, the TMM is confirmed to yield the same natural frequencies for both the approximate short-circuit, $R_l = 10^2\,\Omega$, and open-circuit, $R_l = 10^6\,\Omega$ conditions as derived by the distributed parameter model derived in [18], see Table 1.2.

Table 1.1: Geometry and material properties

Variable	Desciption	Case 4.1.1	Case 4.1.2	Case 4.2	Case 4.3	Case 4.4.1	Case 4.4.2
$(L_1,...,L_n)$	Length of beam segments [mm]	(100)	(50.8)	(Table 3, Table 3)	(25.4, 28.6, 44.5)	(25.4, 37.9, 50.4, 75.8, 79, 94.9)	(25.4, 37.9, 50.4, 75.8, 88.4)
$(m_1,...,m_n)$	Point mass [mg]	(0)	(12000)	(0, 0)	(0, 10, 0)	(0, 2284, 0, 0, 10, 0)	(0, 2284, 0, 0, 1884)
$(\theta_1,...,\theta_n)$	Discontinuity angle [degrees]	(0)	(0)	(0, 0)	(0, 0, 0)	(0, 180, 0, 0, 0, 0)	(0, 180, 0, 0, 0)
b	Width [mm]	(20)	(31.8)	(5, 5)	(3.2, 4.7, 4.7)	(3.2, 4.7, 4.7, 3.2, 4.7, 4.7)	(3.2, 4.7, 4.7, 3.2, 4.7)
t_s	Thickness of inactive layer* [mm] * Indicates a PCB layer of 1.67 mm also present	(0.5)	(0.14)	(0.25, 0.25)	(0.127, 0.127*, 0*)	(0.127, 0.127*, 0.127*, 0.127, 0.127*, 0*)	(0.127, 0.127*, 0.127*, 0.127, 0.127*)
t_p	Thickness of piezoelectric layer [mm]	(0.4)	(0.26)	(0.25, 0.25)	(0.191, 0.191, 0)	(0.191, 01.91, 0.191, 0.191, 0.191, 0)	(0.191, 01.91, 0.191, 0.191, 0.191)
ρ_s	Density of inactive layer / PCB* [kg·m^{-3}]	7165	9000	7850	8400 / 1850*	8400 / 1850*	8400 / 1850*
ρ_p	Density of piezoelectric layer [kg·m^{-3}]	7800	7800	7800	7800	7800	7800
c_s	Young's modulus of inactive layer / PCB* [GPa]	100	105	105	100 / 24*	100 / 24*	100 / 24*
c_{11}^E	Young's modulus of piezoelectric layer [GPa]	66	66	66	66	66	66
e_{31}	Piezoelectric constant [C·m^{-2}]	-12.54	-12.54	-12.54	-12.54	-12.54	-12.54
ε_{33}^S	Permittivity [nF·m^{-1}]	15.93	15.93	15.93	13.28	13.28	13.28

Table 1.2: Comparison of literature studies with predictions using the TMM

pVEH Structure (Cantilever Boundary Conditions)	Analytically Determined 1st Natural Frequencies [Hz]	Experimentally Determined 1st Natural Frequencies [Hz]	TMM Modeled 1st Natural Frequencies [Hz]	Relative Error (Theories , Experiment) [%]
Unimorph, no tip mass [18]	47.8 ($R_l = 10^2\,\Omega$) 48.8 ($R_l = 10^6\,\Omega$)	N/A N/A	47.8 ($R_l = 10^2\,\Omega$) 48.8 ($R_l = 10^6\,\Omega$)	0 , N/A 0 , N/A
Bimorph, with a tip mass [20]	45. 6 ($R_l \cong 0\ \Omega$) 48.4 ($R_l \cong \infty\ \Omega$)	45.6 ($R_l \cong 0\ \Omega$) 48.4 ($R_l \cong \infty\ \Omega$)	45.7 ($R_l \cong 0\ \Omega$) 48.2 ($R_l \cong \infty\ \Omega$)	0.2 , 0.2 0.4 , 0.4

6.1.2 Bimorph with a tip mass (Figure 1.5.b)

Second we examine the cantilevered, uniform geometry bimorph with a tip mass using the same generalized TMM approach. A single field matrix $\mathbf{F}_1(L_1)$ represents the uniform bimorph from the clamped condition to the free end, and a point matrix $\mathbf{P}_1$ represents the free end location $x = L_1$. However, for this configuration, at $x = L_1$ the point matrix $\mathbf{P}_1$ is not equal to the identity matrix since it must account for the translational and angular inertia introduced by the presence of the inline tip mass. The resultant state transition matrix is $\mathbf{\Phi}(L_1,0) = \mathbf{P}_1\mathbf{F}_1(L_1)$. Solving for the TMM eigensolutions of this pVEH configuration, we show that the mechanical, or short-circuit condition, mode shapes expand to match the eigensolutions of the modal solution [28] of a non-piezoelectric cantilever with a tip mass, see *Section 4.3.* Thus, we can implement the TMM eigensolutions with the electromechanical coupling using the values reported in [20] and shown Table 1. From those values, we find the TMM yields nearly identical natural frequencies as those previously found both theoretically and experimentally, with only a 0.2% difference for the short-circuit condition and a 0.4% difference for the open-circuit condition, see Table 1.2. Given the validation of the modified, distributed parameter model described in [20] used the results from that experiment to do so, we conclude that the TMM is also confirmed validate for this

topology. Thus, within this linear algebaraic framework, we provide an alternative matrix-based approach to generally relate the analyses of a cantilevered unimorph to a cantilevered bimorph with a tip mass.

6.2 Partial-length bimorph without a tip mass (Figure 1.5.c)

For the third topology, we perform a set of experiments with a non-uniform geometry, multi-segmented beam pVEH structure: the partial-length bimorph cantilever without a tip mass. This type of structure is also referred to as a cantilever with a bimorph patch. Here we extend our comparisons beyond the TMM-based natural frequencies to the accuracy of the mode shapes and mode shape slopes predictions.

To measure each of these eigensolutions, we create an experimental setup which tests five unique partial-length bimorphs with varying coverage percentages, see Tables 1.1 and 1.3. For each sample test, the partial-length bimorph segment is positioned at the clamped condition and extends to the point $x = L_1$, which is less than the total length L of the cantilevered beam on which it is attached. For the cantilever beam, we use a cold-rolled annealed 1095 spring steel substrate material. For each piezoelectric layer, we use a PSI-5A4E ceramic with nickel plated electrodes from Piezo Systems, Inc, with the same thickness and width as that of the steel substrate. The layers are adhered using Loctite E-120HP Hysol epoxy from Henkel AG & Co. The poling direction is orthogonal to the plane of the beam and is in the same direction for both layers, which creates the parallel, partial-length bimorph configuration. The piezoelectric response is dominant in the 31 direction. The structures are harmonically driven by a Bruel and Kjaer vibration exciter Type 4809, which has a first axial resonance frequency of 20kHz, well above the driving frequencies considered in this study. Measurements of the cantilevered

structure's transverse deflection at various points along its length are taken at the first resonance using a laser vibrometer from Polytec, Inc. From these measurements, we are able to experimentally determine the mode shape and its spatial derivative for various partial-length bimorph topologies and generate comparisons with the TMM-based solutions. In Figure 1.6 we provide a photograph of the actual experimental setup, showing the cantilever and the shaker.

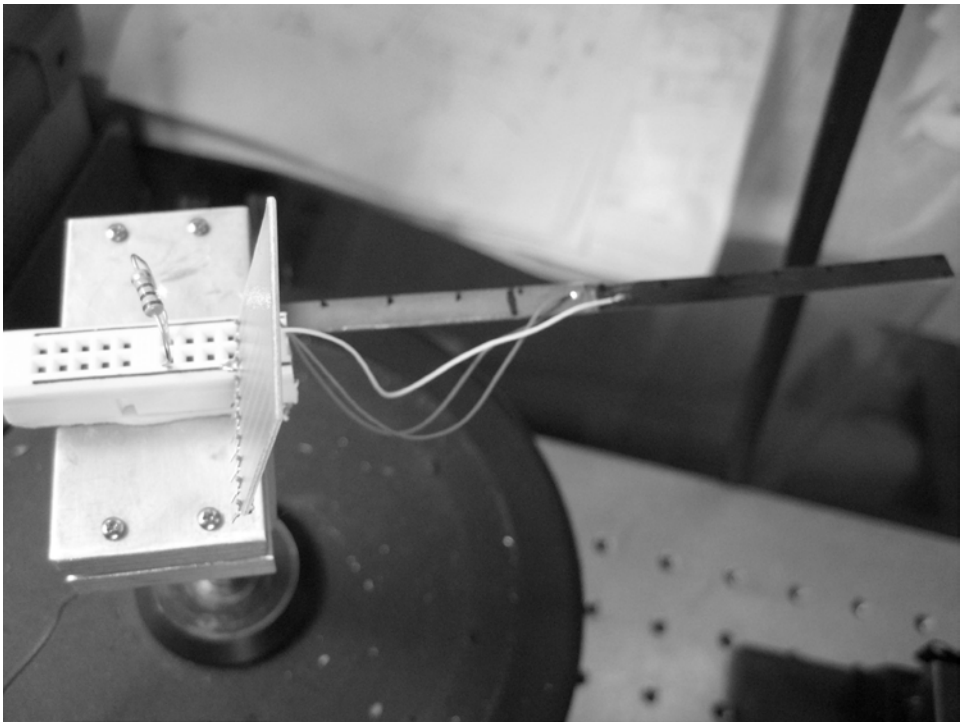

Figure 1.6: Photograph of experiment with partial-length bimorph cantilever without a tip mass. Clamped end is given a base excitation at resonance and eigenmodes are measured via detecting the motion along the beam with a laser vibrometer.

Table 1.3: Cantilevered, partial-length bimorph with variable coverage

Bimorph Length Coverage [%]	Bimorph Beam Segment (L_1) [mm]	Total Beam Length (L_2) [mm]	Experimentally Determined 1st Natural Frequency [Hz]	TMM Modeled 1st natural Frequency [Hz]	Relative Error [%]
40	40	100	46.25	45.76 Hz	1.06
45	50	110	42 Hz	41.52 Hz	1.14
50	60	120	38 Hz	37.15 Hz	2.24
63	52	83	84.25 Hz	82.53 Hz	2.04
81	52	64	117 Hz	118.95 Hz	1.67

To construct the TMM-based model for this discontinuous geometry topology, we decompose the beam into two separate prismatic beam segments: (1) the bimorph which extends from the base to $x = L_1$ and (2) the remainder of the non-piezoelectric laminated beam which extends from $x = L_1$ to the free end, $x = L_2 = L$. For the bimorph segment, we represent it using a field matrix $\mathbf{F}_1(L_1)$ and a point matrix $\mathbf{P}_1$. For the non-piezoelectric laminated beam segment, we have another field matrix, which is defined as $\mathbf{F}_2(L_2 - L_1)$, and a point matrix $\mathbf{P}_2$. Using the semigroup property, we multiply the transfer matrices for each segment from the successive order in which they appear along the non-uniform beam, which yields the state transition matrix $\mathbf{\Phi}(L_2,0) = \mathbf{P}_2\mathbf{F}_2(L_2 - L_1)\mathbf{P}_1\mathbf{F}_1(L_1)$. Examining $\mathbf{P}_1$ and $\mathbf{P}_2$, we observe that both are equal to the identity matrix since the discontinuities are inline and there are no external masses present. This simplifies the state transition matrix to $\mathbf{\Phi}(L,0) = \mathbf{F}_2(L - L_1)\mathbf{F}_1(L_1)$.

Evaluating the eigensolutions, we compare the results to the experimental setup. From Table 1.3, we show that the mechanical response shows between 1.06 % and 2.24 % minimal error when predicting the 1st mode's short-circuit natural frequency. This percent difference is well within experimental error and indicates extremely good accuracy for closed form modeling of the first natural frequencies of these non-uniform, inline geometric structures.

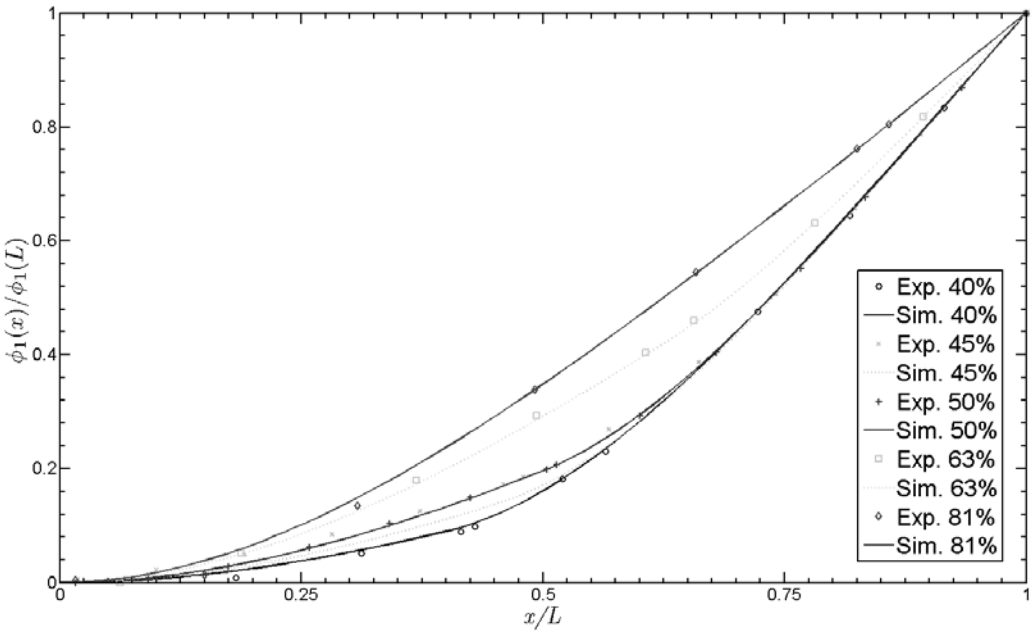

Figure 1.7: Comparison of TMM solutions and experiments for 1st mode shapes of varying partial-length bimorph structures

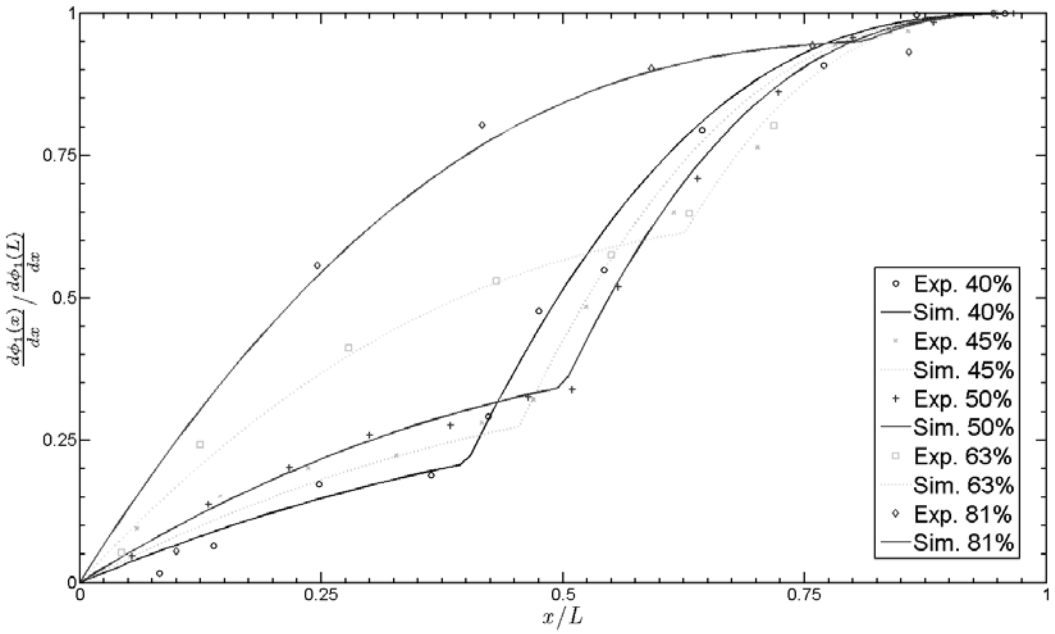

Figure 1.8: Comparison of TMM solutions and experiments for 1st mode shape spatial derivatives of varying partial-length bimorph structures

Investigating further, we compare the mode shapes and their spatial derivatives with the measurements from the laser vibrometer near the first natural frequencies. In evaluating Figures 1.7 and 1.8, we again see excellent agreement between the model and the experiment. Here, we note that while the laser vibrometer has excellent accuracy, any differences could be attributed to human error in determining the exact location along the structure for each of the laser vibrometer's single point measurements. The importance of correctly being able to predict these such solutions with respect to the electromechanical equations of motion is clear as shown in *Section 5,* specifically for the modal electromechanical and influence coefficients respectively. Thus, the validation of this decomposition method for both eigenfrequencies and eigenmodes makes it quite attractive as a means for compact, closed form solutions of partial-length piezoelectric designs, in addition to full-length unimorph and bimorph topologies.

6.3 Commercial Bimorph with a PCB Beam Attached to Tip (Figure 1.5.d)

Having shown in the previous two sections the accuracy of using the TMM for predicting the eigensolutions of single, inline uniform and non-uniform geometric structures, we extend the subset of calculable designs further by investigating an inline, cantilevered structure composed of two beams. Using the same shaker described in *Section 6.2*, we mount the commercial pVEH structure pictured in the top of Figure 1.1 in a cantilevered configuration and compare its measured natural frequencies and voltage frequency response with our TMM-based model. Here we note that as far as the authors are aware, this is the first time a TMM-based model has been validated experimentally with respect to its voltage frequency response, thereby strengthening its use as a closed form method for predicting pVEH power generation.

For the matrix-based model, we proceed as before and decompose the commercial device along its length, with all parameters described in Table 1.1. Starting with one of the printed circuit board (PCB) mounting beams as the clamped condition, the remainder of the pVEH device is modeled with three prismatic beam segments having discontinuities at each of their ends. We therefore ignore one of the PCB beams and begin the model with the bimorph segment, which starts from the edge of the mount to the edge of the next physical beam, i.e. the other PCB, it is attached onto. This prismatic bimorph segment is represented by a field matrix $\mathbf{F}_1(L_1)$ and a point matrix $\mathbf{P}_1$, which is evaluated at $x = L_1$. The second prismatic segment is the exact overlap length of the remainder of the bimorph composite with the free end's PCB beam, modeled as $L_2 - L_1$. This overlapped segment is represented by a field matrix $\mathbf{F}_2(L_2 - L_1)$, with composite beam theory used to determine items such as the effective stiffness. The second point matrix $\mathbf{P}_2$ is evaluated at $x = L_2$. The third and final transfer matrix pair represents the remainder of the PCB beam to the free end without any bimorph overlap. This pair is comprised of a field matrix $\mathbf{F}_3(L_3 - L_2)$ and a point matrix $\mathbf{P}_3$, which is evaluated at $x = L_3 = L$. The resultant state transition matrix for the entire structure employs the semigroup property and is the successive multiplication of all the matrices along the cumulative length, $L_3 = L$, of the beam segments, or $\mathbf{\Phi}(L_3,0) = \mathbf{P}_3\mathbf{F}_3(L_3 - L_2)\mathbf{P}_2\mathbf{F}_2(L_2 - L_1)\mathbf{P}_1\mathbf{F}_1(L_1)$. Simplifying, we observe that all the discontinuities are inline, or have zero-degree bends, and that at $x = L_1$ & $x = L_3$ there exist no lumped masses, but at $x = L_2$ we must account for a small mass from the adhesive used to bond the two beams. Therefore, the point matrices $\mathbf{P}_1$ and $\mathbf{P}_3$ reduce to the identity matrices and $\mathbf{P}_2$ has an adhesive mass m_2 which we approximate as 10 mg. Applying these to the state transition matrix, we obtain $\mathbf{\Phi}(L,0) = \mathbf{F}_3(L - L_2)\mathbf{P}_2\mathbf{F}_2(L_2 - L_1)\mathbf{F}_1(L_1)$.

Table 1.4: Cantilevered, multi-beam pVEH topologies

pVEH Structure (Cantilever Boundary Conditions)	Experimentally Determined 1st Natural Frequencies ($R_l = 976\ \Omega$, $R_l = 8.7\ M\Omega$) [Hz]	TMM Modeled 1st Natural Frequencies ($R_l = 976\ \Omega$, $R_l = 8.7\ M\Omega$) [Hz]	Experimentally Determined 2nd Natural Frequencies ($R_l = 976\ \Omega$, $R_l = 8.7\ M\Omega$) [Hz]	TMM Modeled 2nd Natural Frequencies ($R_l = 976\ \Omega$, $R_l = 8.7\ M\Omega$) [Hz]	Relative Error {(1st mode) , (2nd mode)} [%]
Bimorph with PCB attached at free end (Figure 5.d)	(111, 117)	(111.2 , 117.7)	(N/A , N/A)	(837.3 , 840.8)	{(0.2 , 0.6) , (N/A , N/A)}
2 bimorphs in folded-back configuration without a tip mass (Figure 5.e)	(35 , 37)	(35.2 , 37.2)	(92 , 94)	(92.0 , 93.8)	{(0.5 , 0.5) , (0.02 , 1.7)}
2 bimorphs in folded-back configuration with a tip mass (Figure 5.f)	(24.5 , 25.5)	(24.67 , 26.0)	(49 , 49.5)	(48.58 , 48.88)	{(0.7 , 2.1) , (0.9 , 1.2)}

After setting up the model and completing the analysis with the cantilever boundary conditions, we compare our TMM natural frequencies for the first mode with that measured experimentally, see Table 1.4. The results show excellent agreement for this inline, two-beam structure, with less than 0.6% difference for short- and open-circuit conditions at the first resonance. Additionally, for the mode shape solution at the first natural frequency, we observe the strong influence of the PCB beam's length on the spatial derivative of the mode shape, see Figure 1.9. From these eigenmode solutions, the strength of the TMM-based model is clear for accurate electromechanical solutions, as the PCB must be considered as a beam and cannot be simply lumped as a point mass.

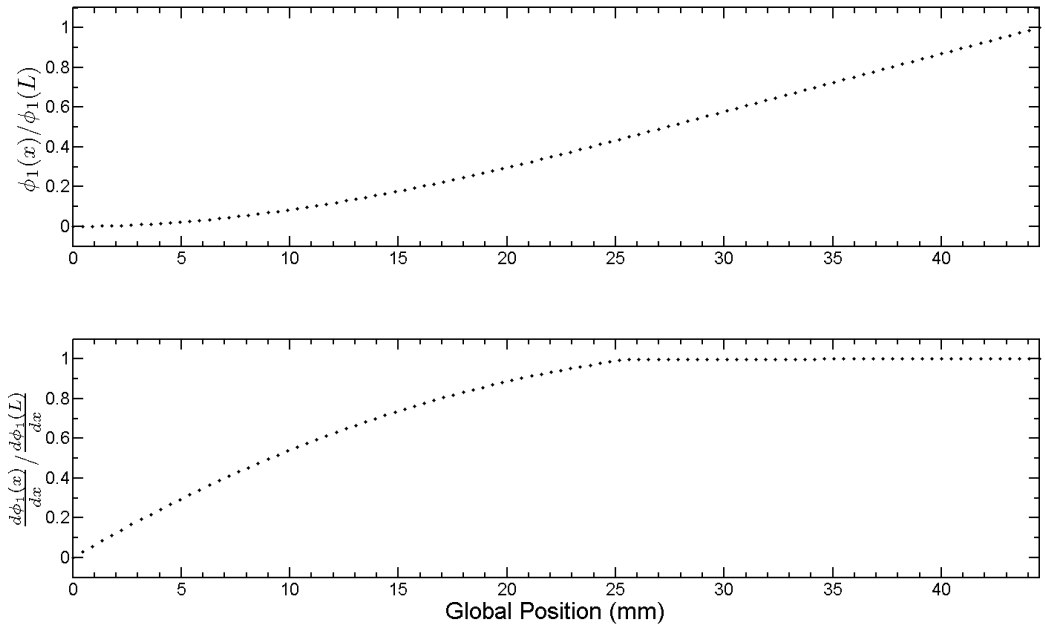

Figure 1.9: TMM predictions for mode shape and its spatial derivative about the 1st natural frequency of a clamped-free, two beam element structure (Piezo Sys: D220-A4-103).

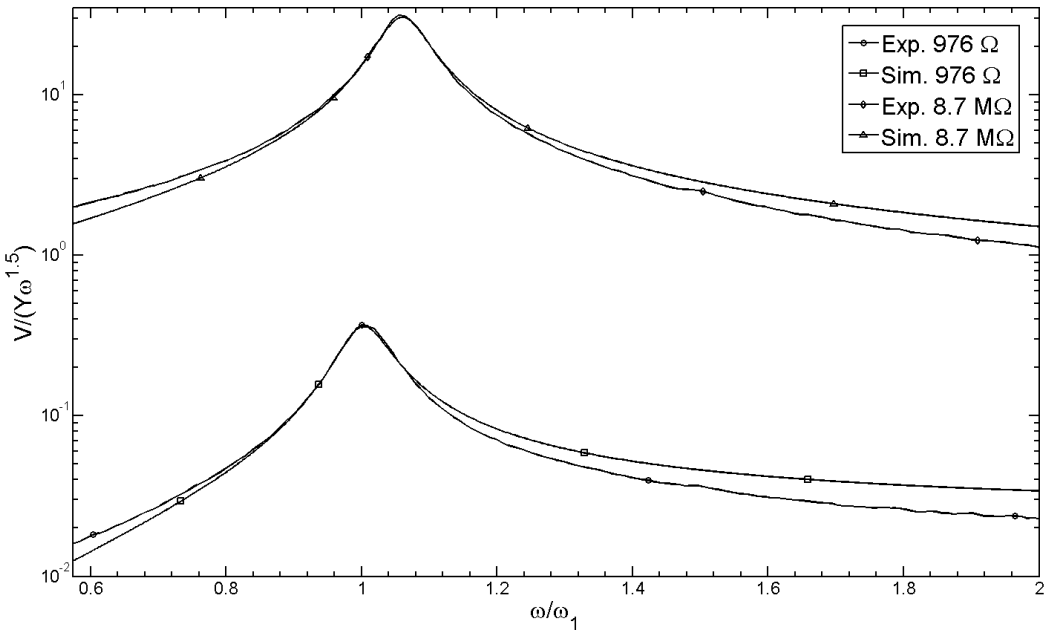

Figure 1.10: Comparison of TMM voltage frequency response about the 1st natural frequency of a clamped-free, two beam structure depicted in Figures 1.1 & 1.5.d (Piezo Sys: D220-A4-103).

Coupling the electromechanical effects with the eigensolutions, we perform a voltage frequency response at both short- and open-circuit conditions and compare the closed form solutions with experiment. As can be seen in Figure 1.10 using only the first mode, the TMM-based model predicts the transfer function extremely well within the ±10 percent bounds of the first natural frequency. While some deviation exists outside this range, we can correct for these errors by extending the model's solution to include higher order modes, as seen in the next section.

6.4 Non-uniform pVEH structures with multiple beams (folded-back)

With the TMM solution validated for inline structures with single and multi-beam segments, we now extend this method to two separate structures exhibiting folded-back topologies, i.e. containing at least one 180 degree discontinuity. From the following solutions and comparisons with experiments, we aim to convince the reader of this method's validity for such topologies, as well as give insights into the performance effects that 180 degree discontinuities yield with respect to compact structural forms, natural frequencies, and mode shapes.

6.4.1 Two structures from Section 6.3 with no mass at the tip (Figure 1.5.e)

The first folded-back structure is the same as the assembly pictured in the bottom of Figure 1.1, only without an added tip mass. For this and the following section, the same shaker described in *Section 6.2* is used for the experimental analysis. For the matrix-based model, we proceed similar to the decomposition in *Section 6.3*, since the assembly is comprised of the same commercial, multi-element bimorphs, see Table 1.1. The model begins with the origin starting from the edge of the mounting or clamped condition of the lower multi-element beam. We once again ignore the PCB mounting beam and begin the model with the bimorph segment from the edge of the

mount to the edge of the PCB it is attached onto. This prismatic bimorph segment is represented by a field matrix $\mathbf{F}_1(L_1)$ and a point matrix $\mathbf{P}_1$, which is evaluated at $x = L_1$. As from before, this point matrix can be defined using the identity matrix given its inline and no added mass properties. For the next transfer matrix pair, we perform a slight modification from *Section 6.3* and model the second prismatic segment as the distance to the center of mass of the point mass, $x = L_2 = 37.9$ mm and not the actual length to the end of the PCB beam, which is 44.5 mm. This composite segment is represented by a field matrix $\mathbf{F}_2(L_2 - L_1)$ and a second point matrix $\mathbf{P}_2$. Here $\mathbf{P}_2$ is the combined mass of the ABS plastic connecting block, fasteners, adhesive, and mass of the remainder of both the lower and upper PCB lengths un-modeled by the field matrix. The point matrix $\mathbf{P}_2$ is modeled with the 180 degree bend condition. Given the symmetry of the folded-back topology at the 180 degree bend, the third beam segment is equal to the second field matrix but has a point matrix equal to the identity matrix, since the direction continues along the length of the structure away from the block mass towards the free end. Proceeding along the structure, the remainder of the upper commercial bimorph beam has the exact same three transfer matrix pairs as in *Section 6.3*. Therefore with simplification, the state transition matrix is $\mathbf{\Phi}(L,0) = \mathbf{F}_6(L - L_5)\mathbf{P}_5\mathbf{F}_5(L_5 - L_4)\mathbf{F}_4(L_4 - L_3)\mathbf{F}_3(L_3 - L_2)\mathbf{P}_2\mathbf{F}_2(L_2 - L_1)\mathbf{F}_1(L_1)$. Here we note that even though there exists a greater number of prismatic segments and point matrices to describe this structure than in the previous topologies, the state transition matrix always remains 4 × 4 in format due to the linear algebraic formulation, regardless of the inline or 180 degree discontinuities. This compact lends itself well to less computational effort for eigensolutions with linear algebraic solvers such as MATLAB.

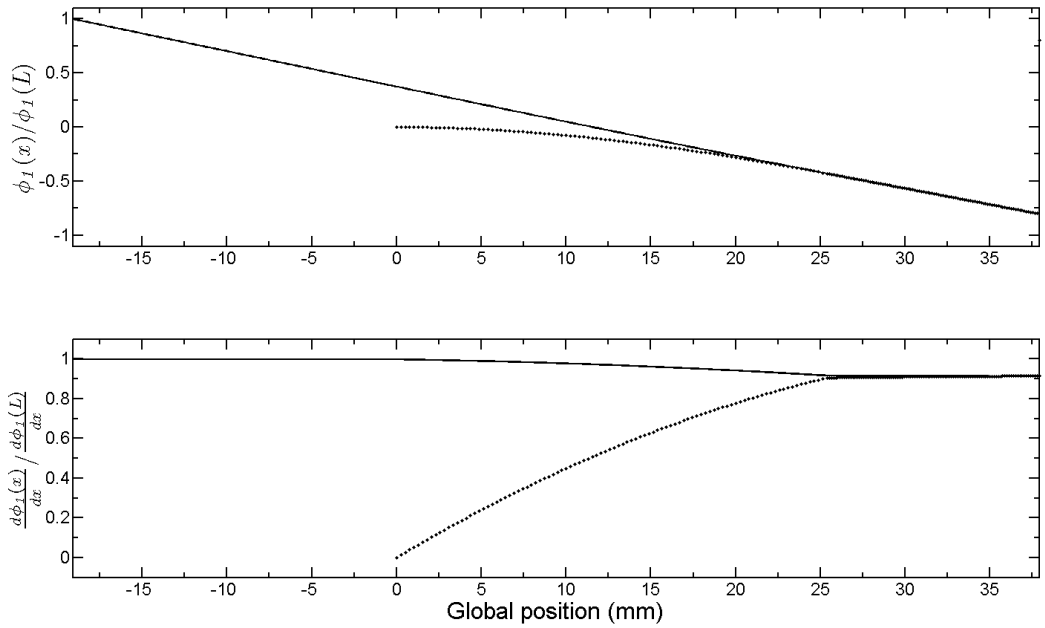

Figure 1.11: TMM predictions for mode shape and its spatial derivative about the 1st natural frequency of a clamped-free, two bimorph structure in folded-back configuration without a tip mass (see Figure 1.5.e)

Investigating the TMM-based natural frequencies for the first and second modes with that measured experimentally, we observe less than 1.7% difference for short- and open-circuit conditions when using a higher, three mode expansion model, see Table 1.4. Checking the mode shape solution at the first natural frequency, we again clearly see the influence of the PCB beams, especially on the spatial derivative of the mode shape at the 180 degree bend condition, see Figure 1.11. We therefore conclude that for accurate eigenmodes of multi-segmented structures, the TMM-based approach is quite useful not only for inline discontinuities but folded-back topologies as well.

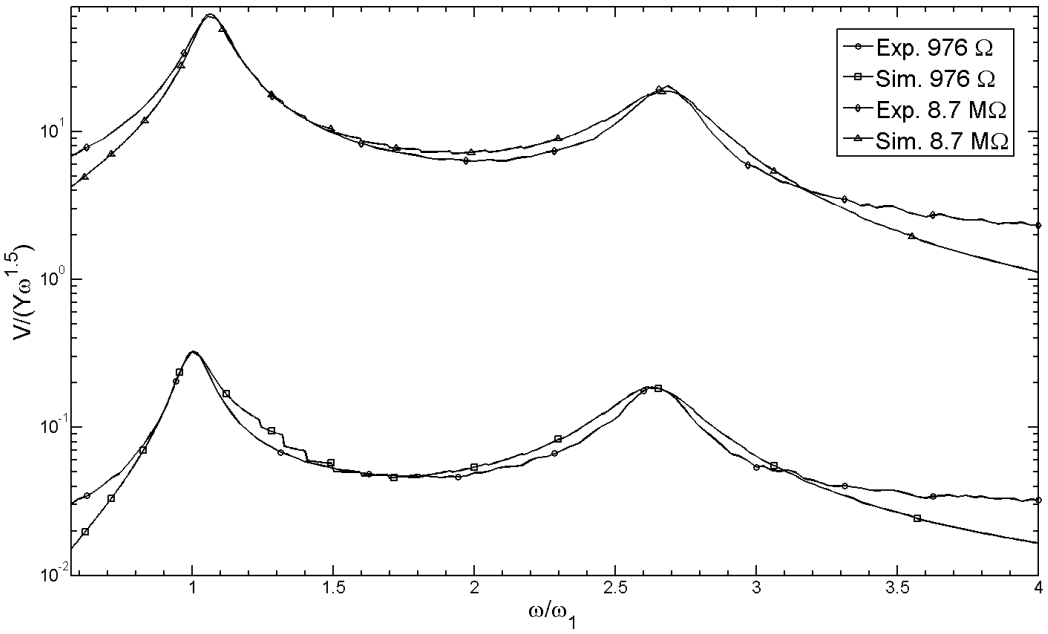

Figure 1.12: Comparison of TMM voltage frequency response about the 1st and 2nd natural frequencies of a clamped-free, two bimorph structure in folded-back configuration without a tip mass (see Figure 1.5.e)

Last, we compare our TMM model to the base excitation experiment for the voltage frequency response at both short- and open-circuit conditions at the first and second natural frequencies. Using the same three mode expansion for the model prediction, we observe in Figure 1.12 that the TMM predicts the transfer function extremely well about both of these natural frequencies, with slight error beyond the second mode. As mentioned previously, we can correct for this error at higher frequencies, if needed, by including higher order modes in the model expansion. Additionally, from this analysis we can predict a number of benefits of introducing a folded-back design. The first is that the first resonance can be decreased without extending the length far from the hos structure, or clamped condition. Second, we observe that the second resonance is driven closer to the first resonance due to the near symmetry of the folded-back configuration. As described in another work, we expect to see this second resonant frequency converge to

nearly twice that of the first resonant frequency as the geometric symmetry converges, a phenomena known as “repeated resonances” [26]. The benefit of these closer resonant frequencies for pVEH designs is that the bandwidth for power generation can increase between the two modes and not remain confined by the quality factor of a single beam [13].

6.4.2 Two structures from Section 6.3 with a mass at the tip (Figure 1.5.f)

The second folded-back topology is the same as in *Section 6.4.1* only with an added tip mass, making it closer in geometric symmetry than in the previous section. The exact assembly is pictured in the bottom of Figure 1.1. Here, we expect to observe both in the model and the base excitation experiment that the first resonant frequency decreases due to the added tip mass, as well as the second resonant frequency converges closer toward twice that of the first resonant frequency. As a point of reference, for the previous assembly without a tip mass, the first resonant frequency was 35 Hz and the second resonant frequency was at 2.6 times that value. For the matrix-based model, we proceed in the same fashion as in *Section 6.4.1* but with a modification to the last two transfer matrix pairs, see Table 1.1. To explain, the model begins with the origin starting from the edge of the mounting or clamped condition of the lower multi-element beam. We then ignore the mounting beam and begin the model with the bimorph segment from the edge of the mount to the edge of the PCB it is attached onto, giving a field matrix $\mathbf{F}_1(L_1)$ and a point matrix $\mathbf{P}_1$ equal to the identity matrix at $x = L_1$. Following the same modification as in *Section 6.4.1*, we model the second prismatic segment as the distance to the center of mass of the point mass and not the actual length of the beam, giving a field matrix $\mathbf{F}_2(L_2 - L_1)$ and a second point matrix $\mathbf{P}_2$ at $x = L_2$. The 180 degree bend point matrix $\mathbf{P}_2$ is the same as in the previous topology, with a combined mass from the ABS plastic connecting block,

fasteners, adhesive, and mass of the remainder of both the lower and upper PCB lengths un-modeled by the field matrix. In this configuration though, we observe that the second multi-beam structure with a tip mass is identical to the first, except for the tip mass magnitude, which doesn't include a second PCB beam. Thus, the symmetry of the folded-back topology at the 180 degree bend yields the third beam segment to be equal to the second field matrix but with a point matrix equal to the identity matrix, since as before, the direction continues along the length of the structure away from the block mass towards the free end. Proceeding forward along the structure, the purely bimorph section of the upper commercial bimorph beam is equal to the first set of transfer matrix pairs, or the lower purely bimorph beam section. The final beam segment with the tip mass uses the same modification for the field matrix as done at the 180 degree bend, accounting for the distance to the center of mass of the smaller point mass. The point mass P_5 is modeled as inline, with a magnitude equal to the ABS plastic connecting block, fasteners, adhesive, and mass of the remainder of the final PCB beam un-modeled by the field matrix. Therefore with simplification, we can model this nearly geometrically symmetric structure as $\mathbf{\Phi}(L,0) = \mathbf{P}_5\mathbf{F}_5(L-L_4)\mathbf{F}_4(L_4-L_3)\mathbf{F}_3(L_3-L_2)\mathbf{P}_2\mathbf{F}_2(L_2-L_1)\mathbf{F}_1(L_1)$.

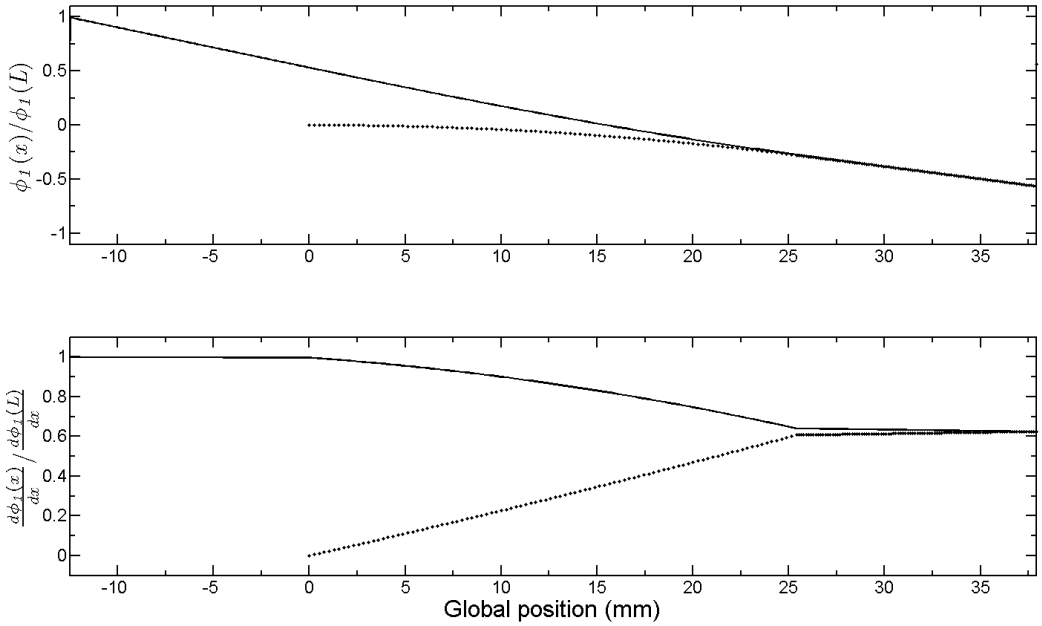

Figure 1.13: TMM predictions for mode shape and its spatial derivative about the 1st natural frequency of a clamped-free, two bimorph structure in folded-back configuration with a tip mass (see Figure 1.5.f)

Comparing the TMM-based natural frequencies for the first and second modes with that measured experimentally, we observe less than 2.1% difference for short- and open-circuit conditions when using the higher, three mode model, see Table 1.4. While this is the highest percent difference observed, we do note that it is well within experimental error and can be considered acceptable as a form of validation for this method. Likewise, we also observe from this analysis that the "repeated resonance" is correctly predicted, with the first resonant frequency reducing to 24.5 Hz and the second resonant frequency at nearly precisely twice the first resonance. Checking the effect on the mode shape solution at the first natural frequency, we notice the effect of the PCB segments as before but observe little qualitative difference between the assembly with and without tip masses, see Figures 1.11 and 1.13. Thus, the shift in the

resonant values appears not qualitatively with the mode shapes, but with a subtle shifting of the quantitative values.

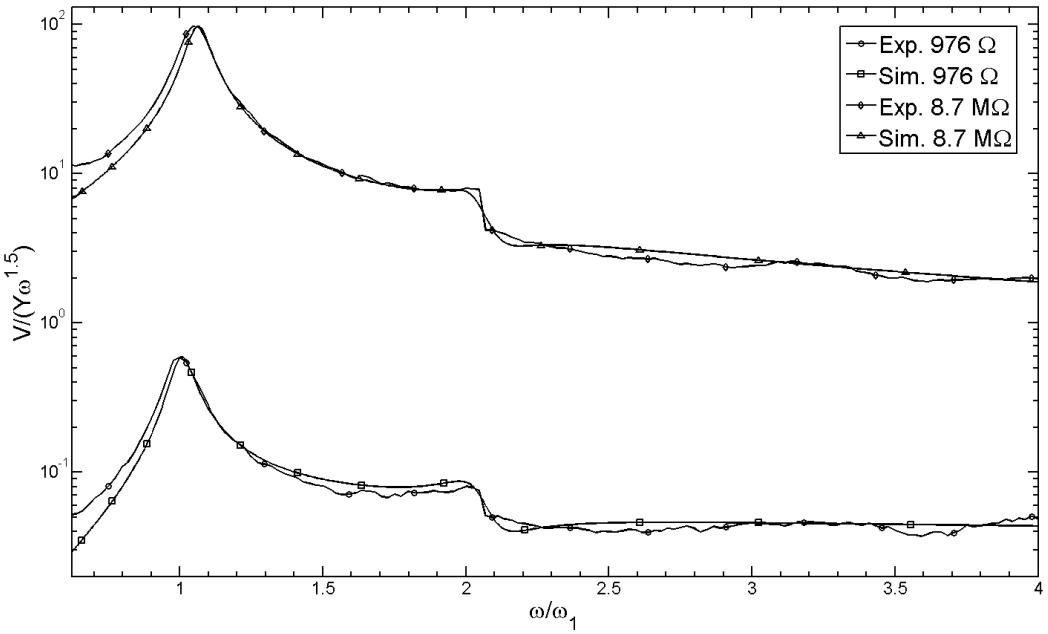

Figure 1.14: Comparison of TMM voltage frequency response about the 1st and 2nd natural frequencies of a clamped-free, two bimorph structure in folded-back configuration with a tip mass (see Figure 1.5.f)

Finally, we compare our TMM model for the voltage frequency response at both short- and open-circuit conditions at the first and second natural frequencies with the base excitation experiment. Using three mode expansion for the model prediction, we observe in Figure 1.14 that the TMM matches quite well about the first and second natural frequencies for the electromechanical response. Thus, the model correctly predicts the subtle changes of the "repeated resonances" phenomena not only mechanically but electrically as well.

7. Conclusion

In this paper, the transfer matrix method is derived and applied to the distributed parameter electromechanical model for piezoelectric vibration energy harvesters with continuous and discontinuous geometries. The analytical models are based on Euler-Bernoulli assumptions and a linearized piezoelectric model. The transfer matrix method works by solving for the variation of the state vector, composed of the transverse deflection, slope, moment, and shear force, along the length of the structure and across discontinuities. To achieve these solutions over continuous and discontinuous geometries, the transfer matrix method uses a segmentation approach to separate structures into uniform beam elements and points of discontinuity. Thus, the mathematical model is composed of two matrix types, known as the field and point transfer matrices. The field transfer matrix relates the states along each uniform geometry beam segment, while the point transfer matrix relates the states at each geometric discontinuity between the uniform beam segments.

In simplifying the analysis to only bending modes with transverse deflections, the applicable cases are limited to zero and 180 degree interfaces but still include the effects of any lumped masses or rotary inertias at the junctions between individual uniform beam segments. By multiplying the representative field and point transfer matrices in the order in which they appear along the structure, a state transition matrix is yielded with a constant 4×4 matrix size, regardless of the number of beam segments and discontinuities. This compact matrix form is valuable when trying to find closed form solutions for the eigenvalues and piecewise-continuous mode shape functions of such structures. Therefore with these solutions at hand, a generalized approach can be adapted to previous electromechanical models developed in the literature without having the caveat of being case specific. The validity of this method, both mechanically

and electrically, is confirmed by the high accuracy of the results shown in the *Section 5*, both with existing models and with experiments.

In terms of pVEH application, this technique is believed to be most valuable in designing multi-beam structures with attributes of low natural frequencies, small form factors, and larger energy conversion bandwidths. Furthermore, it is noted that the TMM is broadly applicable to non-electromechanical systems as well, simply by setting the electromechanical coupling to zero. In conclusion, the TMM is a versatile, linear analytic tool for solving the dynamic response of uniform and non-uniform geometric structures and can be now readily accepted for pVEH designs with our validated electromechanical solutions.

REFERENCES

[1] S. Roundy, P.K. Wright, J. Rabaey, "A study of low level vibrations as a power source or wireless sensor nodes," *Computer Communications*, **26**, p. 1131–1144, (2003)

[2] S.R. Anton, H. Sodano, "A review of power harvesting using piezoelectric materials (2003-2006)," *Smart. Mater. and Struct*, **16**, p. R1-R21, (2007)

[3] S. Priya, D.J. Inman, "Energy Harvesting Technologies," Springer, (2008)

[4] D. Shen, J. Park, J. Ajitsaria, S. Choe, H. Wikle, D. Kim, "The design, fabrication and valuation of a MEMS PZT cantilever with an integrated Si proof mass for vibration energy harvesting," *J. Micromech. Microeng*., **18,** 055017, (2008)

[5] J.Q. Liu, H.B. Fang, Z.Y. Xu, X.H. Mao, X.C. Shen, D. Chen, H. Liao, B.C. Cai, "A MEMS-based piezoelectric power generator array for vibration energy harvesting," *Microelectron. J*., **39**, p. 802–806, (2008)

[6] E. Reilly, P. Wright, "Modeling, fabrication and stress compensation of an epitaxial thin film piezoelectric microscale energy scavenging device," *J. Micromech. Microeng*., **19**, 95014, (2009)

[7] D. Shen, J. Park, J. Noh, S. Choe, S. Kim, H. Wikle, D. Kim, "Micromachined PZT cantilever based on SOI structure for low frequency vibration energy harvesting," *Sens. Actuators A*, **154**, p. 103–108, (2009)

[8] S. Roundy, E.S. Leland, J. Baker, E. Carleton, E. Reilly, E. Lai, B. Otis, J.M. Rabaey,

P.K. Wright, V. Sundararajan, "Improving power output for vibration-based energy scavengers," *Pervasive Computing,* **4**, p. 28- 36, (2005)

[9] T. Reissman, J.M. Dietl, E. Garcia, "Modeling and Experimental Verification of Geometry Effects on Piezoelectric Energy Harvesters," *Proceedings of 3rd Annual Energy Harvesting Workshop*, Santa Fe, NM, February 24-27, (2007)

[10] J.M. Dietl, E. Garcia, "Beam shape optimization for power harvesting," *J. Intell. Mater. Syst. Struct.,* **21**, p. 633-646, (2010)

[11] D. Guyomar, A. Badel, E. Lefeuvre, C. Richard, "Toward energy harvesting using active materials and conversion improvement by nonlinear processing," *IEEE Trans. Ultrason. Ferroelectr. Freq. Control*, **52**, p. 584–595, (2005)

[12] W.J. Wu, A.M. Wickenheiser, T. Reissman, E. Garcia, "Modeling and experimental verification of synchronized discharging techniques for boosting power harvesting from piezoelectric transducers," *Smart Mater. Struct.*, **18**, 055012, (2009)

[13] A. Erturk, J.M. Renno, D.J. Inman, "Modeling of piezoelectric energy harvesting from an L-shaped beam-mass structure with an application to UAVs," *J. Intell. Mater. Syst. Struct.*, **20**, p. 529-544, (2009)

[14] M.A. Karami, D.J. Inman, "Analytical modeling and experimental verification of the vibrations of the zigzag micro-structure for energy harvesting,**"** *J. Vib. Acoustics.*, **133**, 011002, (2011)

[15] S. Roundy, P.K. Wright, "A piezoelectric vibration based generator for wireless

electronics," *Smart. Mater. and Struct.*, **13**, p.1131–1142, (2004)

[16] N.E. duToit, B.L. Wardle, S. Kim, "Design considerations for MEMS-scale piezoelectric mechanical vibration energy harvesters," *Integr. Ferroelectr.*, **71**, p.121–160, (2005)

[17] H.A. Sodano, G. Park, D.J. Inman, "Estimation of electric charge output for piezoelectric energy harvesting," *Strain*, **40**, p.49–58, (2004)

[18] A. Erturk, D.J. Inman, "A distributed parameter electromechanical model for cantilevered piezoelectric energy harvesters," *J. Vib. Acoustics.*, **130**, 041002, (2008)

[19] A.M. Wickenheiser, E. Garcia, "Power optimization of vibration energy harvesters utilizing passive and active circuits," *J. Intell. Mater. Syst. Struct.*, doi: 10.1177/1045389X10376678, (2010)

[20] A. Erturk, D.J. Inman, "An experimentally validated bimorph cantilever model for piezoelectric energy harvesting from base excitations," *Smart Mater. and Struct.*, **18**, 025009, (2009)

[21] E. Pestel, F.A. Leckie, "Matrix Methods in Elastomechanics," McGraw-Hill, (1963)

[22] A.M. Wickenheiser, "Eigensolution of piezoelectric energy harvesters with geometric discontinuities: Analytical modeling and validation," *J. Intell. Mater. Syst. Struct.*, doi: 10.1177/1045389X12448447, (2012)

[23] D.J. Inman, "Distributed-Parameter Systems," Engineering Vibrations, Prentice-Hall, (2001)

[24] M.A. Koplow, A. Bhattacharyya, B.P. Mann, “Closed form solutions for the dynamic response of Euler-Bernoulli beams with step changes in cross section,” *J. Sound Vib.*, **295**, p. 214-225, (2006)

[25] S.C. Stanton, B.P. Mann, “On the dynamic response of beams with multiple geometric or material discontinuities,” Mech. Syst. And Sig. Processing, **24**, p. 1409-1419, (2010)

[26] A.R. Khattak, S.D. Garvey, A.A. Popov, “Repeated resonances in folded-back beam structures,” *J. Sound Vib.*, **290**, p. 309-320, (2006)

[27] T. Reissman, E. Garcia, "Electro-mechanical effect on resonances in fan-folded piezoelectric beam structures," *Proceedings of CanSmart International Workshop on Smart Materials and Smart Structures*, Montreal, Quebec, Canada, October 23-24, (2008)

[28] B.R. Bhat, H. Wagner, “Natural frequencies of a uniform cantilever with a tip mass slender in the axial direction,” *J. Sound Vib.*, **45**(2), p. 304-307, (1976)

[29] F.P. Beer, E.R. Johnston, “Mechanics of Materials,” McGraw-Hill, (2000)

CHAPTER 1 APPENDIX

Considering that many piezoelectric VEH can be segmented into composite beams classified as either unimorph or bimorph configurations, the following table is used to provide quick formulas for computing the effective parameters appearing in Eqs. (1,3,18a-b) for each type of beam segment:

Table 1.5: Vibration energy harvester parameters

	Unimorph	Bimorph
$(\rho A)_{eff}$	$b_s(\rho_s t_s + \rho_p t_p)$	$b_s(\rho_s t_s + 2\rho_p t_p)$
$(EI)_{eff}$	$\frac{b_s}{12}\frac{c_s^2 t_s^4 + 4c_{11}^E c_s t_p^3 t_s + 6c_{11}^E c_s t_p^2 t_s^2 + 4c_{11}^E c_s t_p t_s^3 + \left(c_{11}^E\right)^2 t_p^4}{c_{11}^E t_p + c_s t_s}$	$c_s b_s \frac{t_s^3}{12} + 2c_{11}^E b_s\left[\frac{t_p^3}{12} + t_p\left(\frac{t_p + t_s}{2}\right)^2\right]$
ϑ	$-\frac{e_{31} b_s}{2}\frac{c_s t_s (t_p + t_s)}{c_{11}^E t_p + c_s t_s}$	$-e_{31} b_s (t_p + t_s)$
C_0	$\frac{\varepsilon_{33}^S}{t_p} b_s L$	$\frac{2\varepsilon_{33}^S}{t_p} b_s L$

The variable $(\rho A)_{eff}$ is the mass per unit length and is described by the width *b*, density ρ, and thickness *t*. The susbscript $(\cdot)_s$ designates the substrate layer and $(\cdot)_p$ designates the piezoelectric layer. The effective stiffness $(EI)_{eff}$ is derived from composite beam theory [29] in which the geometric cross section is transformed by setting the modulus of elasticity to be the same for the entire beam segment and changing the width of the composite layers accordingly to account for the transformation. Following IEEE piezoelectric constitutive equations standards, the modulus of elasticity for each material is defined by the variable *c*. For the piezoelectric material the relevant modulus is c_{11}^E, where the subscript value 1 corresponds to the longitudinal component of the modulus and the superscript $(\cdot)^E$ indicates the use of a linearization at constant electric

field. The electromechanical coupling ϑ incorporates the piezoelectric coupling coefficient e_{31}, which is indicates the transverse bending mode. Lastly, the net clamped capacitance C_0 is defined using the dielectric constant ε_{33}^{S} of the piezoelectric material, where the polarization is assumed to be in the transverse axis, subscript 3, and the superscript $(\cdot)^{S}$ indicates a linearization at constant strain.

This chapter originally appeared as:

Reissman, T., Wickenheiser, A. M., and Garcia, E., "Closed Form Electromechanical Modeling and Experimental Validation of Piezoelectric Vibration-based Energy Harvesting Structures with Non-Uniform Geometries", *Smart Materials and Structures* (submitted)

CHAPTER 2
ELECTRICAL POWER GENERATION FROM SMALL ANIMAL FLIGHT[1]

1. Abstract

This article presents an implementation of a miniature energy harvester (weighing 0.292 grams) on an insect (hawkmoth *Manduca sexta*) in un-tethered flight. The harvester utilizes a piezoelectric transducer which converts the vibratory motion induced by the insect's flight into electrical power (generating up to 59 μW_{RMS}). By attaching a low-power management circuit (weighing 0.200 grams) to the energy harvester and accumulating the converted energy onboard the flying insect, we are able to visually demonstrate pulsed power delivery (averaging 196 mW) by intermittently flashing a light emitting diode. This self-recharging system offers biologists a new means for powering onboard electronics used to study small flying animals. Using this approach, the lifetime of the electronics would be limited only by the lifetime of the individuals, a vast improvement over current methods.

2. Introduction

The development of lightweight transmitters for small flying animals has allowed biologists to study their populations, gain valuable insights into their behaviors, and assess the environmental factors that drive their migrations [*1*]. Improvements in animal tracking technology and the decreasing size of micro-electronics have resulted in transmitters (tags) weighing as little as 0.2 grams, permitting the investigation of ever-smaller species [*2,3*]. Many of the same technological

[1] From Reissman, T., MacCurdy, R. B., and Garcia, E., "Electrical Power Generation From Small Animal Flight"; originally submitted to *Science* through the American Association for the Advancement of Science, Inc. This work was supported by the DARPA HIMEMS program.

advances, when combined with advances in bio-electronic interfaces, have allowed for the creation and control of cybernetic insects [*4,5*]. However, researchers in both areas of study have been primarily limited by the low payload capabilities of their target animal. With the majority of the electronic payload consumed by the battery, researchers are forced to compromise between functionality and lifetime, as in the case of ultra lightweight[2] tags which last only a few weeks [*3,6*].

Following Moore's law, the size of microelectronics have greatly decreased, but their power requirements and the energy density of batteries have not kept pace. These differing rates of technology development form the underlying cause of the endurance limitations. Researchers would benefit greatly if the lifetimes of these onboard electronics could be significantly extended without increasing the mass of the system. Ideally, the lifetime of any animal tag would equal the lifetime of the animal on which it is placed. To address this issue we look to the emerging field of energy harvesting. Energy harvesting is the process of converting energy from ambient sources into electrical energy for use by electronics [*7*]. Thus by using energy harvesting, the power system remains fixed in mass but is now self-recharging, resulting in the electrical energy being no longer finite.

Previous energy harvesting research conducted with humans describes several techniques for wearable devices. The first reported design was a shoe generator, which harvested energy from each heel strike motion, generating up to 0.8 W [*9,10*]. Subsequent devices made significant power improvements by allowing for greater relative motion, in order to increase the mechanical energy available for harvesting. Such devices include an energy harvester attached to the knee, producing 5 W [*11*],

[2] Although a lighter weight class of animal electronic systems exist called passive tags, they are limited by modest range and require high equipment costs [*6*]. Therefore, our focus is on improving the technology associated with the more functional active tags onboard flying animals.

and in the form of a backpack, producing 7 W [*12*]. In all three cases, the energy harvesters exploited the cyclic walking motion.

In the focus group of flying animals, wingbeats produce a similar cyclic motion, in the form of a body vibration, and a large source of ambient energy from which to harvest. However, the scale difference between humans and flying animals negates the possibility of directly adapting any of these previous designs. Even micro-system energy harvesters are not applicable, since they are only effective at vibration frequencies in the hundreds of Hertz, well above the typical wingbeat frequencies of the single to tens of Hertz [*6,13,14*]. In order to generate sufficient power from the animals' body vibration in flight, enough to perform basic electronic functions (Table 1.5), we were required to develop a new energy harvester design. The result was a piezoelectric backpack (Figure 2.1) that weighs 0.292 grams, generates a maximum power of 59 μW_{RMS}, and can be conditioned to generate 196 mW pulses.

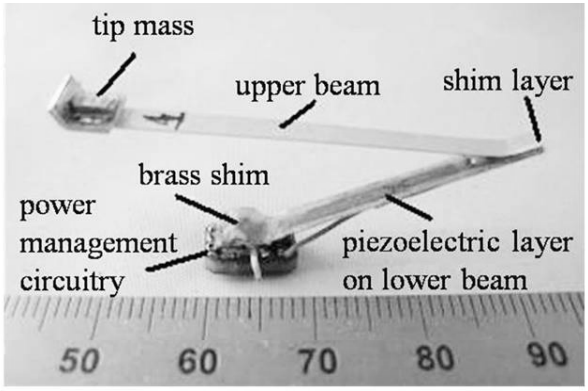

Figure 2.1: Energy harvesting piezoelectric backpack

All measurements were acquired from low-mass data logging tools onboard an insect, the hawkmoth *Manduca sexta* (*M. sexta*), under free flight conditions in an unbounded volume of space (Figure 2.2). These tools allowed us to assess the insects' flight behaviors with payloads, measure their maximum payload capabilities, and evaluate the power generated by the vibration

energy harvester. The use of these tools for the same assessments on other flying species may be widely applied given their low masses.

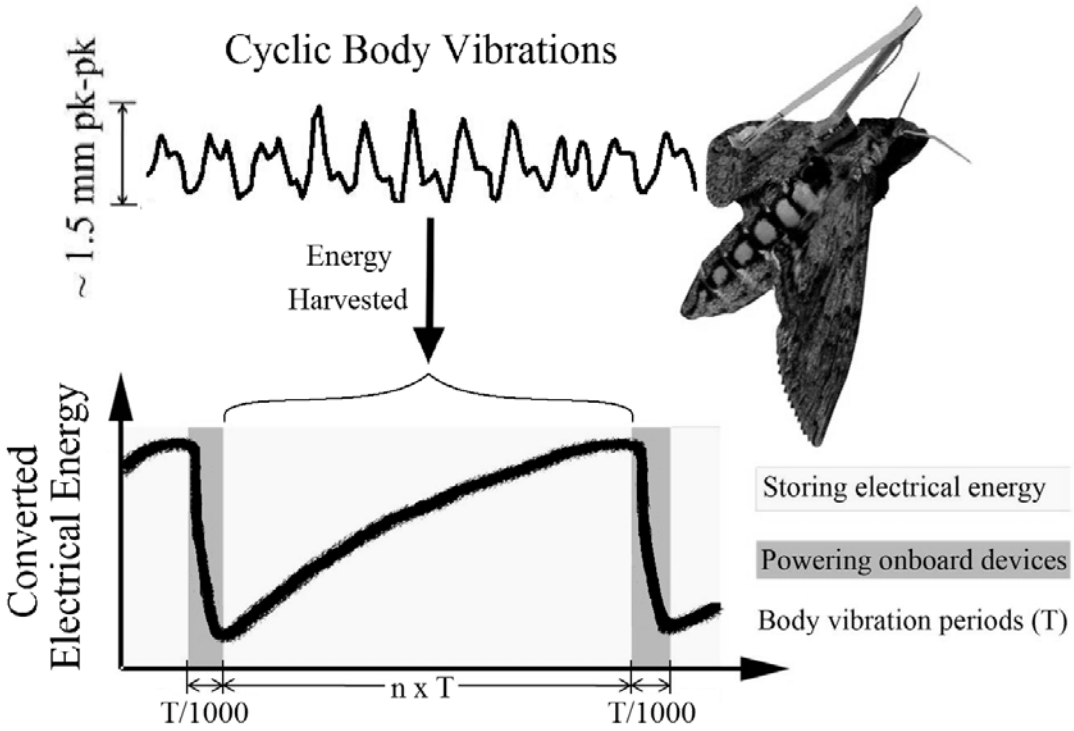

Figure 2.2: Overview of the energy harvesting process. Flying animals have an oscillating body motion, or vibration, induced by the flapping of their wings. Attaching our miniature energy harvester to the dorsal thorax of a hawkmoth *Manduca sexta*, we harness the body vibration to generate electricity, which is then stored by our power management circuitry in order to intermittently power onboard electronics.

3. Effects of Payload Flight

We selected the *M. sexta* as our flying animal model, due to the numerous studies on its flight mechanics and its capacity to carry additional mass, or payload. The test specimens used have a measured body mass of 2.43 ±0.38 grams and an approximate flight muscle mass of 0.47 ±0.11 grams (mean ± standard deviation, n = 47 specimens) (Table 2.2). The loaded cyclic body motion of this species is assumed to be very close to their un-loaded free-flight flapping frequency of 24 to 26 Hz [*14*]. With this frequency, we can predict the cyclic excitation which drives the power generation of the energy harvester. The maximum payload ability of this

species has previously been determined to be proportional to the flight muscle mass, with a maximum lifting force of 63.2 N kg^{-1} of flight muscle mass [*15*]. For our specimens this indicates an upper payload limit for liftoff at 0.61 ±0.60 grams. However, this value has a high variability and is unusable as a statistical estimate for this species' payload capability due to the variances that exist in the unladen muscle mass ratio, defined as the flight muscle mass divided by body mass, between individual specimens. In comparison, tag researchers widely use 5% of the flying animal's body mass as a heuristic for a generalized payload value [*16*]. Using this relationship, our energy harvester would be limited to a mass of 0.12 ± 0.02 grams. With such a large discrepancy from the maximum payload for liftoff, the need for a new method to provide researchers with appropriate, species-specific payload limitations for flight seemed vital. To achieve this, we created a lightweight data logging tag that can directly record the body accelerations of animals in free-flight, thereby investigating the effects of various payloads (Figure 2.3). This approach offers a far less expensive option, versus conventional high-speed camera systems, and adds the advantage of not requiring the animal be confined to a test chamber during flight.

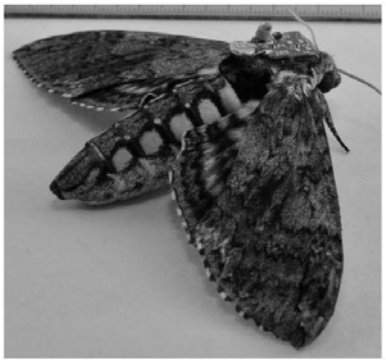

Figure 2.3: Flight motion recording unit attached to dorsal thorax

The payload study tag consisted of a tri-axial accelerometer and a microcontroller, which measured the flight motion onto the available memory of the unit. The attachment location,

alongside the dorsal thorax, allowed for firm adhesion between the exoskeleton and the electronics. Located near the insect's center-of-mass (COM), approximately one centimeter posterior to the thorax, the unit induced a minimal pitching moment on the insect body, allowing it to maintain flight. The flight motion measurements[3] were recorded with a sensitivity of ±0.6 m s^{-2} and a sampling rate of 200 Hz.

We tested 47 specimens (18 males and 29 females), each starting from the ground and flying untethered with a payload for 50 seconds. The initial payload consisted of only the payload study's tag, weighing 0.359 grams, and increased up to a maximum of 1.460 grams with the addition of calibrated weights. Each specimen was repeatedly tested until it was no longer able to fly, with the results for specimens able to fly at a given payload illustrated in Figure 2.4. Figure 2.4 (upper) shows that for the *M. sexta* specimens capable of flying, body accelerations and frequencies are regulated regardless of the payload present. The frequencies under payload are on average lower than the free flight frequencies, a result also observed in a payload study conducted with tethered fruit flies [*17*]. Additionally, a similar study using carpenter bees showed the same relatively flat slope or constant frequencies while in loaded flight [*18*]. While these correlations to the frequency responses of other flying animals under payload indicate the likely generalization of the results, our acceleration results provide even more detail to the understanding of the energetic effect on the animals. Although payload increments increased the specimens' mean mass by 60%, the corresponding decrease of only 24% in body accelerations implied that the *M. sexta* were able to

[3] See also Chapter 2 appendix section "Payload flight motion instrumentation and measurements"

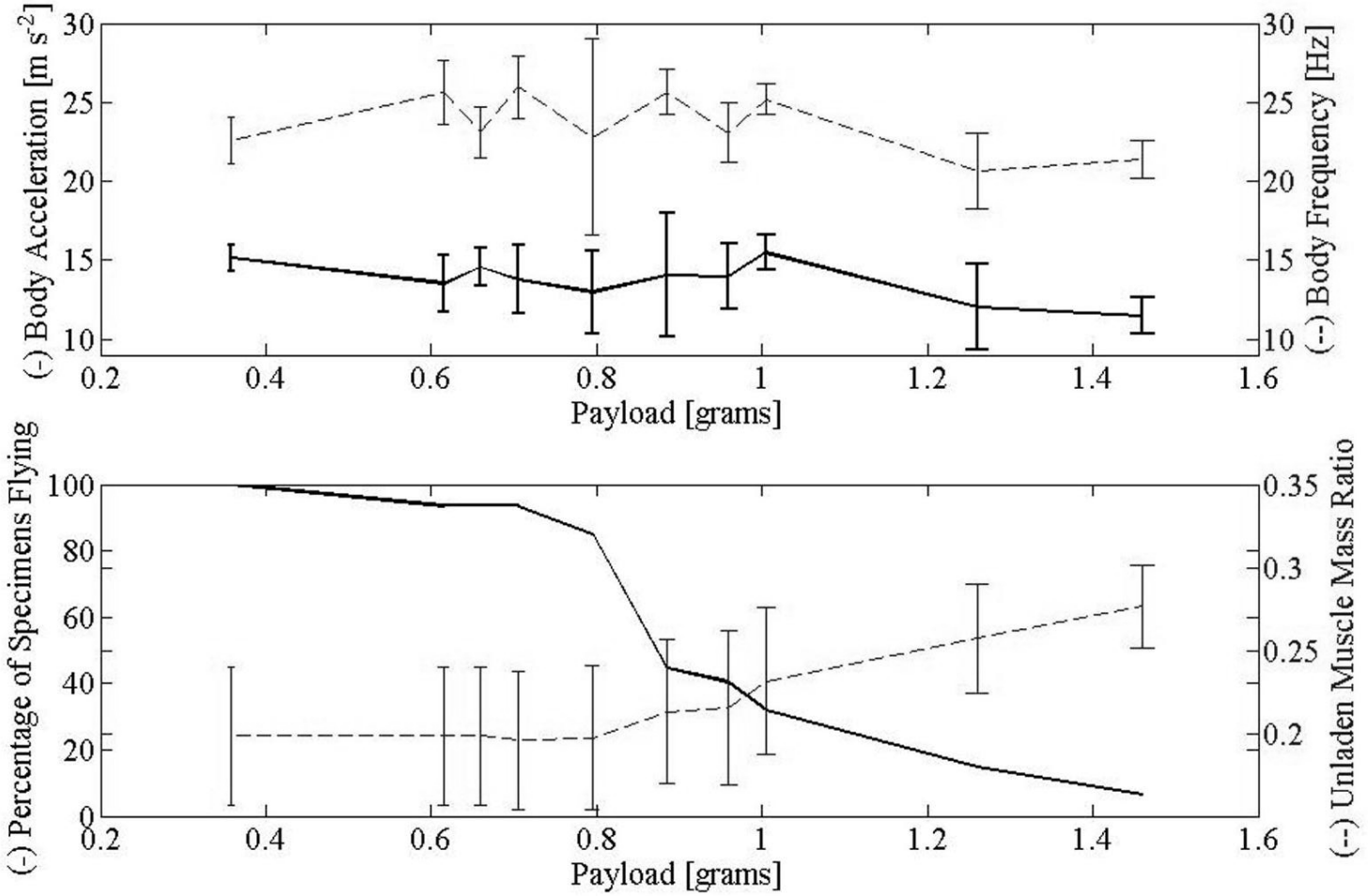

Figure 2.4: (upper) In-flight body accelerations and frequencies for increasing payloads on *M. sexta*. (lower) Percentage of tested specimens which were able to fly at each payload along with their unladen muscle mass

exert greater flapping forces in order to regulate their body motion. In Figure 2.4 (lower), a clear cutoff at approximately 0.8 grams existed for the percentage of our specimens that were able to fly. At this payload level, the corresponding standard deviation of the frequencies diverges considerably, indicating a statistical loss of the ability of *M. sexta* to regulate their flight motion. Beyond 0.8 grams, each subsequent payload increment was met with further reduction in the number of specimens able to fly and an increased unladen muscle mass ratio in order to sustain flight. We hypothesize that a similar cutoff exists in many flying species, at which a statistically significant divergence in body frequencies will be observed and which designates the true species-specific maximum[4] for allowable electronic payloads with regulated flight [*19,20*].

4. Energy Harvesting from Flight Motion

Utilizing the body acceleration data, we defined the vibration energy harvester's design with three criteria. The first was to have a resonant frequency near the exhibited body frequency of the total payload mass, obtained from the payload study. The second was to have a mass that lay within the statistical payload cutoff for flight, which was specified as below 0.8 grams for our specimen pool. The third was that the energy harvesting device have a compact form, with a center-of-mass located near that of the insect's COM, to remain minimally intrusive.

We selected a piezoelectric material as the transducer of the energy harvester due to its characteristically high voltage output and demonstrated ability to be fabricated at small dimensions [*21*]. A piezoelectric energy harvester converts the ambient motion, in this case the cyclic body vibration of a flying animal, into electrical energy by inducing a relative motion and

[4] In research involving electronics on flying animals, there exists added concern that the extra energy required from the animal may limit the maximum flight range or alter flight behaviors, which has been suggested by endurance studies performed with birds carrying electrical transmitters [*16*]. Thus, we regard our species-specific maximum payload as referring strictly to the affect on the regulation of flight mechanics and not its affects on energy homeostasis, wear and tear on muscles and joints, or other aspects that could be affected by chronic loading.

stress in the piezoelectric material. The axial deformation of the material's dielectric crystals causes a cyclic electric potential, and when applied to a resistive load, results in electrical power. Presently, piezoelectric designs utilize long, single-element cantilevers or large tip masses to lower resonant frequencies, but given the total mass and COM limitations, using this approach would only result in unacceptably long lengths or in micro-systems with mismatched resonances in the hundreds of Hertz [*7,21-22*]. To resolve all three design criteria, we developed a "zigzag" configuration at the centimeter length scale, which was composed of two linked elements connected to the dorsal thorax of the insect (Figure 2.1). The multiple element structure increased the effective length and decreased the resonant frequency to 22.3 Hz, without the addition of a large tip mass or a large shift in the animal's COM.

The energy harvester, weighing 0.292 grams, was custom-fabricated and attached to another lightweight logging device, weighing 0.315 grams. The system measured the instantaneous voltage output of the vibration energy harvester across a fixed resistive load (649 kΩ), which was chosen to maximize the electrical power conversion[5]. The voltage readings were then post-processed to obtain the instantaneous electrical power generation, defined as the voltage^2/resistance. Given the total system mass of 0.607 grams, we used the acceleration results from the payload study to estimate the relative motion of the energy harvester as approximately 6 millimeters in amplitude. To sustain this motion, the *M. sexta* must contribute an estimated 361 μW to replenish the energy lost to damping of the relative motion and to electrical energy conversion[6]. This power represents only 0.6% of the total mechanical power output by the flight muscles of this species, estimated at 100 W kg^{-1} of flight muscle mass. This low percentage

[5] See also Chapter 2 appendix sections "Estimated energy harvester relative motion and dissipated power" and "Calculation for resistive load of electrical power generation"

[6] See Chapter 2 appendix for further information on electrical damping and electrical energy conversion

insinuates that the weight of the unit, rather than the energy required to sustain the vibration, is responsible for the changes in flight performance [*23*].

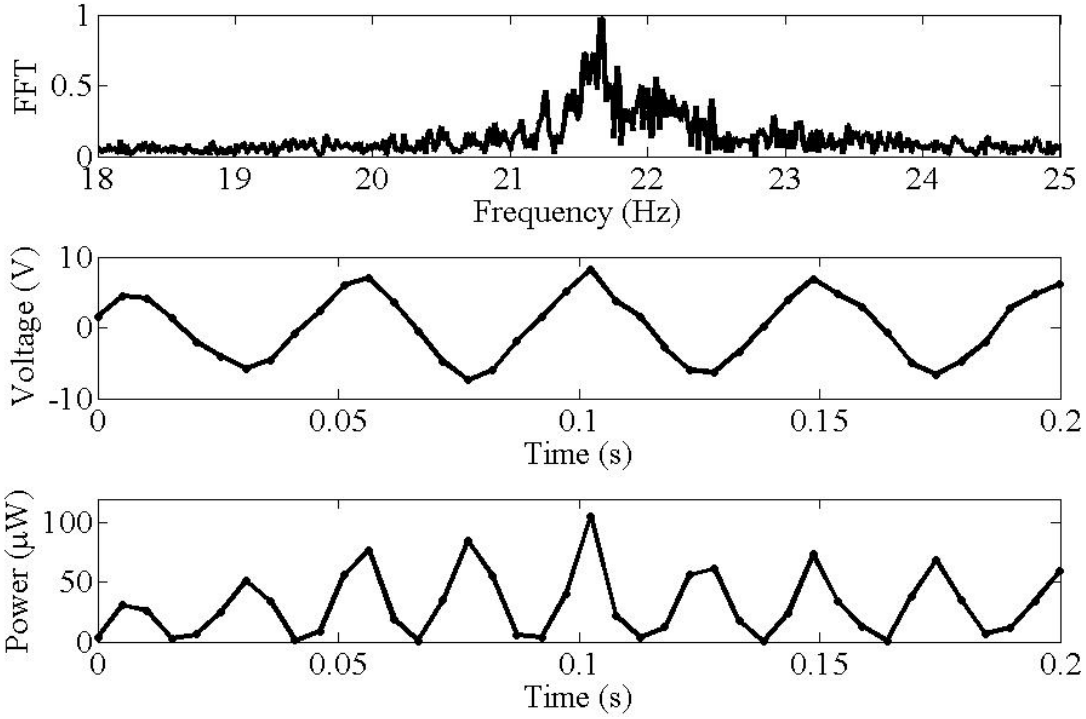

Figure 2.5: (upper) Frequency analysis using the Fast-Fourier-Transform (FFT) of the generated voltage's frequency. The primary frequency of the motion is located at the peak. (middle) The generated voltage output across a 649 kΩ resistor. (lower) The generated electrical power output during flight.

The energy harvester testing was conducted using a subset of the same specimens as the payload tests (5 males and 4 females) under the same conditions[7]. The base of the recording unit was attached to the dorsal thorax, and the energy harvester was attached to the upper side of the recording unit. Each specimen was placed on the floor just prior to recording and then allowed to fly un-tethered for 75 seconds. Figure 2.5 shows the frequency analysis of the cyclic body vibration and the electrical output of the energy harvester while in flight. In this trial, the primary

[7] See also Chapter 2 appendix section "Payload flight motion instrumentation and measurements"

frequency of the energy harvester's motion was 21.7 Hz, as shown in the upper plot. The middle plot displays the alternating polarity and the magnitudes of the voltage output of the energy harvester due to the cyclic body motion. The bottom plot presents the calculated instantaneous power generation, with a root-mean-squared (RMS) value of 35 μW.

The maximum power output obtained in flight was 59 μW_{RMS}, equating to an efficiency of 15.8% [*24*]. The average power across all specimens while in flight was 31.1 ±14.6 μW_{RMS} (Table 2.4). The large standard deviation in the results can be attributed to the range of exhibited frequencies and the selective sensitivity of the energy harvester to its specific resonant frequency, or high Q-factor. This emphasizes the importance of tuning the energy harvester's resonance as close to the exhibited frequency as possible for maximum power generation (Figure 2.6).

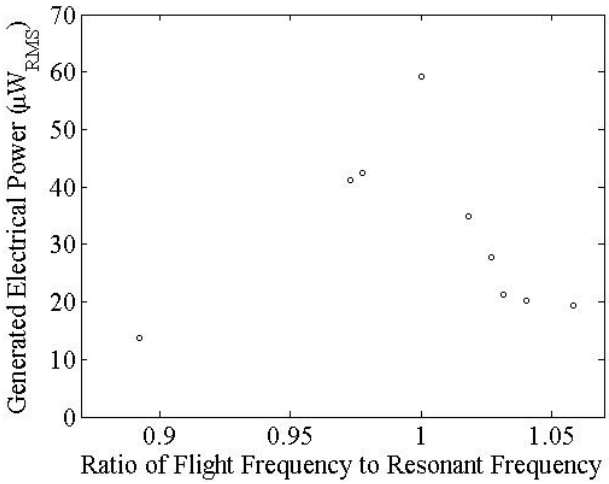

Figure 2.6: The electrical power output as a function of the ratio of the tuning of the vibration energy harvester's resonant frequency to the exhibited flight frequency.

To demonstrate the operation of our energy harvester, we built a 0.200 gram power management circuit and connected it to the energy harvester. The total system, weighing 0.492 grams, blinked a LED while attached to a *M. sexta* in free flight to visually demonstrate the harvested energy (Video 2.1). The circuit, which is self-starting and does not require a battery, works by

accumulating the harvested energy into a storage capacitor, and intermittently releasing the stored electrical energy into a LED, causing it to blink. The charging time between LED blinks is dependent on the activity level of the insect, with constant wing beats decreasing the time to approximately every 2 seconds (Figure 2.2). The average power dissipation through the LED during each blink is 196 mW for 29 micro-seconds, where the power and duration are dictated by the circuit design. The power losses in the circuit are approximately 5% for rectification [*12*] and 1.7 μW for the rest of the circuit (Figure 1.10 and 1.11). This demonstrated level of power discharge is therefore sufficient to power many of the common intermittent applications onboard flying animals, such as sensor readings and radio transmissions (Table 2.5).

5. Conclusion

In summary, two criteria must be met for an energy harvester to be a viable power source for the electronics on flying animals. First, the generated electrical power must exceed the requirements of the applications, in order to allow for losses in the power management circuitry which rectifies and regulates the harvested energy. Second, the energy harvester, power management circuitry, and other electronic devices must be able to be carried by the flying animal without causing a loss in flapping frequency control or adversely affecting flight behavior. Presently, our energy harvester system meets these criteria for the testing performed onboard *M. sexta*. Although implemented using an insect, the design allows for adaptation to other flying animals by changing the tip mass and beam geometry to match a range of wing beat frequencies.

By applying our procedure for determining free flight responses under payload, we expect researchers to be able to evaluate payload limits that are statistically relevant to the abilities of the target species. The success of our miniature piezoelectric backpack under free flight testing

conditions demonstrates that the use of such devices is viable and may just provide a much sought after solution for biologists to significantly improve electronics lifetime and extend the impact of this important class of wildlife monitoring tools.

REFERENCES

[1] T. Bookhout, "Research and Management Techniques for Wildlife and Habitats," *The Wildlife Society*, (1994)

[2] C. Holden, "Tracking Mini-Fauna," *Science*, **310**, p.773, (2005)

[3] B. Naef-Daenzer, D. Fruh, M. Stalder, P. Wetli, E. Weise, "Miniaturization (0.2 g) and evaluation of attachment techniques of telemetry transmitters," *Journal of Experimental Biology*, **208**, p. 4063-4068, (2005)

[4] H. Sato, C.W. Berry, Y. Peeri, E. Baghoomian, B.E. Casey, G. Lavella, J.M. VandenBrooks, J.F. Harrison, M.M. Maharbiz, "Remote radio control of insect flight," F*rontiers in Integrative Neuroscience*, **3**, 24, (2009)

[5] A. Bozkurt, R.F. Gilmour Jr., A. Lal, "Balloon-Assisted Flight of Radio-Controlled Insect Biobots," *IEEE Transactions on Biomedical Engineering*, **56**, 9, p. 2304-2307, (2009)

[6] K Niitepold, A.D. Smith, J.L. Osborne, D.R. Reynolds, N.L. Carreck, A.P. Martin, J.H. Marden, O. Ovaskainen, I. Hanski, "Flight metabolic rate and Pgi genotype influence butterfly dispersal rate in the field," *Ecology*, **90**, p. 2223-2232, (2009)

[7] N.S. Hudak, G.G. Amatucci, "Small-scale Energy Harvesting Through Thermoelectric, Vibration, and Radiofrequency Power Conversion," *Journal of Applied Physics*, **103**, 101301, (2008)

[9] J. Kymissis, C. Kendall, J. Paradiso, N. Gershenfeld, "Parasitic Power Harvesting in Shoes," *Proceedings of IEEE Conference on Wearable Computing*, p. 1-8, (1998)

[10] J.A. Paradiso, T. Starner, "Energy Scavenging for Mobile and Wireless Electronics," *IEEE Pervasive Computing*, **4**, 18, (2005)

[11] J.M. Donelan, Q. Li, V. Naing, J.A. Hoffer, D.J. Weber, A.D. Kuo, "Biomechanical Energy Harvesting: Generating Electricity During Walking with Minimal User Effort," *Science*, **319**, p. 807-810, (2008)

[12] L.C. Rome, L. Flynn, E.M. Goldman, T.D. Yoo, "Generating Electricity While Walking With Loads," *Science*, **309**, p. 1725-1728, (2005)

[13] C.J. Pennycuick, "Wingbeat Frequency of Birds in Steady Cruising Flight: New Data and Improved Predictions," *Journal of Experimental Biology*, **199**, p. 1613-1618, (1996)

[14] A.P. Wilmott, C.P. Ellington, "The Mechanics of Flight in the Hawkmoth Manduca Sexta," *Journal of Experimental Biology*, **200**, p. 2705-2722, (1997)

[15] J.H. Marden, "Maximum Lift Production During Takeoff in Flying Animals," *Journal of Experimental Biology*, **130**, p. 235-258, (1987)

[16] W.W. Cochran, "Long Distance Tracking of Birds," *Animal orientation and navigation*, **NASA SP-262**, p. 39-59, (1972)

[17] F. Lehmann, M .H. Dickinson, "The Changes in Power Requirements and Muscle Efficiency During Elevated Force Production in the Fruit Fly Drosophila Melanogaster," *Journal of Experimental Biology*, **200**, p. 1133-1143, (1997)

[18] S.P. Roberts, J.F. Harrison, R. Dudley, "Allometry of Kinematics and Energetics in Carpenter Bees (Xylocopa varipuncta) Hovering in Variable-Denisty Gases," *Journal of Experimental Biology*, **207**, p. 993-1004, (2004)

[19] C.J. Pennycuick, M.R. Fuller, "Considerations of Effects of Radio-Transmitters on Bird Flight," *Biotelemetry*, **IX**, p. 327-330, (1987)

[20] L.A. Powell, D.A. Krementz, J.D. Lang, M.J. Conroy, "Effects of radio Transmitters on Migrating Wood Thrushes," *Journal of Field Ornithology*, **69**, 2, p. 306-315, (1998)

[21] S. Roundy, P. Wright, J. Rabaey, "Energy Scavenging for Wireless Sensor Networks: With Special Focus on Vibrations," *Kluwer Academic*, (2004)

[22] R. Elfrink, T.M. Kamel, M. Goedbloed, S. Matova, D. Hohlfeld, Y. van Andel, R. van Schaijk, "Vibration energy harvesting with aluminum nitride-based piezoelectric devices" *Journal of Micromechanics and Microengineering*, **19**, 9, 094005, (2009).

[23] R.D. Stevenson, R.K. Josephson, "Effects of operating frequency and temperature on mechanical power output from moth flight muscle," *Journal of Experimental Biology*, **149**, p. 61-78, (1990)

[24] Y. Liao, H.A. Sodano, "On Structural Effects and Energy Conversion Efficiency of Power Harvesting," *Journal of Intelligent Material Systems and Structures*, **20**, p. 505-514, (2009)

[25] T. Reissman, A.M. Wickenheiser, E. Garcia, "Closed Form Electromechanical Modeling and Experimental Validation of Piezoelectric Vibration-based Energy Harvesting Structures with Non-uniform Geometries," *J. Smart Materials and Structures*, (in review)

[26] R.B. MacCurdy, T. Reissman, E. Garcia, "A Methodology for Applying Energy Harvesting to Extend Wildlife Tag Lifetime," *In Proceedings of ASME International Mechanical Engineering Congress and Exposition*, 68082, (2008)

[27] N. Ghafouri, H. Kim, M. Atashbar, K. Najafi, "A Micro Thermoelectric Energy Scavenger for a Hybrid Insect," *In Proceedings of IEEE SENSORS*, p. 1249–1252, (2008)

[28] S.C. Chang, F.M. Yaul, A. Domiguez-Garcia, F. O'Sullivan, D.M. Otten, J.H. Lang, "Harvesting Energy from Moth Vibrations During Flight," *In Proceedings of Power MEMS*, p. 1-4, (2009)

CHAPTER 2 APPENDIX

Test specimen's lifecycle development and general experimental protocol

Manduca sexta hawkmoths were tested using specimens obtained from the Boyce Thompson Institute at Cornell University (Ithaca, NY USA). The rearing protocol was the following: The eggs were hatched in a communal tub with diet (Table 2.1). Just after the molt to the second instar, larvae were individually placed in glass tubes with a cap full of diet and left to feed until becoming prepupae. Prepupae were placed in wooden blocks until just before emergence. Larvae were reared on a 16:8 light:dark photo period. Temperatures for larvae were 25^{o} C during light and 23^{o} C during dark. Pupae were kept at 27^{o} C until emergence.

Adult males and females were separated into large insect tents (Johnson Cage Tent, 1.43 m square by 1.5 m tall) with a 16:8 light:dark photo period at a constant room temperature of 21^{o} C. Deionized water and a 10% mixture of sucrose were mixed together and placed in 100 mL test tube vials to allow feeding.

To ensure repeatability of results, the following protocol was performed prior to any trials of the test specimens: Testing was performed within the first 3 days after emergence and during one hour of the transition period between light and dark photo period, when the insects were most active flyers. Prior to beginning a set of trials on a specimen, the dorsal thorax hair was removed using a scalpel, to expose the exoskeleton underneath, and allow attachment of the electronics using a small patch of double sided adhesive (3M, #4496) weighing 0.015 grams. With the electronics attached, the specimen was placed on the floor, with the recording unit turned on, and allowed to takeoff from the ground in un-tethered flight. The temperature of the room was held constant at 21^{o} C for all trials. After each trial, the electronics were removed and the data was

downloaded. Processing of the results was then performed using custom routines in MATLAB. Dissections were performed to measure the body mass and flight muscle mass (Table 2.2). All masses were recorded using an analytical scale (Mettler Toledo, AG104). Flight muscle mass was estimated as 97% of the thorax mass, which did not include the mass of the legs [*15*].

Payload flight motion instrumentation and measurements

Flight motion measurements were recorded using a custom electronics unit (Figure 2.7). The unit consisted of a tri-axial accelerometer sensor (Bosch, BMA 150) with a sensitivity of ±0.6 m/s^2 and a sampling rate of 200 Hz, a microprocessor (Texas Instruments, MSP430) that stores the all three axes' measurements up to 50 seconds, and a battery (Seiko, MS412FE) to power the electronics. The board was populated on both sides with a 400 μm thickness to save mass, weighing 0.359 grams including the adhesive layer connecting it to the specimen. Recording was initiated by manually pushing a toggle switch (Deltek, 2100-400). The data was retrieved by connecting the unit using a standard electronics JTAG connection and commercial connector device (Elprotronic, FlashPro 430).

Trials were conducted with 47 specimens (18 males and 29 females), each starting initially from the ground and flying un-tethered for 50 seconds with a payload. Each was then retested with increasing payloads until they were no longer able to lift off the ground. The flight motion recording unit was placed on the subject using adhesive tape placed between the bottom side of the unit and the dorsal thorax exoskeleton. Sufficient rest was given between tests to ensure the insect was able to fly prior to the subsequent test. To verify this, the insect was not tested until it demonstrated the ability to fly without a payload before each trial. The accelerations were measured with respect to the specimen's reference frame, with the x component anterior, the y

component lateral, and the z component perpendicular to the body. The accelerations were then combined into one measurement by taking the root-mean-square (RMS) value for each of the three acceleration components while in flight and calculating the norm, or magnitude, of the resulting vector. The measured acceleration norms for each specimen and the primary frequency component, found by taking the frequency at the peak power spectral density, were performed using a custom MATLAB routine and the results are shown in Table 2.3.

Energy harvester design description

The piezoelectric energy harvester (Figure 2.1) was hand-fabricated and consisted of two beams adhered together using cyanoacrylate (CA) adhesive at their ends with an aluminum shim (.254 x 3 x 3 mm) in between. The shim allowed a small separation to be created between the two beams, and resulted in the relative motion occurring without the beams striking each other at the junction. The lower beam consisted of an aluminum layer (.127 x 32 x 3 mm) bonded in the center to a piezoelectric layer (Piezo Systems, T105-H4E-602 custom cut to .127 x 23 x 2 mm) using a thin coating of silver conducting epoxy (MG Chemicals, 8331-14G). A layer of shim brass (.025 x 3 x 3 mm) was adhered to the opposite end of the lower beam from the square aluminum shim using the same layer of conductive epoxy. The brass shim allowed for a stronger solder connection over the aluminum layer for a wire lead to be placed. Two 36 AWG wires (McMaster Carr, 9511T413(4)) were soldered to the piezoelectric layer and brass layer to allow lead connections to the energy harvester's circuit. A protective insulator layer was placed over top of the entire lower beam to prevent physical contact of the top beam with the two leads, which would otherwise cause a short circuit and result in no power generation. The top beam was composed of a single aluminum layer (.127 x 40 x 3 mm) and a 0.060 gram mass (Ohaus,

ASTM Class 6) CA glued to the free end. The beams were bent at angles to create a separation distance greater than the maximum calculated relative motion amplitude of the free end with respect to the base. The final mass of the energy harvester was measured to be 0.292 grams.

Power recording instrumentation and measurements

The electrical power generation was determined by attaching a custom recording unit (Figures 2.8 and 2.9), weighing 0.315 grams, to the energy harvester's wire leads. The base of the energy harvester was CA glued to the battery (Seiko, MS412FE), and the wire leads were soldered to the recording unit. The energy harvester's voltage output was measured across a resistor load (649 kΩ) and recorded into a microprocessor (Texas Instruments, MSP430). The unit was turned on prior to each trial by flipping a toggle switch (Deltek, 2100-400). Measurements were recorded for 75 seconds of un-tethered flight, with each specimen starting from the ground. A subset (5 males and 4 females) of the same specimens from the payload study was used for this energy harvester study. Specimens were tested at the same time as their respective payload study. The data was retrieved by detaching the energy harvester from the recording unit and connecting the logger using the JTAG connector and commercial device (Elprotronic, FlashPro 430). The instantaneous power was calculated as the voltage^2/resistance, and the root-mean-squared power while in flight was determined using a custom MATLAB routine. The electrical power recordings for subject #2 are shown in Figure 2.5 and the overall results for all the subjects can be seen in Figure 2.6, with the data listed in Table 2.4.

Power management electronics

We demonstrated a visual confirmation of the power generation by the energy harvester in un-tethered flight on a *M. sexta* by developing a custom power management circuit (Figure 2.10 and 2.11). The 0.2 gram circuit rectified the alternating polarity of the electrical power coming in (Figure 2.5) and stored the electrical energy into a 4.7 μF capacitor. The capacitor's voltage level was monitored by a nano-ampere comparator (Linear Technology, LTC 1540), which determined the on and off voltage thresholds for releasing the stored electrical energy to the electronic load, in our case a light emitting diode (LED). The threshold voltage settings were set at 3.37 V for opening the switch and 1.82 V for closing the switch. The stored electrical energy dissipated across the LED was calculated as ½ times the capacitance times the (voltage difference)^2, which equaled 5.71 μJ for our circuit. A 10 Ω resistor was placed in series with the LED to control the rate of electrical energy discharge to an average power of 196 mW over 29.1 micro-seconds and produce a distinct blink of the LED. The flash of the LED, which lasted longer than the time of the pulsed power due to the longer thermal time constant, indicated that a successful amount of net converted energy was stored and used by our electronic load.

The power management circuit was attached to the base of the energy harvester on top of the comparator chip using CA adhesive. The leads were soldered to the wire connectors and the bottom of the power management board was adhered to the insect's dorsal thorax using the adhesive tape. The power consumption of the rectifier was estimated at 5% [*9*], and the power consumption of the rest of the circuit was measured using a Keithley 2400 Sourcemeter, which measured a maximum power draw of 1.7 μW at the upper voltage threshold (Figure 2.12).

The result can be seen in the accompanying video, showing the energy harvester connected to the power management circuit and having repeated LED flashes while on the insect (Video 2.1). It

should be noted that LED flashes were demonstrated while the insect was flapping its wings, both on the ground and in un-tethered flight.

Maximum payload relationship

The payload for lift capabilities (Table 2.2) were calculated using two separate relationships. For reference [*15*], the value is simply

$$\max payload_{(16)} = 0.05 \times (m_{body}) \tag{1}$$

where m_{body} is the body weight. For reference [*14*], the relationship is

$$\max payload_{(15)} = K_{muscle} \times \frac{m_{muscle}}{9.81\left[m/s^2\right]} - m_{body} \tag{2}$$

where K_{muscle} is the maximum lift force per unit of muscle mass, or 63.2 N kg^{-1} for *M. sexta* and m_{muscle} is the flight muscle weight. The mean difference in payload values using Equations (1) and (2) for *M. sexta* was nearly 0.5 grams. Results using our onboard acceleration measuring technique revealed regulation of flight for payload values up to 1.460 grams. The broadening of the standard deviation of body frequencies near 0.8 grams, along with the steep drop-off in percentage of specimens being able to fly, displayed a new means of determining the payload cutoff for our species. Using these recognizable changes in flight motion under payloads, we hypothesize that a species-specific method for determining appropriate payloads may exist. For this work, it has been demonstrated that loaded flight can be maintained by a *M. sexta*, exhibiting small drops in accelerations and frequencies given sufficient unladen muscle mass ratios.

Estimated energy harvester relative motion and dissipated power

The energy harvester's mechanical energy input was predicted by approximating the system as a two prismatic beams connected in a folded-back topology with point masses at each of their beam segment tips (Figure 2.14). Using the modified transfer matrix (TMM) representation [25], the following state transition matrix for the structure was described as

$$\mathbf{\Phi}(L_2,0) = \mathbf{P}_2\mathbf{F}_2(L_2 - L_1)\mathbf{P}_1\mathbf{F}_1(L_1) \tag{3}$$

,where the field matrix $\mathbf{F}_1(L_1)$ represented the dynamics of the structure's lower beam segment, or unimorph, which began at the Hawkmoth's thorax and ended at the folded-back, or approximate 180 degree bend condition. Thus the point matrix $\mathbf{P}_1$ represented the influence of the 180 degree bend discontinuity, with the shim mass magnitude also accounted for. The last two transfer matrix pairs represented the dynamics of the upper beam without any piezoelectric material but included the effects of the aluminum tip mass. Likewise, we note that the point matrix $\mathbf{P}_2$ was modeled as an inline, or zero degree bend discontinuity. We then inputted the geometric parameters and performed an eigensolution solution with the electromechanical effect incorporated. The results estimated the structure's first resonance to be near 23.2 Hz.

With the resonance within the estimated range of the flapping frequencies, we then confirmed its performance by experimentally measuring the energy harvester using the voltage output across the 649 kΩ resistive load while under excitation. The results are plotted with a dynamic signal analyzer (Hewlett Packard, 35665A) (Figure 2.13). From the frequency response plot, we determined the actual resonance to be 22.3 Hz, a 4% difference. The damping ratio ζ was found to be 0.06.

To determine the estimated power output, we approximated the base excitation using the flapping angular frequency ω and the thorax displacement Y_0 from the payload flight motion data at 0.660 grams. This payload was chosen since it was the closest representative value to the actual system mass, 0.607 grams, from our subset of specimens tested. Using the calculated RMS amplitude of the relative motion of the tip mass, the total power needed to sustain this motion (to replenish the energy lost to damping of the relative motion and to electrical energy conversion) using the lumped parameter estimate within Equation (5) [*26*].

$$P_{vibration} = m\zeta z_{RMS}^2 \omega_n^3 \tag{5}$$

The conversion efficiency was determined by taking the percentage of the generated electrical power to this vibration power [*24*]. The results indicated low conversion efficiencies and were attributed to the fact that this system was not considered for optimality, but instead designed for resonance near the body frequency. Reinvestigation for an optimal structural design with respect to power output would most likely improve performance, but was not the focus of this work. From the analysis above, a researcher can estimate the power dissipation incurred by the implementation of an energy harvester, and based on an estimate of the conversion efficiency, determine the electrical power generation.

Calculation for resistive load of electrical power generation

In terms of electrical parameters, the piezoelectric transducer behaves most similar to a capacitive element. The theoretical capacitance of the transducer is determined by

$$C = \varepsilon \frac{A}{\delta} \tag{6}$$

where ε is the permittivity of the piezoelectric material, A is the surface area, and δ is the thickness. Given the value for ε equals 3.03e-08 F m^{-1} (Piezo Systems, PSI-5H4E), the theoretical capacitance is 10.97 nF. In order to maximize the power transfer, impedance matching of the resistive load to the capacitance is performed. The relationship is approximated using a lumped parameter analysis, which gives

$$R = \frac{1}{\omega C} \tag{7}$$

where R is the resistive load. Using the ω value at the 0.660 gram payload and the theoretical capacitance, R is calculated to be 646 kΩ. Using 649 kΩ as our resistive load, we are within 0.5% of the maximum power conversion for our design.

Consumption of onboard electronics

The piezoelectric energy harvester generated sufficient power to keep many electronics typically placed onboard a flying animal operable. A list of typical electronics is shown in Table 2.5, with the highest power being the communications at 60 mW. While the RMS generated power was lower than the sensor readings and communications requirements, their power consumption is typically intermittent, and can be resolved by coupling power management electronics, like the one used in this work, to deliver sufficient higher power levels. Further research in power management technology is being explored by companies (Microstrain and Linear Technology) to

improve the efficiency of stored harvested energy for the long term, allowing energy harvester systems to power electronics during periods of non-generation as well.

Alternative energy harvesters

Other ambient sources are certainly present onboard flying animals and offer alternatives for energy harvesting technologies. Solar and thermal energy are considered to be two sources that immediately come to mind, however there are significant issues with the effective conversion of each. Solar power input levels are based on the irradiance level. With many flying animals seeking refuge from exposure to predators and others, like our species of interest the *M. sexta,* flying primarily during low to no light, irradiance levels are estimated to drop by orders of magnitude from the reported 1000 W m^{-2} [*21*]. In addition, the angle of the solar device with respect to the sun has been estimated to reduce the power conversion by as much as 80-90% [*12*].

Thermal energy exists from the difference of the body temperature to the environment and conversion efficiency is largely based on the material properties, most notably the Seebeck coefficient. The main issues with this harvester type are the direct contact it must make with the body to heat one side of the harvester to effectively transfer the thermal energy and the low material coefficients associated with these devices. To emphasize the resultant low power generation, a study on an 11^{o} C difference on a beetle with respect to its environment was demonstrated to produce only 0.8 μW [*27*]. This value is far lower than the power consumption required by the electronics and requires the design to have the device partially implanted into the specimen for a secure contact.

For these reasons, the piezoelectric energy harvester is considered a reliable electrical power generator for producing sufficient power when the electronics onboard a flying animal need them the most, when the animal is traveling. To note, a similar approach of using the cyclic motion of animal flight has been recently published by another group of researchers using an electromagnetic design [*28*]. The energy harvester, without any power management electronics, is reported to weigh 1.28 grams, and has yet to be implemented on a flying animal. Since the target animal for that work is also the *M. sexta*, it is assumed that a large unladen muscle mass ratio will be needed to allow regulation of its flight dynamics before successful implementation can be achieved. Therefore, the demonstration of our piezoelectric design offers the first known energy harvester system to produce electrical energy generation from insect flight and does so far superior to other designs, producing sufficient power to drive several onboard electronics. It is also well below the cutoff payload for the *M. sexta*, making it useful for a high percentage of specimens within that species.

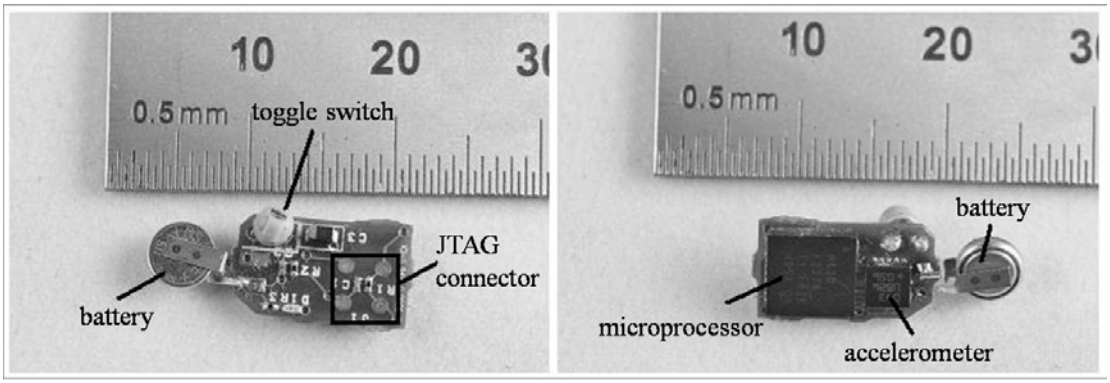

Figure 2.7: Custom onboard flight motion recording unit (left) upper side and (right) bottom side. Unit measures and records 50 seconds for all three acceleration axes with respect to the location of attachment. Circuit diagram is not included since its operation is basic, collect information from the accelerometer sensor into the microprocessor.

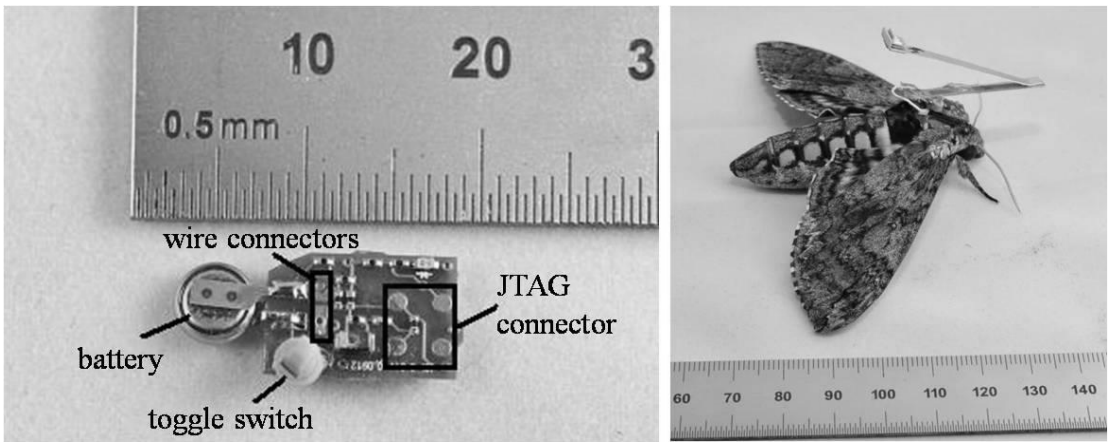

Figure 2.8: (left) Custom onboard power recording unit. Measures and records 75 seconds of the energy harvester's voltage across a fixed resistive load (649 kΩ). The bottom side (not shown) contains the microprocessor only. (right) Energy harvester connected to the power recording unit and attached to the *M. sexta*'s dorsal thorax.

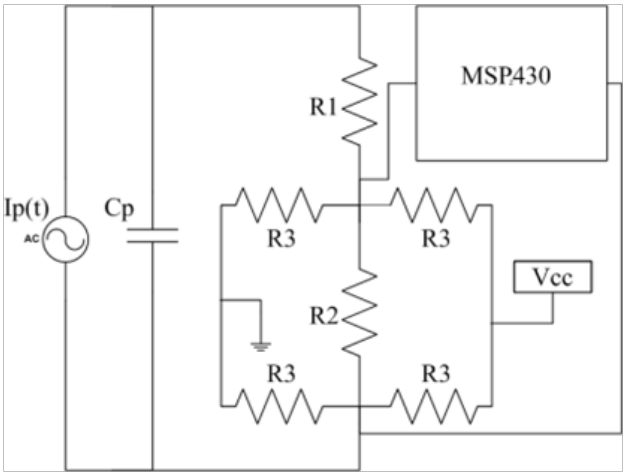

Figure 2.9: Circuit diagram of onboard power recording unit. The terms $I_p(t)$ and C_p represent the energy harvester's piezoelectric transducer and its electrical output. The variables R1 and R2 are combined in series to form the resistive load (649 kΩ). The R3 resistive bridge isolates the (R1+R2) resistive load and allows for precision measurement of the energy harvester's electrical output, by setting the impedance to the microprocessor (MSP430) to be high with respect to the resistive load.

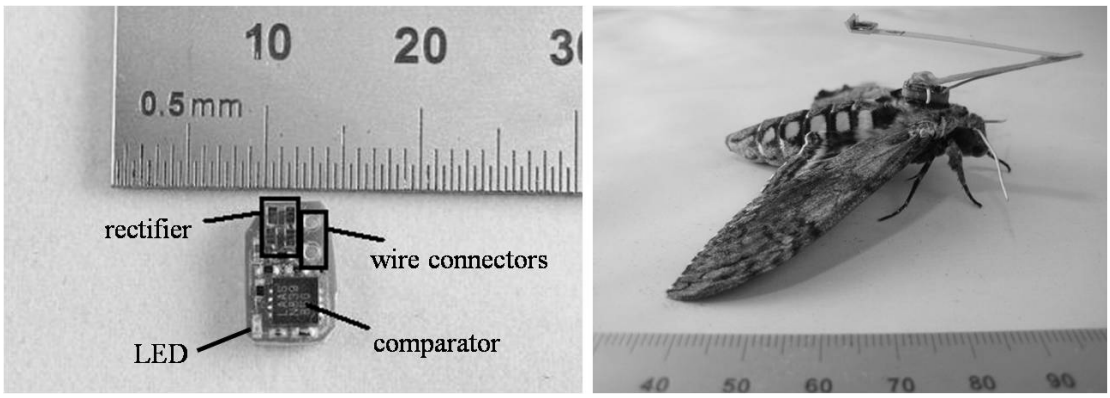

Figure 2.10: (left) Custom power management circuit. Rectifies and stores the converted electrical energy into a capacitor. The energy is then released when the capacitor's voltage reaches a threshold determined by the comparator. The result is a blink of the onboard LED. The bottom side (not shown) contains only one resistor. (right) Energy harvester connected to the power management circuit and attached to the *M. sexta*'s dorsal thorax.

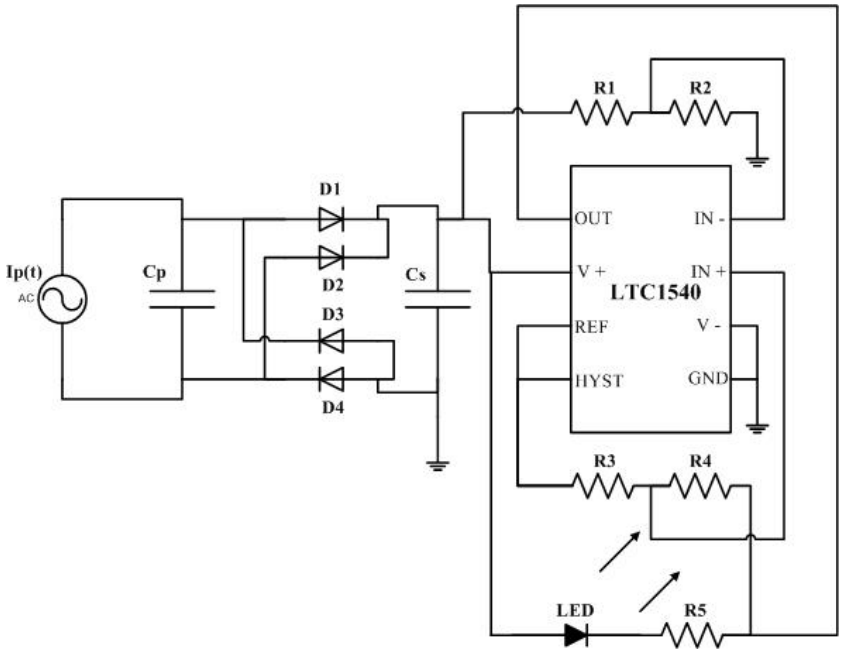

Figure 2.11: Circuit diagram of custom power management board. The terms $I_p(t)$ and C_p represent the energy harvester's piezoelectric transducer and its electrical output. A full-wave rectifier is represented by diodes D1 thru D4. The rectified electrical energy is then accumulated into a storage capacitor C_s. The comparator (Linear Technology, LTC1540) monitors the voltage of the storage capacitor, and by manipulating the resistors R1 thru R4, determines at what voltage threshold to discharge the storage capacitor's electrical energy across the LED and R5 resistor, producing a blink.

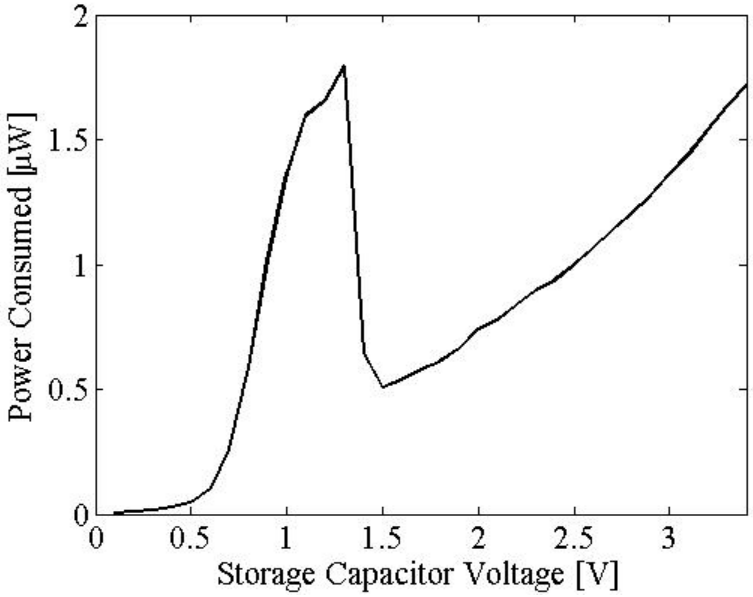

Figure 2.12: Measured power consumption by the power management circuit, obtained using a Keithley 2400 Sourcemeter.

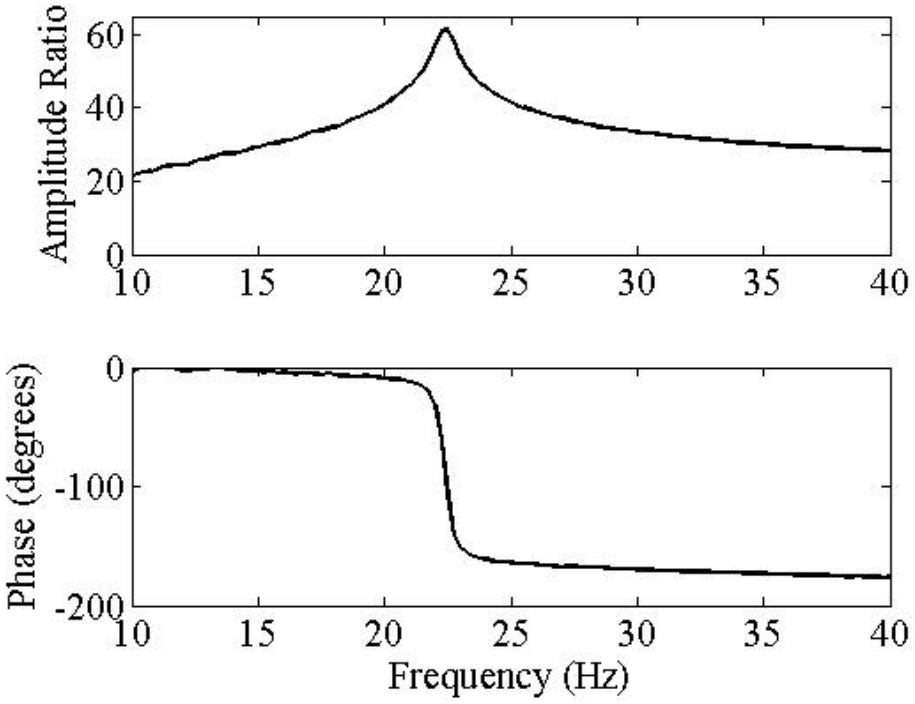

Figure 2.13: (upper) Frequency response of the amplitude ratio of the voltage generated to the input excitation voltage and (lower) the phase between the two signals. Using Bode plot analysis, the peak amplitude ratio determines the resonant frequency of the energy harvester and its damping ratio.

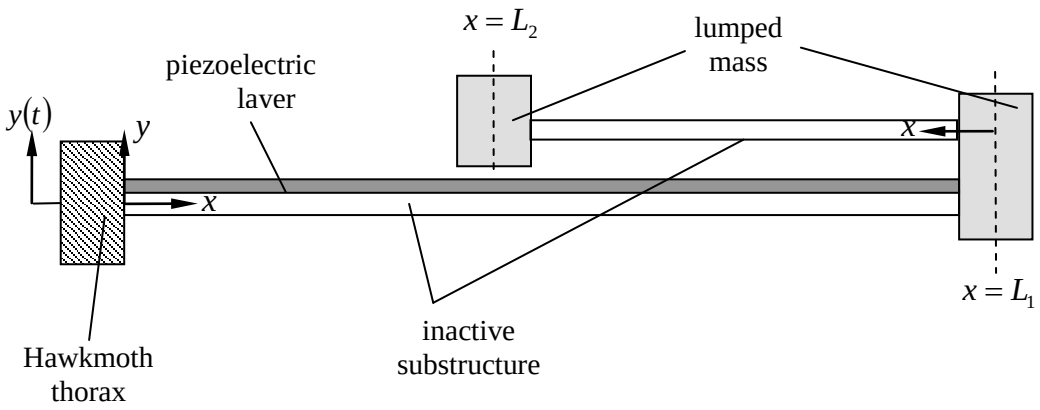

Figure 2.14: Segmented transfer matrix model of the energy harvester's folded-back topology.

Table 2.1: Hawkmoth diet and vitamin mix. This table lists the ingredients for one batch of diet, to rear hawkmoth *Manduca sexta* from larvae to the prepupal stage. It is enough food to raise approximately 48 individuals.

Hawkmoth Diet	
Ingredient (units)	Amount
Agar (g)	48
Wheat germ (g)	240
Casein (g)	108
Sucrose (g)	96
Wesson's Salt (g)	36
Torula yeast (g)	48
Cholesterol (g)	10.5
Sorbic Acid (g)	6
Methyl-p-hydroxbenzonate (g)	3
Deionized water (l)	2.2
Ascorbic acid (g)	15
Formalin (ml)	70
Linseed oil (ml)	30
Vitamin mix (ml)	12

Vitamin Mix	
Ingredient (units)	Amount
Nicotine Acid (g)	0.9
Riboflavin (g)	0.45
Thiamine (g)	0.21
Folic Acid (g)	0.21
Biotin (g)	0.018
Pyridoxine (g)	0.21
Deionized water (ml)	900

Table 2.2: Hawkmoth specimen data. This table lists the gender, body mass, and flight muscle mass (approximated as 97% of the thorax mass without the legs) measured for each specimen. Traditional payload estimates are shown to illustrate the differences in outcomes using each technique. A subset of the specific specimens that were used for the energy harvester trials is included to see individual performances.

Specimen	**Gender**	**Body Mass (grams)**	**Flight Muscle Mass (grams)**	**Maximum payload [*15*] (grams)**	**Maximum payload [*14*] (grams)**
1m:18m	male	**2.264 ±0.364**	**0.501 ±0.138**	**0.113 ±0.018**	**0.966 ±0.694**
1f:29f	female	**2.534 ±0.351**	**0.454 ±0.084**	**0.126 ±0.017**	**0.388 ±0.414**
1t:47t	**Mean**	**2.431**	**0.472**	**0.122**	**0.609**
	SD	**0.376**	**0.109**	**0.019**	**0.602**
Subset					
1	male	2.330	0.444	0.116	0.532
2	male	1.610	0.504	0.080	1.636
3	male	3.320	0.716	0.166	1.290
4	male	2.447	0.689	0.122	1.994
5	male	2.646	0.789	0.132	2.439
6	female	2.418	0.582	0.121	1.330
7	female	2.563	0.556	0.128	1.019
8	female	3.858	0.641	0.193	0.273
9	female	2.547	0.676	0.127	1.811
1:9	**Mean**	**2.64**	**0.62**	**0.132**	**1.37**
	SD	**0.63**	**0.04**	**0.03**	**0.69**

Table 2.3: Hawkmoth payload data. Specimen are shown with the vector norm of the three acceleration components (m s^{-2}) followed by a comma and then the primary body frequency (Hz). N/A indicates that the insect was unable to fly. The bottom section indicates the data used for Figure 1.4 (lower). Some payload increments were skipped for individuals in order to find the payload maximum without fatiguing the specimens with extra trials. Therefore, it was assumed that skipped lighter payloads were within the flight capability of an individual. For the subset of individuals also used to do the energy harvester trials, the number of payload trials was further reduced accordingly for this same reasoning.

		Payload Mass (grams)									
		0.359	**0.615**	**0.660**	**0.705**	**0.795**	**0.885**	**0.960**	**1.005**	**1.260**	**1.460**
Specimen	**Males (18)**	15.0, 22.9	12.9, 25.9	14.6, 23.7	14.2, 26.2	13.3, 26.2	15.7, 26.2	13.9, 23.4	15.8, 25.2	11.9, 20.7	11.5, 21.4
	Females (29)	15.4, 21.9	13.7, 25.5	14.5, 21.9	13.6, 25.9	12.9, 22.2	11.9, 25.0	12.8, 22.7	14.6, 25.0	13.1, 20.3	N/A
	All (47)	15.1, 22.6	13.5, 25.6	14.6, 23.1	13.8, 26.0	13.0, 22.8	14.0, 25.7	13.9, 23.1	15.5, 25.2	12.0, 20.6	11.5, 21.4
	1	14.7, 21.8		13.2, 22.6				12.6, 21.1		N/A	N/A
	2	16.2, 23.4		13.9, 22.6				N/A		N/A	N/A
	3	15.1, 21.9		16.8, 21.1				17.2, 21.1		16.0, 19.5	N/A
	4	15.0, 23.4		13.7, 24.2				14.6, 24.2		11.0, 18.8	10.2, 21.1
	5	14.8, 23.4		14.4, 24.2				16.0, 22.6		11.2, 18.0	12.4, 20.3
	6	14.9, 21.8		14.6, 21.1				13.3, 21.8		N/A	N/A
	7	14.6, 22.6		12.4, 23.4				12.4, 23.4		13.1, 20.3	N/A
	8	16.1, 20.3		15.7, 20.3				17.0, 21.1		N/A	N/A
	9	15.8, 22.6		15.4, 22.6				N/A		N/A	N/A
	1:9 Mean	**15.2, 22.4**		**14.5, 22.5**				**12.6, 20.1**		**7.6, 13.6**	**3.6, 8.0**
	1:9 SD	**0.6, 1.0**		**1.3, 1.4**				**4.6, 4.8**		**5.6, 6.6**	**4.7, 8.6**
	% able to fly (out of 47)	100	93.6	93.6	93.6	85.1	44.7	40.4	31.9	14.9	6.4
	Unladen muscle mass ratio	0.198 ±0.042	0.198 ±0.042	0.198 ±0.042	0.196 ±0.042	0.197 ±0.043	0.213 ±0.043	0.216 ±0.047	0.231 ±0.044	0.257 ±0.033	0.276 ±0.025

Table 2.4: Electrical output data for energy harvesters onboard *M. sexta.* Primary frequencies of the generated voltage of the energy harvester are calculated using the peak power spectral density. The estimated total vibration power is calculated for the moving 0.060 gram tip mass using the estimated acceleration from the payload study and the calculated primary frequency. The electrical power generated and the estimated total vibration power are then compared to approximate the conversion efficiency.

Specimen	**Primary Frequency (Hz)**	**Total Power Dissipated (μW)**	**Electrical Power Generated (μW_{RMS})**	**Conversion Efficiency (%)**
1	23.0	279	21.2	7.6
2	22.7	333	35.0	10.5
3	21.7	328	41.2	12.6
4	22.3	375	59.3	15.8
5	22.9	297	27.7	9.3
6	23.2	242	20.2	8.3
7	21.8	343	42.4	12.4
8	19.9	102	13.7	13.4
9	23.6	177	19.3	10.9
Mean	**22.3**	**275.1**	**31.1**	**11.2**
SD	**1.1**	**88.0**	**14.6**	**2.6**

Table 2.5: Basic power estimates for electronics onboard flying animals. The power management circuitry is presumed needed to stay on at all times, while the sensors and communications are turned on intermittently. When the power generation by the energy harvester is present, there exists sufficient power to perform any of the operations listed above, with the use of a power management circuit amplifying the power intermittently for higher power delivery.

System	**Description**	**Electrical requirements**	**Model or Source**
Traditional Power Management	Ultra-low power micrcontroller, timekeeping only	3 V, 3 μA: 9 μW	Texas Instruments, MSP 430 [*26*]
Sensors	1 byte of data read per minute for 1 ms	3 V, 200 μA: 600 μW	[*26*]
Communications	RF data transmission at 10 kbps	3 V, 20 mA: 60 mW	[*26*]

CHAPTER 3
MULTI-LAYER, STACKED SPIRAL COPPER INDUCTORS ON SILICON WITH MICRO-HENRY INDUCTANCE USING SINGLE-LEVEL LITHOGRAPHY[1]

1. Abstract

In this work, we present a structure of multi-layer spiral inductors with tens of micro-Henry inductance for use in low frequency (sub 100 MHz), power converter technology. Unique to this work is the introduction of single-level lithography over the traditional two-level approach to create each inductor layer. The result is a simplified fabrication process which results in a reduction in the number of lithography steps per inductor (metal) layer and a reduction in the necessary alignment precision. Additionally, we show this fabrication process yields strong adhesion amongst the layers, since even after a post-process abrasion technique at the inner diameter of the inductors, no shearing occurs and connectivity is preserved. In total, three separate structures were fabricated using the single-level lithography approach, each with a three-layered, stacked inductor design but with varied geometries. Measured values for each of the structures were extracted, and the following results were obtained: inductance values of (24.74, 17.25, 24.74) μH, self resonances of (9.87, 5.72, 10.58) MHz, and peak quality factors of (2.26, 2.05, 4.6) respectively. These values are in good agreement with the lumped parameter model presented.

[1] From T. Reissman, J.S. Park, E. Garcia, "Multilayer, Stacked Spiral Copper Inductors on Silicon with Micro-Henry Inductance Using Single-Level Lithography"; manuscript within open-source *Journal of Active and Passive Electronic Components*, Hindawi Publishing. This work was supported by the DARPA HIMEMS program.

2. Introduction

Over the last decade, researchers have done a considerable amount of work to model, characterize, and design air-core spiral inductors on silicon technology for both radio-frequency integrated circuits (RFIC) and monolithic microwave integrated circuits (MMIC). In comparing each work, both performance and cost are typical issues examined. For many designers, performance relates directly to improving the quality (Q) factor of these spiral inductors, which most notably has been achieved using designs such as multi-layered, stacked structures (Figure 3.1) which increase the inductance value due to the mutual magnetic coupling [1] and multiple shunt structure which lower the resistance [2,3]. For those researchers concerned with cost, much of the focus is within analyzing the process with respect to the standard complementary metal oxide semiconductor (CMOS) technology, where the key factors in determining the cost are 1) feature size, 2) number and kinds of layers, and 3) chip area occupied [4]. Within this work, we focus on simplifying the fabrication of integrated inductors for the emerging area of power converter technology. Within this growing field, researchers must again balance performance and cost issues with new requirements like the need for much higher inductance in the order of micro-Henries and operation range in the sub 100 MHz range.

Figure 3.1: Three-dimensional rendering of a stacked, in-plane spiral MEMS inductor

To highlight some examples of the balance of performance and cost issues, we cite here results from work within short-range radio frequency identifier (RFID) antennas and DC/DC converters. A typical approach in wireless technology for biomedical devices [5] and strain sensors [6] has been for researchers to use large, single in-plane coils as short-range RFIDs. Thus they balance the simplicity of single-layer inductor design with the cost of using large chip areas, which for [5] and [6] yield 2.7 cm diameters in order to meet the 4-5 μH inductance requirements. Within DC-DC converter technology, researchers have chosen to modify the single-layer CMOS fabrication by orienting the final structure orthogonal to the substrate using magnets and a hinge design, known as plastic deformation magnetic assembly (PDMA) [4]. The results are structures with 1 μH inductance and a small chip area (0.1 mm x 0.1mm), but with the added cost of increasing the difficulty with respect to the types of layers.

In this work, we introduce a simplified CMOS fabrication approach using single-level lithography in order to reduce the difficulty of the number of lithographic steps per layer over the traditional two-level lithographic approach. This simplified layer approach allows for us to then

extend the number of layers from a single-layer design to a multi-layer, stacked inductor at a lower cost over the traditional approach. To substantiate the selection of the multi-layer over single-layer design option, we compared, based on cost factors, several works aimed at achieving high-inductance monolithic inductors. From that review, we found that typical single-layer inductors used exotic substrates [7, 8] to achieve higher inductance, while multi-layered, stacked inductors on standard, silicon substrates [1, 9] were able to achieve similar, if not higher, inductance values. When examining the results with respect to the factors for cost, the latter is seemingly better with increased inductance per unit area without the need for deviation from standard CMOS procedure. Therefore, we propose that combining our potential decrease in cost per inductor layer with the simplified single-level lithography and the increased cost of using more layers with a multi-layered process, the result is still cost advantageous due to the reduction in chip area. Thus, we detail our simplified fabrication technique with respect to the standard two-level lithography approach to highlight the differences. In addition, we analyze the performance metrics of three structures fabricated using our single-level lithography approach, recording the inductance value, L, the inductance per unit area, the quality factor, Q, and the self-resonance frequency, SRF, so as to allow researchers to compare both performance and cost with future works. Lastly, we include a lumped parameter analytical model of the multi-layer, stacked inductor so as to validate the measured results.

3. Multi-layered, Stacked Spiral Inductor Theory

When designing single-layer, spiral inductors, typically a lumped parameter approximation using the π-type electrical model [10-13] is applied for simplicity, which is valid up to the self-resonance frequency, see Figure 2. This model can be viewed as an RLC circuit, where the

inductance, L_s, and capacitance, C_s, of the coil are in parallel, with losses to the substrate induced by the capacitive and conductive properties of the substrate. These and other parasitic losses vary with respect to the geometry and orientation of the inductor. Techniques for predetermining all of these elements' values have ranged from empirical expressions [12] to Greenhouse's method [11] to electromagnetic field solvers [14].

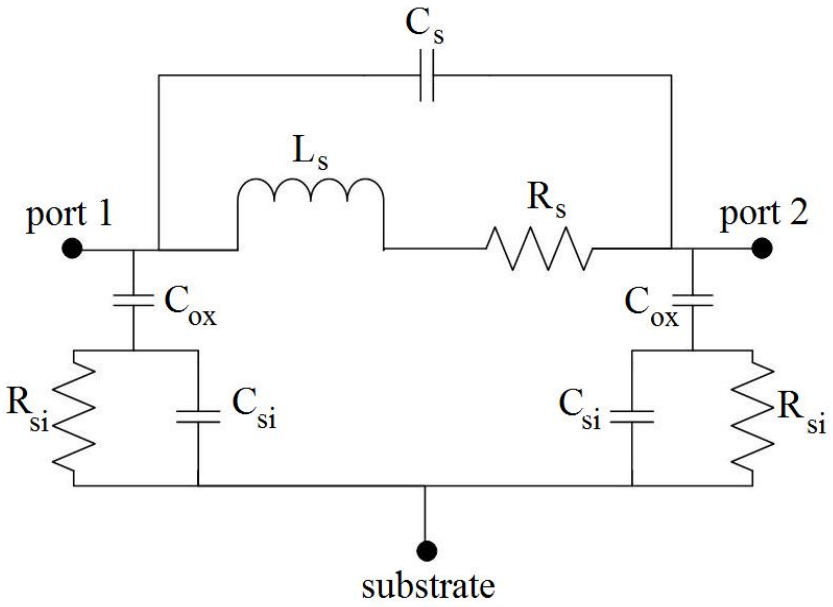

Figure 3.2: π-type electrical model of a single-layer, spiral inductor

Within this model various geometries and materials have been studied to reduce the losses and produce higher performance metrics. Specifically, some researchers have experimented with various substrate materials, Quartz, GaAs, and Sapphire [7, 8, 15], to reduce the losses brought on by the R_{si} and C_{si} components. Researchers have also experimented with creating large trenches on the under-side of the devices to increase the separation distance to the substrate and reduce the capacitive loss [16]. While these techniques are valid, they add considerable complexity and cost to the fabrication process, since they introduce costly materials and require long etching process times.

While the reduction of losses has shown improvement in inductor performance, large inductance variations can occur by manipulation of the coil geometry itself [10]. We estimate the inductance of an in-plane spiral using the zeroth order approximation given by a current sheet expression, equation (1) [12].

$$\mathrm{L} = \frac{\mu \mathrm{N}_t^2 d_{ave} c_1}{2}\left[\ln\left(c_2/\rho\right) + c_3\rho + c_4\rho^2\right] \tag{1}$$

Equation (1) assumes a non-ferrous core and that the inductance can be determined exclusively by the spiral geometry. We define μ as the permeability, N_t as the number of turns, d_{ave} as the average diameter of the turns, and ρ as the fill ratio of the single-layer spiral. The coefficients c_i are dependent on the layout of the spiral, such as square, hexagonal, octagonal, or circular. To increase the inductance value of single-layer spirals, increasing the number of turns, or N_t, is a simple and effective option.

To further increase the inductance values without increasing the turns, and thus the footprint area, we expand the single-layer spiral to a multi-layered, stacked spiral. Multi-layered, stacked spirals have been shown in the literature to increase single-layer spiral inductance values by the summation of the individual single-layer spiral inductances and their mutual inductances between layers [3, 4]. The equivalent inductance, L_{eq}, for a stacked, in-plane spiral is shown in equation (2) [12].

$$L_{eq} = \sum_{i=1}^{n} L_i + \sum_{i=1}^{n} \sum_{j=1, j\neq i}^{n} M_{ij} \tag{2}$$

The value n is the number of stacked layers, the term L_i refers to the i^{th} single-layer spiral inductance value, and the term M_{ij} accounts for the mutual inductance between each set of coils. If we assume that the inductance of each single-layer spiral is approximately the same, then Equation (2) reduces to the inductance of a single, in-plane spiral times the square of the number of stacked spirals. Thus, by interconnecting the spirals, we can increase the inductance of each spiral by a square of the number of turns and multiply that value by a square of the number of layers.

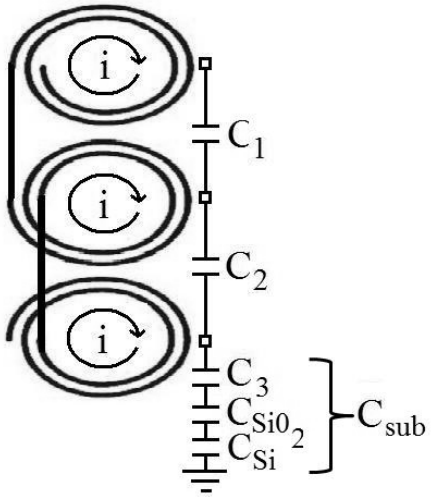

Figure 3.3: Schematic of triple-layer, stacked inductor

However, predicting only the inductance does not give an accurate estimate for the resultant reactance, or nominal inductance, of the integrated inductor which is measured by an impedance analysis. For the reactance, a relationship for the capacitance and the resistance of the device is needed as well. A general form for calculating the capacitance of two adjoining surfaces is shown in Equation (3).

$$C = \frac{\varepsilon A_{surf}}{\delta} \tag{3}$$

The term ε is the permittivity of the medium, and the term δ is the separation distance between the two facing surface areas, A_{surf}. By increasing the number of turns for a single-layer spiral, the area and capacitance also increase. To lower the capacitance while increasing the inductance, multi-layered, stacked, spirals have the following equivalent capacitance, see Figure 3.3 [1].

$$C_{eq} = \frac{1}{3n^2}\left(4\sum_{i=1}^{n-1} C_i + C_{sub}\right) \tag{4}$$

Equation (4) is derived from assuming that there exists perfect coupling between each two inductive elements, and thus the voltages in each turn are equal. The term C_i is then simply expressed as the capacitance between each of the spiral layers, which is determined by the dielectric layers in between. It is determined from Equation (4) that multi-layered, stacked spirals lower the effect that the substrate has on the total capacitance when compared to a single-layer spirals. In addition, the introduction of large separation distances between each layer, using interconnect technology [17, 18], can further reduce the equivalent capacitance and increase the SRF.

To complete the lumped parameters, the series resistance is found using

$$R = \rho l / S_{eff} \tag{5}$$

,where ρ is the conductance of the metal trace, l is the total length of the spiral inductors, and S_{eff} is the effective cross-sectional area of the trace. At zero frequency, or DC, the effective

cross-sectional area is the physical cross-sectional area of the coil's track. For low frequency designs, it can be assumed that the DC resistance is a good estimate of the actual resistance, as long as the proximity effects and skin depth effects, while present, are orders of magnitude less than the DC resistance [19].

Combining Equations (2), (4), and (5), the multi-layered, stacked inductor shown in Figure 1 has a reactance, X of [20]

$$X = 2\pi f L_{eq}\left(1 - \frac{R^2 C_{eq}}{L_{eq}} - 4\pi^2 f^2 L_{eq} C_{eq}\right) \tag{6}$$

The term f refers to the frequency of the inductor. Equation (6) approximates the multi-layered, stacked spiral as a LC circuit in parallel with a finite resistance, and thus, the when the reactance is equal to zero is the corresponding self-resonance frequency, SRF. To increase the nominal inductance, or reactance, and the useful operation range, or SRF, it is clear that maximizing the inductance and minimizing the capacitance are the key aspects of the design. Stacked, in-plane spirals are thereby an excellent choice for high inductance devices, with small footprint areas, according to these design guidelines.

A final inductor performance metric to estimate is the value of the quality factor, or Q. The Q is a measure of the ratio of the energy stored over the energy lost in one cycle. A simple expression for the Q can be estimated up to the SRF using the relationships for the resistance, Equation (5), and the reactance, Equation (6).

$$Q = X/R \tag{7}$$

Therefore, to increase the Q value for these low frequency devices, the length of the trace, which is increasing with every turn or layer to achieve a higher inductance, must be offset by a larger trace width and thickness. Both single- and multi-layered, stacked, spirals have the advantage that both the trace width and the thickness can easily be modified to larger values by creating a larger patterning mold [18].

By using the performance metric relationships listed, we have generated theoretical predictions for the measured reactance (nominal inductance), the resistance, the first self-resonance frequency, and the quality factor of stacked, in-plane spirals. We have also shown the key geometrical considerations associated with creating high inductance, multi-layered, stacked inductors. With the lumped parameter model established, we now focus on a how single-level lithography can lower the fabrication cost for these multi-layer, stacked inductor designs.

4. Device Fabrication

A major cost concern with CMOS fabrication is keeping the number of steps or processes involved, as well as the precision needed within each step, to a minimum. In accordance with these principles, to fabricate a multi-layer, stacked copper inductor, we use a single-level lithography process as opposed to the traditional two-level lithographic process. To achieve this simplified process, we use two types of photo-resists, SU-8 and SPR-220. SU-8 is a permanent photo-resist that serves as a structural layer to build the coil layers onto, as well as the dielectric material between the layers. SPR-220 is then used after evaporating the copper inductor layer to pattern the inductor using wet-etching. Thus, unlike two-level lithography, single-level lithography skips the electroplating of the patterned inductor layer, eliminating that step. After the single-level lithography, holes are made on the SU-8 layer and filled with copper using

electroplating. These copper connects create a conductive pathway from the seed layer to the first planar inductor and each subsequent planar inductor layer. By repeating these two processes, inductor layers can be stacked onto previous layers and the trace is able to maintain its connectivity through the connection holes. In addition, an extremely fast process, abrasion drilling, is introduced as a way of creating an air-core once the stacked spirals are completed. Thus, the entire process eliminates a lithographic step for each inductor layer, reducing the fabrication cost over two-level lithography.

Figure 3.4 shows a simplified version of the process. First, a silicon wafer is thermally oxidized to create an insulator between the silicon substrate and the inductor structure, reducing the parasitic substrate loss, Figure 3.4(a). Next, a tantalum layer is evaporated onto the wafer to improve the adhesion of subsequent evaporated layer, the coil's copper seed layer. The seed layer provides a pathway for electroplating the deep interconnects, Figure 3.4(b). On top of the seed layer, SU-8 2010 photo-resist solution is spun at a specified thickness, which determines the thickness of the dielectric layer (relative permittivity of 2.46), or the separation distance to the first spiral inductor layer and the resultant capacitance, C_n. We pattern the SU-8 with a standard lithography process using the connecting layer mask in order to define the interconnect position. By creating only a single, large interconnect, the precision for alignment of the spiral layer is lowered, reducing the difficulty of the lithography process. A final annealing step, of 115^{o}C for 2 minutes, is applied after developing, to improve the adhesion of the SU-8 and copper inductor layers. When the wafer is dried, it is de-scummed with oxygen plasma etching, which increases the surface roughness, to assist the adhesion of the next copper layer, Figure 3.4(c).

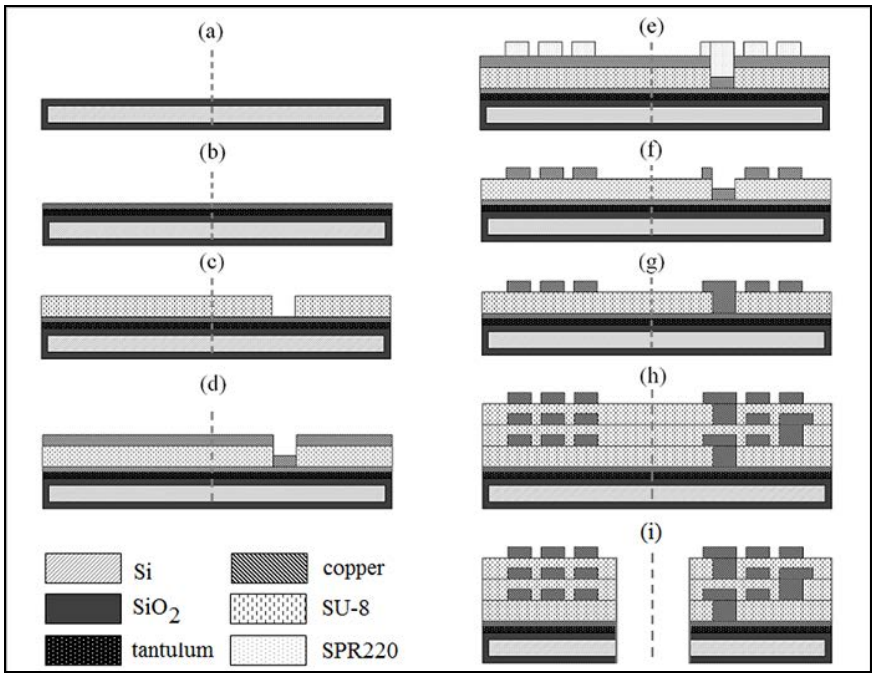

Figure 3.4: Simplified fabrication process.
Note, not drawn to scale in order to show layers.

To build each inductor layer, copper is evaporated over the entire area of the wafer at a rate less than 20 Angstroms per second, Figure 3.4(d). Next, P20 is spun to assist with the adhesion of the patterning layer, which is SPR220-7. Using a negative coil mask and a standard lithography process, the SPR220 is used to form an outline covering the in-plane spiral pattern, Figure 3.4(e). To remove the excess copper, the wafer is immersed in a copper etchant and careful attention is made to not agitate the solution, otherwise coil liftoff can occur. When the complete copper removal is visually observed, the wafer is taken out and thoroughly washed with distilled water. The area covered with SPR220 is left as the patterned inductor spiral, and the SPR220 is removed with a gentle spraying of acetone and then isopropanol, Figure 3.4(f). By doing the patterning of each in-plane spiral this way, we reduce the number of steps needed to only a single-level patterning and concurrently require only a low precision of the pattern be necessary for achieving alignment with the interconnect points between the layers, since the feature sizes

are large for micro-henry inductance. This process is significantly less difficult to achieve than most electroplating techniques used to produce coils, which require a two-level patterning lithography [18]. To explain further, in the two-level patterning, after the evaporation and patterning of the inductor, another level of photo-resist is needed in order to create channels for allowing electroplating of the inductor layer to larger thicknesses. While larger thicknesses do reduce the series resistance, the process adds another step for every inductor layer, as well as introduces the possibility of needing to do chemical metal polishing (CMP) in order to allow parallel layers for future mask alignments. So by using our single-level lithography we trade-off constraining the thickness, and the resistance, of the inductor to the limits prescribed by the evaporation process in order to reduce the fabrication cost. In applications like power converter technology, this performance tradeoff is not as critical, since the high inductance values offset the high resistance, yielding reasonable Q values. Moving on to make all the layers mutually conductive, we leave follow the standard procedure electroplate the interconnect layer.

We electroplate copper in a copper sulfate solution, Microfab SC from Enthone, Inc., at a current density of 0.02mA/mm^2 to connect the copper in-plane spiral layer to the copper seed layer using the interconnect holes, Figure 3.4(g). The rate and duration at which the electroplating process occur are dependent on the concentration of the electroplating solution and the amount of copper that needs to be deposited within the interconnect, in order to fill the hole and make an electrical connection between the layers. This process is simple because it only needs to make electrical connection with the electroplating circuit's clips to the seed layer, which are exposed at the edge of the wafer, in order to flow current and deposit copper into the interconnect. Once the first interconnect is filled, continuity to the next layer is achieved. We are therefore able to verify completion of this process by checking that continuity exists.

The two processes are then repeated from the SU-8 spinning, Figure 3.4(c), to the copper interconnect between the copper layers, Figure 4(g), creating multi-layered, stacked spirals, Figure 3.4(h). For the electroplating process, once an interconnect makes continuity with the next layer, the current will continually flow to the next interconnect. This continues until the electroplating process is deposited onto the last interconnect and makes a connection of the previous layers with the uppermost layer. Since multiple layers of in-plane spirals all need to have current flow in the same direction in order to superimpose inductance effects, a total of four masks, two for alternating connecting layer masks and two for alternating coil layer masks, are needed to construct a multiple-layer coil, see Figure 3.4. Thus the procedure requires a single-level, low precision lithography and one simple continuity test to be passed after the electroplating process. We can then conclude that the entire fabrication procedure meets many of the attributes considered for low difficulty and low cost.

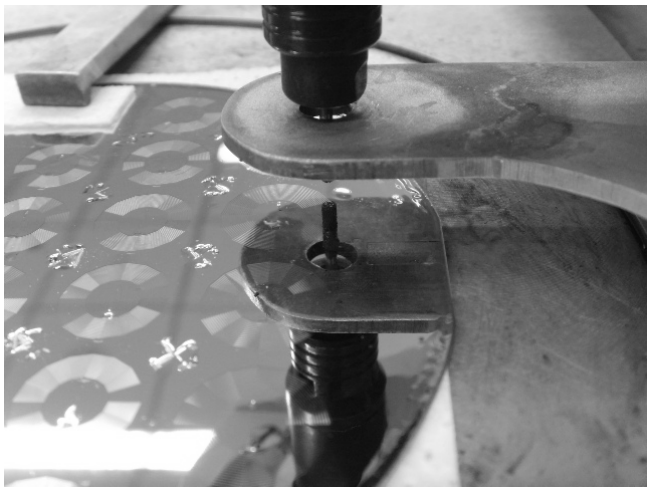

Figure 3.5: Air-core created by abrasion drilling process.

A final post processing step is performed that uses a simple, fast method for creating air-cores within these micro-fabricated stacked coils. The technique is an abrasion, or manual drilling process, in which we use a blunt, diamond-coated drill bit, sized to a diameter smaller than the

structure’s inner diameter, to create a through hole at the center, Figure 3.4(i). By applying light hand pressure using a micro drill and manually turning the drill bit, a hole is created in the inner diameter of the multi-layer coil within seconds, which is far faster than etching techniques previously used in the literature for creating cavities [1], Figure 3.5. In addition to the improvement on time, this step shows that with the fabrication technique described for producing the stacked spirals, the single-level lithography provides enough adhesion and support structure to maintain the inductor’s structural integrity and connectively even under abrasion, bending and shear forces.

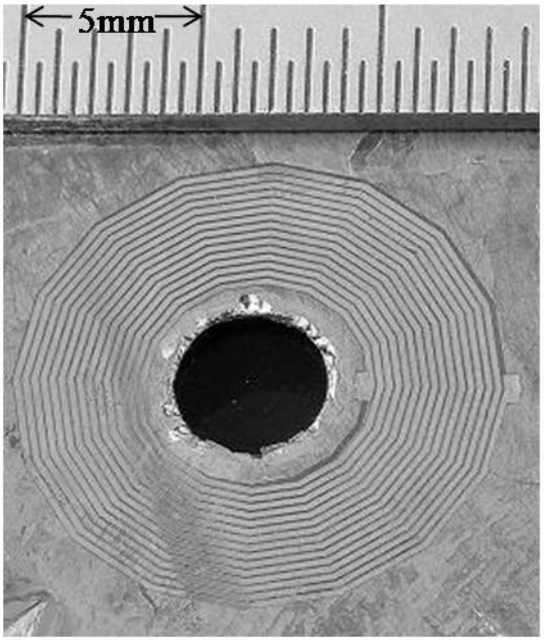

Figure 3.6: Overhead view of triple-layer coils with air core.

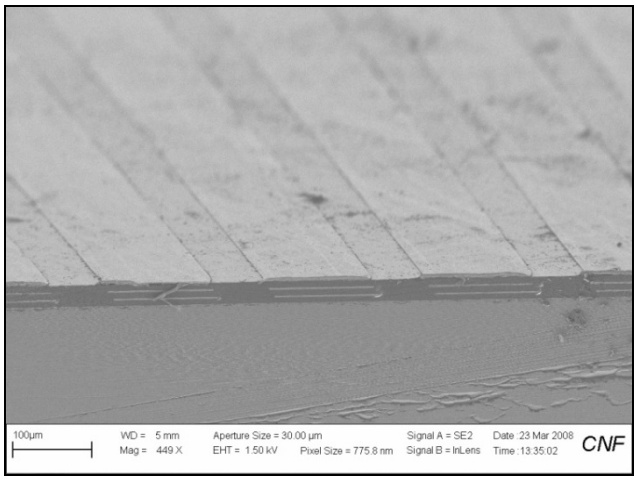

Figure 3.7: SEM cross-sectional image of triple layer coil.

Figure 3.6 shows an overhead view of a stacked, in-plane spiral coil fabricated with the process described and with the inner core removed by the abrasion process. Each hash mark in the overhead scale depicts 500 µm increments. Figure 3.7 shows a cross-sectional cut of the coil in Figure 3.6, where the sections of light gray matter are the copper coil layers, and the dark gray matter are the SU-8 support layers.

5. Device Characterization and Results

Using the single-level lithography fabrication technique, we made three multi-layered, stacked inductors (each with 3 inductor layers in series) with varying trace widths, trace thicknesses, and spacing between layers, see Table 3.1. Designs were chosen by setting the nominal inductance value close to 20 µH and with performance measured for each design variation. Measurements were performed using a HP4194 impedance analyzer and on-chip cascade probes, with averaging of the two-port s-parameters of the spirals from 150 kHz to 15 MHz frequency range. Averages were performed using 401 sample points distributed linearly over the frequency range, with 32 trials at each frequency point. Pad capacitance was de-embedded by subtracting out the open-

circuit structure y-parameters from the spiral y-parameters. The calibration procedure we used is the standard approach and is reported widely [14]. Values for the nominal inductance, resistance, SRF, and quality factor were determined from these measurements and compared to theory.

Table 3.1: Stacked, in-plane spiral coil geometry variations.

Design	1	2	3
Track width (μm)	150	200	150
Track thickness (μm)	1.1	1.6	2.1
Track spacing (μm)	50	50	50
Track turns per layer	15	15	15
Inner diameter (mm)	6	6	6
Outer diameter (mm)	12	13.5	12
Dielectric layer (SU-8 photoresist) (μm)	30	10	30
Number of stacked spirals	3	3	3
Coil volume (mm^3)	10.54	4.98	10.9

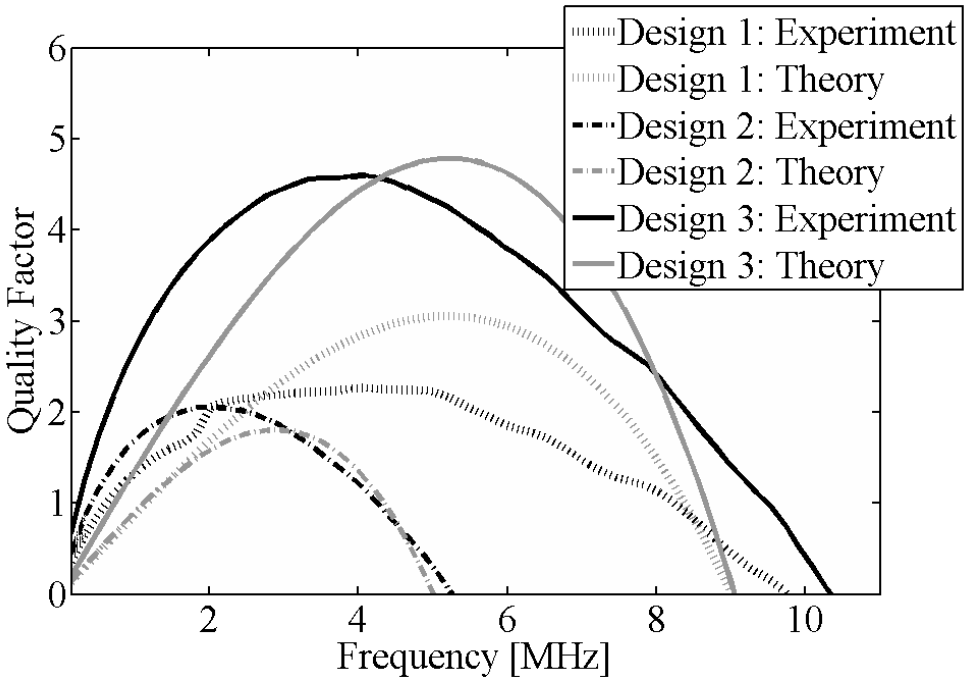

Figure 3.8: Multi-layered, stacked inductor designs with variable geometries.

We observed general agreement between our lumped parameter model and our experimental results for nearly all metric values, see Figure 3.8 and Table 3.2. The only exception was the prediction for the maximum Q of Design #1, which has an unusually flat Q curve over its measured range. Since all other predictions lie within acceptable experimental results, less than 15%, we assume the model is an accurate first order approximation up to the self resonance frequency. The theory is particularly useful in modeling the reactance of the device and accurately predicting its effect on the performance values of interest. Taking this effect into account we can design for a desired nominal inductance and self-resonance frequency, and expect device performance to closely correlate. The nominal inductance is defined in Table 3.2 as the linear slope of the reactance and the corresponding frequency, f, between an initial value in the low frequency range and a final value before the SRF.

$$L_{nom} = \frac{\left(X_{final} - X_{initial}\right)}{2\pi\left(f_{final} - f_{initial}\right)} \tag{8}$$

By designing the SRF higher than an operating range of approximately 1 MHz, we are able to show a constant nominal inductance of approximately 20 μH for all three designs, see Table 3.2.

Table 3.2: Performance results for geometry variations

		Values @ 1 MHz				
		Nominal inductance (μH)	Nominal inductance / footprint area (nH/mm^2)	Resistance (Ω)	Q (maximum)	SRF (MHz)
Design 1	Theory	26.59	235.1	120.7	3.05	9.11
	Measured	24.74	218.8	120.8	2.26	9.87
	Error	*7.5%*	*7.5%*	*0.1%*	*35%*	*7.7%*
Design 2	Theory	19.19	134	65.6	1.8	5.1
	Measured	17.25	120.5	66.5	2.05	5.72
	Error	*11.2%*	*11.2%*	*1.4%*	*12.2%*	*10.8%*
Design 3	Theory	26.82	237.2	60.4	4.78	9.12
	Measured	24.74	218.8	59.1	4.6	10.58
	Error	*8.5%*	*8.5%*	*2.2%*	*3.9%*	*13.8%*

We examine the results of the parametric analysis, which holds all design values to approximately constant nominal inductances, and see that with our fabrication technique performance metrics such as the Q, SRF, and size can be improved. For design 2, we increase the thickness by 50% and the width by 30% above the respective values in design 1. This reduces the resistance by nearly half, in order to improve the Q. Additionally, in design 2 we reduce the coil's size by reducing the thickness of the SU-8 layer, the dielectric layer between the stacked inductors, to one third its original value. Lowering the separation distance between the coils increases the capacitance, which reduces the SRF, and is therefore disadvantageous. However, by combining the two changes in design 2, the benefits of the resistance improvements outweigh the capacitive disadvantages for the 1MHz range and below. Design 2 demonstrates

experimentally a constant Q, with a value near 2, for a volume of only one half that of design 1. Focusing on further improving the Q factor over design 2, design 3 uses the same SU-8 layer thickness between coil layers and the same coil patterning as design 1, but increases the trace thickness to twice that of design 1, which reduces the resistance by one half. The Q factor for design 3 is therefore nearly twice that of design 1, while the SRF is relatively maintained because the footprint area remains the same as in design 1. The only disadvantage to design 3 is that the increased trace thickness results in a slight 3.4% increase in the stacked coil's volume compared to design 1. From this parametric analysis, we are able to show the variation in performance metrics for changes in the geometry of these high-inductance devices.

When comparing these results to the literature [1, 9], these stacked, in-plane spirals stand in an inductance class entirely by themselves. Previous researchers focused on maintaining *SRF* values close to or within the GHz range to allow for RF applications and resulted in inductance values limited to hundreds of nano-Henries. Our devices demonstrate tens of micro-Henries inductance, and maintain Q factors at 2 to 4.6. Through optimization, a balance in designs for appropriate inductance, self-resonance, and Q could be made. Thus this new class of inductors demonstrates useful theory and simplified fabrication for achieving these performance metrics as well as potentially reduced cost for low frequency range applications.

6. Conclusions

Given the need for high-inductance devices in power converter technology, our main goal in this work was to simplify the CMOS process while increasing the performance of multi-layer, stacked inductors for low frequency range operation. We found that to achieve micro-Henry

inductance values, the multi-layer, stacked inductor design required a balance between a large number of turns per layer and a large number of stacked layers. In addition, to lower the manufacturing difficulty to achieve such a design, a reduction in the number of lithographic steps as well as an increase in feature size was crucial. Key points include the use of a single-level patterning for the lithography of each inductor layer, and the creation of large interconnects via electroplating process, which allows for a low required alignment between spiral layers. The large interconnect (dielectric) layers also preserve the large nominal inductance values by reducing the capacitive effect. Lastly, a fast abrasion drilling method was implemented to create air-cores, which reduces the time required to produce the cavity to mere seconds and represents a significant time savings compared to etching. Together, these simplified methods result in a low cost fabrication method for micro-Henry inductance integrated inductors. In summary, the single-level lithography fabrication process in conjunction with the multi-layer, stacked design produced devices exhibiting performance and cost metrics for improving existing power converter technology.

REFERENCES

[1] A. Zolfaghari, A. Chan, B. Razavi, "Stacked inductors and transformers in CMOS technology," *IEEE J. of Solid-State Circuits* **36**(4), p. 620-628, (2001)

[2] D. Suh, B. Mheen, "Analysis on the effect of parallel current path on the quality factor of CMOS spiral inductors for 1-10 GHz," *IEEE J. of Solid-State Circuits*, **77**, p. 292-296, (2005)

[3] O.H. Murphy, K.G. McCarthy, C.J.P. Delabie, A.C. Murphy, P.J. Murphy, "Design of multiple-metal stacked inductors incorporating extended physical model," *IEEE Trans. On Microwave Theory and Techniques*, **53**, p. 2063-2072, (2005)

[4] S. Musunuri, P.J. Chapman, J. Zou, C. Liu, "Design issues for monolithic DC-DC converters," *IEEE Trans. On Power Electronics*, **20**, p. 639-649, (2005)

[5] C.H. Yang, J.H. Chien, B.Y. Wang, P.H. Chen, D.S. Lee, "A flexible surface wetness sensor using a RFID technique," *Biomed Microdevices*, **10**(47), p. 47-54, (2008)

[6] Y. Jia, K. Sun, F.J. Agosto, M.T. Quinones, "Design and characterization of a passive wireless strain sensor," *Meas. Sci. Technol.*, **17**, p. 2869-2876, (2006)

[7] C. Leroy, M.B. Pisani, C. Hibert, D. Bouvet, M. Puech, A.M. Ionescu, "High quality factor copper inductors integrated in deep dry etched quartz substrates," *Proc. DTIP MEMS MOEMS*, ISBN: 2-916187-0-0, (2006)

[8] J.M. Lee, I.H. Choi, "Frequency responses of circular spiral inductors for GaAs RF MMIC applications," *J. Korean Physical Society*, **38**(2), p. 123-128, (2001)

[9] S.J. Pan, L.W. Li, W.Y. Yin, "Compact equivalent circuit model of two-layer spiral inductors," *IEEE RF Microwave Eng*, p. 148-153, (2003)

[10] H.A. Wheeler, "Simple inductance formulas for radio coils," *Proc. IRE*, **16**(10), p. 1398-1400, (1928)

[11] H.M. Greenhouse, "Design of planar rectangular microelectronic inductors," *IEEE Trans. Parts, Hybrids, Packag.*, **PHP-10**, p. 101-109, (1974)

[12] S.S. Mohan, "Modeling, design, and optimization of on-chip inductors and transformers," Ph.D. Thesis Stanford University, (1999)

[13] N.J. Oh, S.G. Lee, "A simple model parameter extraction methodology for an on-chip spiral inductor," *ETRI Journal*, **28**(1), p. 115-118, (2006)

[14] A.M. Niknejad, R.G. Meyer, "Analysis, design, and optimization of spiral inductors and transformers for Si RF Ics," *IEEE J. Solid-State Circuits*, **33**, p. 1470-1481, (1998)

[15] R.A. Johnson, C.E. Chang, P.M. Asbeck, M.E. Wood, G.A. Garcia, I. Lagnado, "Comparison of microwave inductors fabricated on silicon-on-sapphire and bulk silicon," *IEEE Microwave and Guided Wave Letters*, **6**(9), p. 323-325, (1996)

[16] M.C. Hsieh, D.K. Jair, Y.K. Fang, C.S. Lin, "Design and fabrication of the suspended high-Q spiral inductors with x-beams," *Proc. DTIP MEMS MOEMS*, ISBN: 978-2-35500-000-3, (2007)

[17] I.J. Bahl, "High current handling capacity multilayer inductors for RF and microwave circuits," *IEEE RF Microwave Eng*., p. 139-146, (2000)

[18] C. Massin, G. Boero, F. Vincent, J. Abenheim, P.A. Besse, R.S. Popovic, "High-Q factor RF planar microcoils for micro-scale NMR spectroscopy," *Sensors and Actuators A,* **97-98**, p. 280-288, (2002)

[19] J.D. Jackson, "*Classical Electrodynamics,"* Wiley, (1975)

[20] L. Qinghua, "Stacked Spiral Inductor Design and Modeling for fully-Integrated DC-DC Converters," *Applied Mechanics and Materials*, **135-136**, p. 918-923, (2012)

This chapter originally appeared as:

T. Reissman, J.S. Park, E. Garcia, "Multilayer, Stacked Spiral Copper Inductors on Silicon with Micro-Henry Inductance Using Single-Level Lithography" *Journal of Active and Passive Electronic Components*, Volume 2012, Article ID 871620, doi:10.1155/2012/871620

CHAPTER 4
TRANSFER FUNCTION IDENTIFICATION OF THERMALLY-ACTUATED MEMS WITH FULL HEAT TRANSFER ANALYSIS[1]

1. Abstract

In this paper the dynamics of MEMS devices is explored, which characterizes the behavior of a thermally-actuated MEMS in order to perform a system identification enabling controlled operation of the micro-device. By considering the input to the system is the current/voltage and the output is the amplified mechanical displacement, a transfer function, TF, is derived which includes energy losses due to the imperfect energy conversion from electric to thermal, and which correspond to various phenomena, such as convection, radiation and conduction – accounting for a Joule-effect temperature less than the ideal one. This TF also includes the relationship between temperature and the mechanical deformation of both "active and passive" flexure hinges, which are thermally-actuated and which contribute to the kinematics of the output motion of the micro-device. This TF model is validated by means of experimental data from an actual displacement-amplification MEMS which was fabricated by means of the PolyMUMPs surface machining technology.

2. Introduction

Since the creation of MEMS technology, many micro-devices have been fabricated to utilize the transfer of electrical energy into thermal actuating mechanisms. The realization of this technique

[1] From Reissman, T., Lobontiu, N., Nam, Y., and Garcia, E. "Transfer Function Identification of Thermally-Actuated MEMS with Full Heat Transfer Analysis," originally submitted to open-source *Journal of Micro and Nanosystems*, Bentham Science, Inc. This work was supported by a National Science Foundation Grant.

for energy transduction is that a multitude of material properties must be known in order to precisely model the TF. Recent research has followed the method of either formulating simulation data using programs such as SPICE or ANSYS to solve the thermal analysis or using simplified analytical methods satisfying conditions specific to their devices, i.e. conduction only assumptions [1,2,3]. The following analysis breaks free from these assumptions and their inherent partial representations to provide the full analytical thermal analysis for such actuators, so as to gain a clear understanding of the temperature gradient involved in the TF.

With the temperature profile for the actuator accurately described, the steps for conversion of thermal energy into displacement or force simply become an application of the coefficient of thermal expansion. Care must be taken though not to exceed the recrystallization temperature which is lower than the melting point [4]. The recrystallization temperature is associated with a drift in the resistance of the material and will alter the expected output as the material properties change, thus limiting the model to an operating condition within this temperature bound.

The final outcome therefore for thermal actuators in MEMS is to correctly characterize the transformation from electrical input to force or displacement output. The following mathematical model shows the complete thermal analysis for micro-beams, including conduction, radiation, and convection, and couples the temperature output to the thermal expansion force.

3. Mathematical Model

Thermal actuation at the micron level utilizes small geometries in order to reach steady-state temperatures quickly, on the order of micro-seconds, and with low-energy input, on the order of milliwatts. Ideally forced convection would be avoided when designing for an optimal thermal

actuator so as to concentrate the temperature gradient on the actuator itself; however in reality this case rarely exists and for completeness convection is presented with a study of natural convection and with forced convection. As will be shown, even small velocities can significantly affect the total convective energy loss within MEMS.

The starting point for the thermal analysis begins with the law of conservation of energy using the micro-actuator as the control volume. The balance of energy input and output must be equal at steady state. Thus the analysis is not a transient analysis, but one in which the designer can learn the delay time inherent in reaching the actuator's final steady-state output. Using the premise that one is designing these thermal actuators for repeated use, as in the control of a MEMS device, we are concerned primarily with operating the actuators well below any thermal melting or material property changing range, such as the recrystallization point, and in so focus on the final output of the actuator rather than the transient change in the temperature profile. Thus, the surface energy balance equation at steady-state is,

$$\dot{E}_{in} - \dot{E}_{out} = 0 \tag{1}$$

Several assumptions are therefore applied to the analysis. First, conduction to a semi-infinite solid, substrate, occurs by means of a thermal contact resistance, consisting of the air layer, the silicon-nitride layer, and the silicon substrate. Second, radiation loss can be estimated at all exposed surfaces using the steady-state conduction-only model temperature values. Third, natural and forced convection occur on the exposed surfaces of thermal actuator and have a superposition effect on one another.

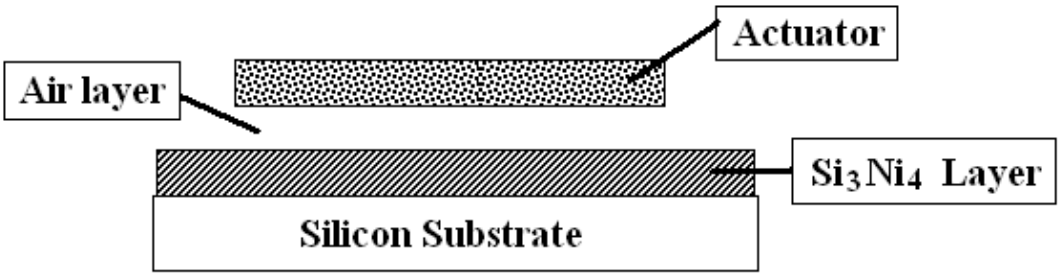

Figure 4.1: Side-view of thermal actuator setup

The thermal analysis utilizes the methodology for 'conduction with thermal energy generation' [5]. In the case of the actuators, thermal energy is generated by ohmic or resistive heating, in which electrical energy is converted to thermal energy. Commonly, this rate of energy generation can be considered equal to the power input into the actuator,

$$\dot{E}_{gen} = P_{in} = I^2 R = IV \tag{2}$$

Equation (2) shows each of the equalities applying Ohm's law. The energy generation equation is a volumetric generation rate (W/m^3) and is uniformly distributed throughout the medium,

$$\dot{q}_{in} = \frac{P_{in}}{V_{ol}} \tag{3}$$

The difference in this model from previous thermal actuator models (Lott, et. al) is the use of Equation (3) for the energy generation as opposed to using the current density function with the material's resistance. Several problems make the current density function difficult to estimate, such as accurately estimating the initial resistivity and thermal coefficient of resistance (TCR) for various geometry and additive dopants, which are also dependent upon knowing the temperature difference between the actuator and its surroundings at all times. Equation (3) uses a transfer function approach in which the designer simply needs to know the power input to the actuator and desires to know the resultant output.

4. Thermal Analysis

4.1 Conduction-Only Thermal Analysis

In order to derive the temperature distribution within the MEMS actuator, a 'plane wall' analysis is evaluated with uniform heat generation, constant thermal conductivity, and constant surface temperatures for each specific location along the actuator. The general uniform heat generation equation then simplifies to,

$$\frac{\partial^2 T}{\partial x^2} + \frac{\dot{q}_{in}}{k_a} = 0 \tag{4}$$

,where the general solution takes the form,

$$T(x) = \frac{\dot{q}_{in} L^2}{2k_a}\left(1 - \frac{x^2}{L^2}\right) + \frac{T_{x=L} - T_{x=-L}}{2}\frac{x}{L} + \frac{T_{x=L} + T_{x=-L}}{2} \tag{5}$$

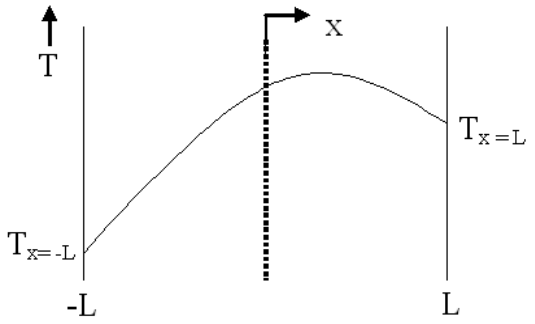

Figure 4.2: Pictorial of approximate temperature profile along the actuator

Assuming that at x=-L the surface temperature is at or near ambient, since the starting point is connected to a large sink, the probe contact pad, another equation is necessary to determine the

value at the opposing end of the actuator, $T_{x=L}$. Applying an approximated surface energy balance at $T_{x=L}$, neglecting radiation and convection, the rate of energy generated combined with the energy lost must subside to zero as prescribed in Equation (1),

$$-k_a A_s \frac{\partial T}{\partial x}\Big|_{x=L} = \frac{S}{R_t}(T_{x=L} - T_{sub}) \tag{6}$$

,where the shape factor, S, accounts for the vertical walls of the actuator [2], and the thermal contact resistance of conductivity is the path leading to the substrate, or infinite medium. Both variables must be determined through geometrical analysis and material properties [6-9]. The solution to Equation (6) thereby takes the form,

$$T_{x=L} = \frac{\dot{q}_{in} A_s x}{\frac{S}{R_t} + \frac{k_a A_s}{2L}} + T_{x=-L} \tag{7}$$

Lastly, in order to determine the time to reach these steady-state values, the following equation is used,

$$\rho V_{ol} c \frac{\partial T}{\partial t} = -\frac{S}{R_t}(T_{x=L} - T_{sub}) \tag{8}$$

From Equation (8), the time to steady-state can be found by applying the initial conditions and some simplifications using variable substitutions. After substituting and integrating Equation (8), the solution to the steady-state time settles to a function of geometry and material constants,

$$t = \frac{\rho V_{ol} c R_t}{S} \ln\left(\frac{2L\left(\frac{S}{R_t} + \frac{k_a A_s}{2L} \right)}{k_a A_s} \right) \tag{9}$$

4.2 Full Energy Loss Thermal Model

A basis has now been developed for evaluating the differences between a conduction only model and the non-partial solution, to give the designer an analysis tool to evaluate what conditions the effects of radiation and convection cannot be assumed negligible [10]. The non-partial solution however is the full surface energy balance equation, taking into account all thermal losses, which is of the form,

$$-k_a A_s \frac{\partial T}{\partial x}\Big|_{x=L} = \frac{S}{R_t}(T_{x=L} - T_{sub}) + \varepsilon\sigma A_{\exp}(T_{x=L}^4 - T_{med}^4) + \bar{h} A_{\exp}(T_{x=L} - T_{med}) \tag{10}$$

where the additional two terms from Equation (6) denote radiation and convection losses in that order. As can be seen, two complications arise when attempting to solve this equation for $T_{x=L}$. The first difficulty is the radiation loss is nonlinear with a 4th power temperature dependence. The second difficulty is the convective loss has a changing coefficient $\bar{h}$ with respect to the surface temperature difference. The following sections include methods to solve such complications.

4.2.1 Radiation Term

The 4th power nonlinearity temperature dependence for the radiation loss can be solved by linearizing the radiation heat transfer coefficient h_r,

$$h_r \equiv \varepsilon\sigma\left(T_{x=L} + T_{med}\right)\left(T_{x=L}^2 + T_{med}^2\right) \tag{11}$$

which uses Equation (7) for an estimate of the initial temperature distribution at the point x=L. The radiation loss is now linear,

$$q_{rad} = h_r A_{\exp}(T_{x=L} - T_{med}) \tag{12}$$

4.2.2 Convection Term

The convection term is typically assumed to be neglected because the thermal conductivity of the medium is much less than the thermal conductivity of the actuator. However, this is not the only variable in the convective term, and henceforth should be evaluated for magnitude, especially if considering using mediums other than air, as in microfluidic systems. To evaluate the magnitude of influence of the convection case, the convection coefficient must be solved for,

$$\bar{h} = \frac{\overline{Nu}_{2L} k_{med}}{2L} \tag{13}$$

To solve for the convection coefficient, an analysis must be made as to whether forced or free convection dominates, or if a superposition of the two effects should be used. The reasoning behind this is that the determination of the Nusselt number is dependent upon knowing which state the flow field surrounding the actuator is immersed in. To perform this evaluation, the following set of equations are used,

$$\begin{aligned} (Gr_{2L} / \mathrm{Re}_{2L}^2) &>> 1 \text{ ,free convection dominant} \\ &<< 1 \text{ ,forced convection dominant} \\ &\approx 1 \text{ ,combined effects must be evaluated} \end{aligned} \tag{14}$$

4.2.2.1 Free Convection

For the first condition of Equation (14), a free convection only analysis can be assumed. The Nusselt number, $\overline{Nu_{2L}}$, is a function of the Rayleigh number, where some important considerations when solving for the Rayleigh number are the film temperature is assumed to be the average of the surface and medium's temperatures, and the medium's properties are dependent upon the film temperature. It is thus apparent that the Rayleigh number is highly dependent upon the length of the actuator, with a cubic dependence, which for MEMS devices will typically drive the value to be relatively small, on the order of less than 10^4. In order to determine the exact correlation of the Nusselt number to the Rayleigh number, heat transmission analysis must be applied below typical macro-scale ranges, which have Rayleigh numbers above the 10^4 range [11,12]. Thus, an approximation for the coefficient and exponent must be made using an extension of the low Rayleigh range from the data correlation by Saunders [13].

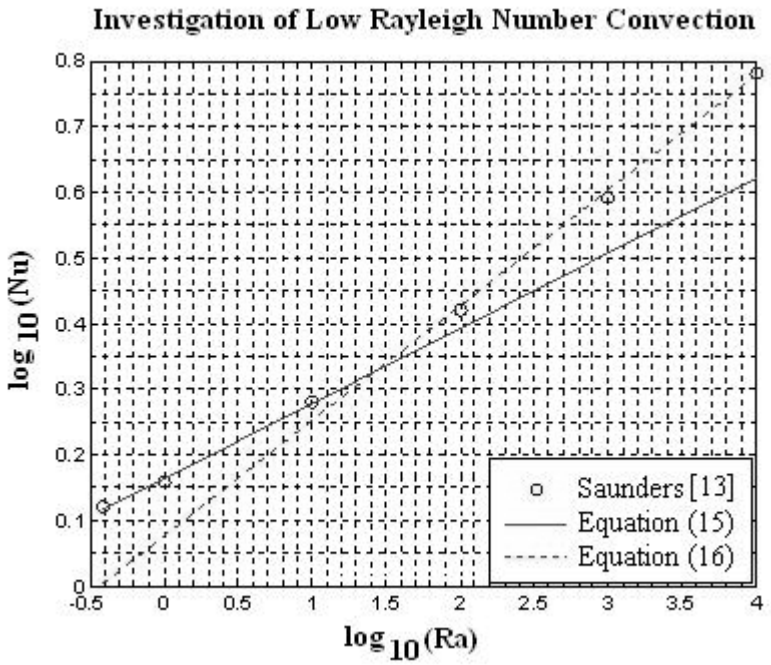

Figure 4.3: Low Rayleigh number correlations to vertical plates

A study of the literature shows strong correlation of these data points with other experiments using horizontal plates, allowing the same formula to be used for flat and vertical sides of the actuator [14 - 17]. Hence the following new formula extension can be made to the range of the Rayleigh number correlation to the Nusselt number by using a best fit approximation to the lower bound of the Rayleigh number range,

$$\overline{Nu}_{2L} = 1.44 Ra_{2L}^{1/8} \qquad 10^{0} \le Ra_{2L} \le 10^{1.5} \tag{15}$$

$$\overline{Nu}_{2L} = 1.24 Ra_{2L}^{1/6} \qquad 10^{1.5} \le Ra_{2L} \le 10^{4} \tag{16}$$

4.2.2.2 Forced Convection

For the second condition of Equation (14), forced convection is assumed. The convection coefficient follows the same formula as Equation (13) and so for a laminar flow over the actuator the governing equation is [18,19],

$$\overline{Nu}_{2L} = 0.664\,\mathrm{Re}_{2L}^{1/2}\,\mathrm{Pr}^{1/3} \qquad \mathrm{Pr} \geq 0.6 \tag{17}$$

Laminar flow can generally be assumed valid for most MEMS devices since the Reynolds number is typically small due to the actuator's length scale. While it generally follows that the Reynolds number confines the medium to within the realm of laminar flow, it is possible that the mean velocity could be extraordinarily large, and hence, for completeness, the turbulent flow formula using a modified Reynolds, or Chilton-Colburn, analogy for the Nusselt number is [20],

$$\overline{Nu}_{2L} = 0.037\,\mathrm{Re}_{2L}^{4/5}\,\mathrm{Pr}^{1/3} \qquad \mathrm{Re} >> 5x10^{5} \tag{18}$$

4.2.2.3 Superposition of Free and Forced Convection

For the third condition of Equation (14), both free and forced convection are assumed to be similar in magnitude, and thus both must be considered for the formulation of the Nusselt number used to derive the convection coefficient. The mixed convection Nusselt number is a superposition of the forced and free,

$$\overline{Nu}_{2L} = \overline{Nu}_{2L,\,forced} \pm \overline{Nu}_{2L,\,free} \tag{19}$$

The terms are additive with assisting and transverse flows, and negative when the flows are opposing. This superposition of terms is an approximation since it is dependent on the contribution of the medium's flow, however an investigation of the mixed convection problem indicates it as an accurate analysis for the Nusselt number [21-26].

4.2.3 Combining The Three Thermal Losses

Equation (10) includes a set of internal equations to find the steady-state asymptotic solution by using the methodology above. The equation can then be checked against the conduction-only model, Equation (6), to quantify the effects of conduction, radiation, and convection at the micron-level. The final full surface energy balance equation is then,

$$T_{x=L,\,full} = \frac{\dot{q}_{in} A_s x}{\frac{S}{R_t} + \frac{k_a A_s}{2L} + h_r A_{\exp} + \bar{h} A_u} + T_{x=-L} \tag{20}$$

Using the same variable substitution and integration technique for Equation (9), the time to reach steady-state for the full thermal model is,

$$t_{full} = \frac{\rho V_{ol} c}{\left(\frac{S}{R_t} + h_r A_{\exp} + \bar{h} A_u \right)} \ln \left(\frac{2L \left(\frac{S}{R_t} + \frac{k_a A_s}{2L} + h_r A_{\exp} + \bar{h} A_u \right)}{k_a A_s} \right) \tag{21}$$

5. Force Analysis

For isotropic materials, a linear thermal expansion can be assumed. This linear assumption provides a correlation for the rate of change of unidirectional strain with respect to the temperature difference,

$$\alpha_T = \frac{\partial \varepsilon_{uni}}{\partial T} \tag{22}$$

As a reference, polysilicon's CLTE ranges from 2.57 to 2.7E-06 K^{-1} [27]. To determine the total strain, a superposition of the initial and thermal strain is analyzed,

$$\varepsilon_{uni}(T) = \varepsilon_{uni}(T_0) + \alpha_T \bullet \Delta T \tag{23}$$

Using the unidirectional stress relationship, the correlation of the thermal expansion to the unidirectional force is calculated,

$$\sigma_T = \frac{F_{uni}}{A_s} = E\varepsilon_{uni} \tag{24}$$

Thus the transfer function relating force to an input voltage can be determined based on the solution to the incremental change in the temperature distribution,

$$F_{uni} = EA_s \bullet \left(\varepsilon_{uni}(T_0) + \alpha_T \bullet \left(\frac{\dot{q}_{in} A_s x}{\frac{S}{R_t} + \frac{k_a A_s}{2L} + h_r A_{\exp} + \bar{h} A_u} \right) \right) \tag{27}$$

5. Results and Discussion

With a mathematical model of the system now derived, a TF analysis can be performed to analyze the thermal actuation of a MEMS device. Figure 4.4 depicts such a thermal drive for a MEMS device.

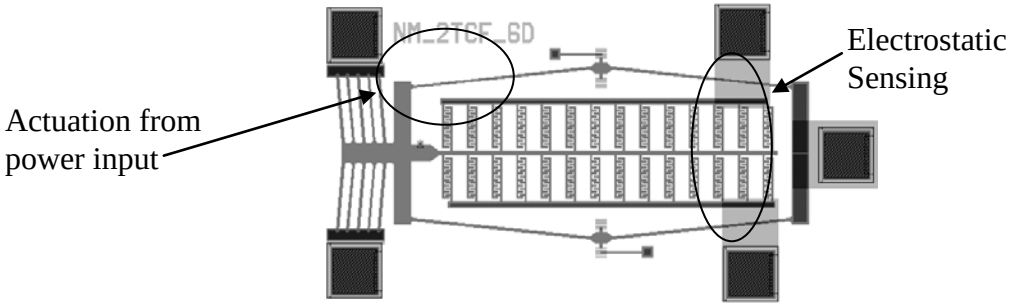

Figure 4.4: Thermally-actuated MEMS

The power input to the system is known, thus a method for quantifying the output from the system is done by electrostatic, or capacitance, sensing for the displacement of the structure, which is detailed by Reissman et al. [28]. The design in Figure 4.4 allows for quick TF analysis to be performed on the system and position feedback control for the longitudinal direction to be implemented. A block diagram for this control scheme is shown in Figure 4.5.

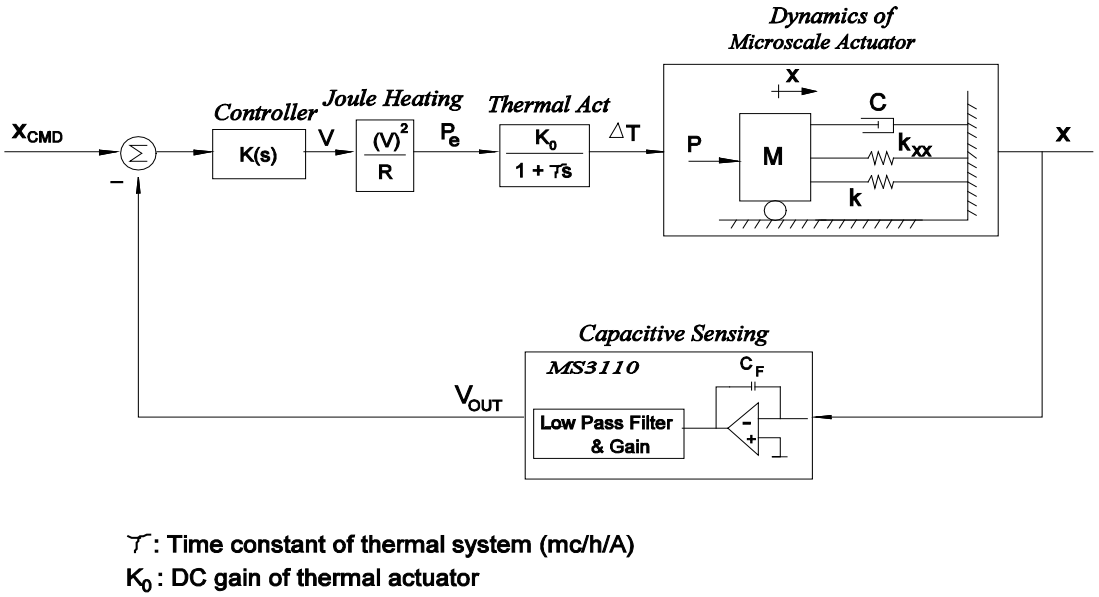

Figure 4.5: Position control using thermal actuation TF

An estimation of the force transmitted by the thermal actuation can be done using Equation (27), where the force is proportional to the temperature difference as prescribed by the profile in Figure 4.2, see Figure 4.6. An important consideration is that while an increase in power will result in an increase in the unidirectional force, it will also result in an increase in temperature, which should be limited to operate in the linear range, or below the recrystallization temperature. To prove this point, Figure 4.7 illustrates the failure of a thermal actuation drive due to melting. The onset of failure can be observed by the change in the refraction of the actuator induced by stress and the resultant buckling, with eventual failure by means of a flash burning and charring at the location of the actuator's highest temperature, approximately the 60% mark along 2L, the total length.

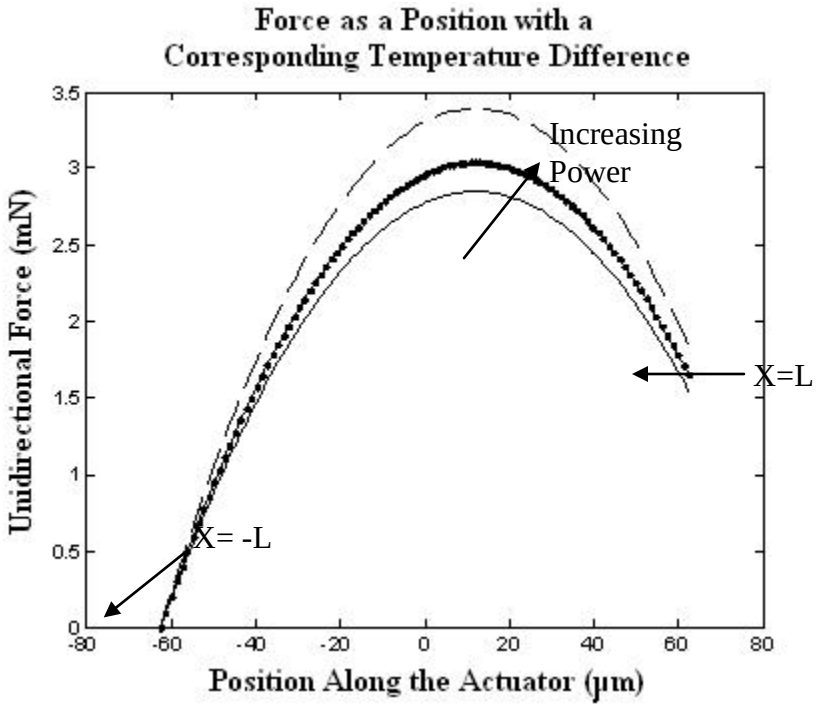

Figure 4.6: Parabolic temperature profile leads to corresponding profile for force

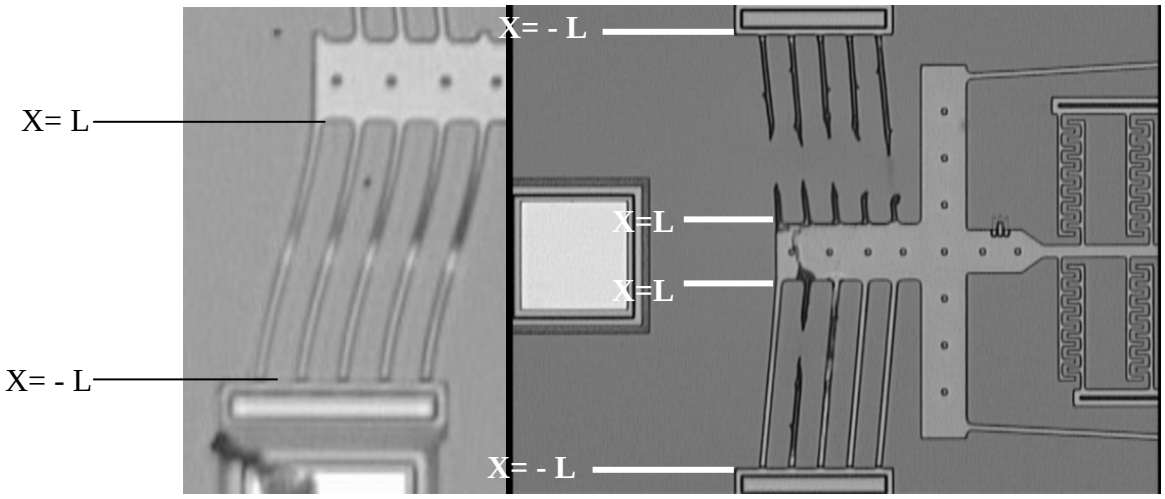

Figure 4.7: Thermal failure of a MEMS actuator along 60% of length

Another important consideration if the objective is to control the system is the time it takes for the thermal actuators to achieve their steady-state temperature profiles. This time is critical for applications pertaining to how quickly the thermal actuator will achieve their desired temperature and what sampling frequencies are necessary in order to monitor and control precise motion of

the actuators. As shown previously, the steady-state time is a function of material properties and geometry. Figure 4.8 shows that as the length of a polysilicon actuator is increased, the steady-state time follows closely to a quadratic function, up until the length decreases to 20μm or less. An issue that quickly arises from Figure 4.8 is obtaining data at fast enough sampling times with decreasing length scales.

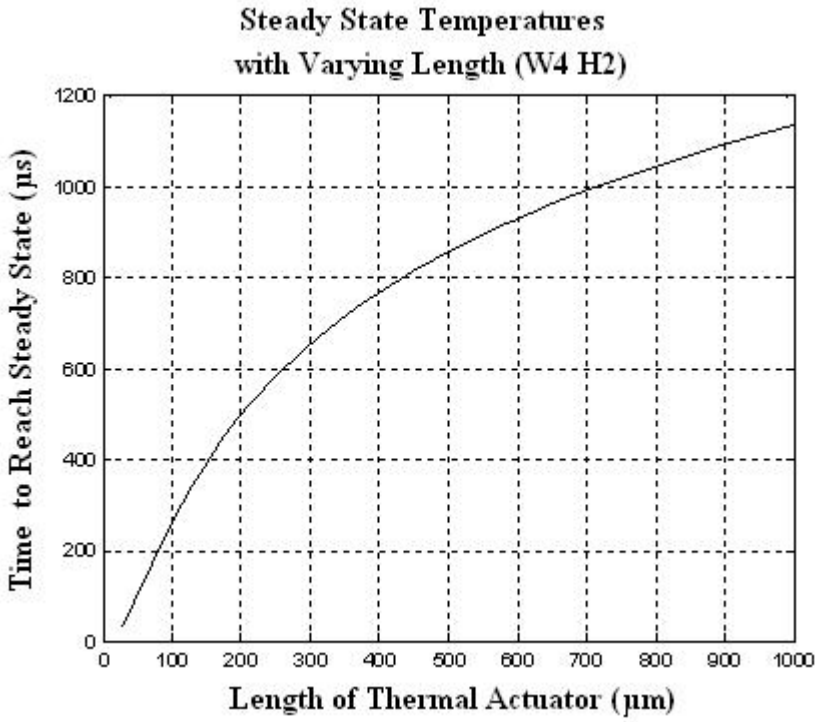

Figure 4.8: Time to reach steady-state as a function of actuator length

Lastly, large motions are typically desired with MEMS devices. However since most thermal devices have a limited operating range with respect to temperature, and are coupled with relatively low thermal expansion coefficients, the need arises for displacement amplification methods to be imposed, solutions include geometry configurations and flexures. Details about such configurations and flexures can be found in Garcia et al. [29-32]. A brief overview of the purpose for flexures is provided here. The intent of using flexures is to create a relative variation in stiffness from one principal axis to another, i.e. allow deflection to be induced with less force

for one direction over another. Thus compliances are given to model the displacement for given force inputs. As an example, in Figure 4.4 the linear drive in the longitudinal direction is connected to a beam that will displace in the transverse direction by means of a flexure hinge, see Figure 4.9 for the model representation.

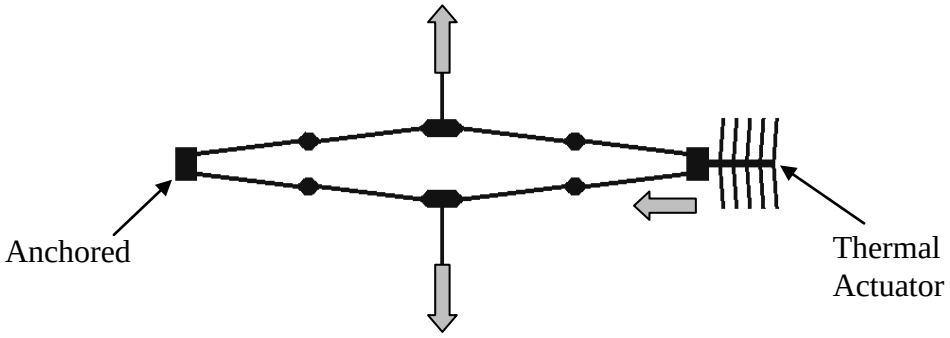

Figure 4.9: MEMS device with flexures for displacement amplification

In conclusion, the mathematical model correlates well with experimental results when adding the stiffness of the system to calculate for displacement of the MEMS device, as is observed in Figure 4.10. Each line with '+', 'o', and 'x' in Figure 4.10 represents the longitudinal displacement of slightly variant MEMS devices, such as the one shown in Figure 4.4. The solid line is the theoretical travel in the x-direction for a given electric potential using the mathematical model. The discrepancies from the model can be hypothesized by those detailed in [28], which include Coulomb friction of the moving structure against the substrate, deflection of the structure out of plane by residual stress, adhesion of the moving structure to the substrate due to an attraction to water after the removal of the sacrificial oxide layer, etc.

The rigorous modeling of the thermal TF was conducted to address how each of the loss terms are placed in the model for thermal actuation, as well as provide a means in which to quantify these losses. Higher accuracy is then achievable with this model for determining the temperature variation in the thermal actuator, which results in an output force. While this model follows a

continuum analysis, experimental results for micro-scale actuation on the scale of a few microns still appears to be valid, as seen in Figure 4.10. Key findings in this research include an extension of the

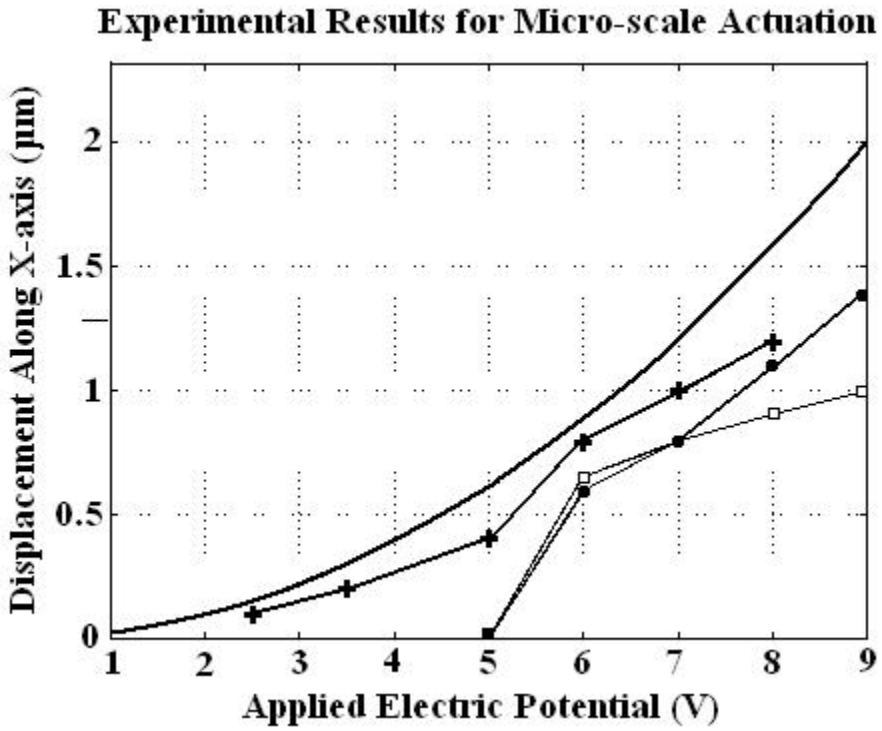

Figure 4.10: Experimental results for micro-scale actuation

Rayleigh number to ranges below the macro-scale realm, the noted importance of the medium in which the MEMS device is immersed in with respect to the convective loss, the limitations of the operating range of a thermal actuator, and the bandwidth in which thermal actuation occurs on MEMS devices.

REFERENCES

[1] C.H. Mastrengelo, "Thermal Applications of Microbridges," Ph.D. Dissertation, U.C. Berkeley, (1991)

[2] L. Lin, "Electrothermal Responses of Lineshape Microstructures," *Sensors & Actuators*, **55**, p. 35-41, (1996)

[3] C.D. Lott, T.W. McLain, J.N. Harb, L.L. Howell, "Modeling the Thermal Behavior of a Surface-micromachined Linear-displacement Thermomechanical Microactuator," *Sensors & Actuators: A. Physical*, **101**, 1-2, p. 239-250, (2002)

[4] M. Ehmann, P. Ruther, M. von Arx, O Pau, "Operation and short-term drift of polysilicon-heated CMOS microstructures at temperatures up to 1200 K," *J. Micromechanics and Microengineering*, **11**, 4, p. 397-401, (2001)

[5] F.P. Incropera, D.P. Dewitt, "Introduction to Heat Transfer," 3rd Edition, Wiley Publications, (1996)

[6] E. Fried, "Thermal Conduction Contribution to Heat Transfer at Contacts," in R.P. Tye, Ed., *Thermal Conductivity*, Academic Press, London, **2**, (1969)

[7] J.C. Eid, V.W. Antonetti, "Small Scale Thermal Contact Resistance of Aluminum against Silicon," in C.L. Tien, V.P. Carey, J.K. Ferrel, Eds., *Heat Transfer*, **2**, p. 659-664, (1986)

[8] B. Snaith, P.W. O'Callaghan, S.D. Probert, "Interstitial Materials for Controlling Thermal Conduction across Pressed Metallic Contacts," *Applied Energy*, **16**, p.175, (1984)

[9] M.M. Yokanovich, "Recent Developments in Thermal Contact, Gap, and Joint Conductance Theories and Experiment," in C.L. Tien, V.P. Carey, J.K. Ferrel, Eds., *Heat Transfer*, **1**, p. 35-45, (1986)

[10] C.S. Pan, W. Hsu, "An electro-thermally and laterally driven polysilicon microactuator," *J. Micromechanics and Microengineering*, **7**, p. 7-13, (1997)

[11] W.H. McAdams, "Heat Transmission," 3rd edition, Chapter 7, McGraw-Hill, (1954)

[12] R.J. Goldstein, E.M. Sparrow, D.C. Jones, "Natural Convection Mass Transfer Adjacent to Horizontal Plates," *Int. J. Heat Mass Transfer*, **16**, 1025, (1973)

[13] O.A. Saunders, "The Effect of Pressure Upon Natural Convection in Air," *Proc. of the Royal Society of London, Series A, Mathematical and Physical Sciences*, **157**, 891, p. 278-291, (1936)

[14] C.Y. Warner, V.S. Arpaci, "An Experimental Investigation of Turbulent Natural Convection in Air at Low Pressure Along a Vertical Heated Flat Plate," *Int. J. Heat Mass Transfer*, **11**, p. 397-406, (1968)

[15] F.J. Bayley, "An Analysis of Turbulent Free Convection Heat Transfer," *Proc. Inst. Mech. Eng.*, **169**, p. 361, (1955)

[16] R.J. Goldstein, E.M. Sparrow, D.C. Jones, "Natural Convection Mass Transfer Adjacent to Horizontal Plates," *Int. J. Heat Mass Transfer*, **16**, p. 1025, (1973)

[17] E.R. Eckert, T.W. Jackson, "Analysis of Turbulent Free-Convection Boundary Layer on Flat Plate," *NACA Report*, **1015**, p. 255-261, (1951)

[18] T. de Karman, L. Howarth, "On the Statistical Theory of Isotropic Turbulence," *Proc. of the Royal Society of London, Series A, Mathematical and Physical Sciences*, **164**, 917, p. 192-215, (1938)

[19] E. Pohlhausen, "The exchange of heat between solids and liquids with less friction and less heat conduction," *J. Applied Math and Mechanics*, **1**, p. 115-121, (1921)

[20] W.M. Kays, M.E. Crawford, "Convective Heat and Mass Transfer," McGraw-Hill, (1980)

[21] S.W. Churchill, "Combined Free and Force Convection Around Immersed Bodies," in E.U. Schlunder, Ed., Heat Exchanger Design Handbook, Sect. 2.5.9-10, (1983)

[22] T.S. Chen, B.F. Armaly, S. Kakac, R.K. Shah, W. Aung, "Handbook of Single-Phase Convective Heat Transfer," Chap. 14-15, Wiley-Interscience, New York, (1987)

[23] F.P. Incropera, A.J. Knox, J.R. Maughan, "Mixed Convection Flow and Heat Transferring Entry Region of a Horizontal Rectangular Duct," *J. Heat Transfer*, **109**, p. 434, (1987)

[24] J.R. Maughan, F.P. Incropera, "Mixed Convection Heat Transfer for Airflow in a Horizontal and Inclined Channel," *Int. J. Heat Mass Transfer*, **30**, p. 1307, (1987)

[25] D.G. Osborne, F.P. Incropera, "Laminar, Mixed Convection Heat Transfer for Flow Between Horizontal Parallel Plates with Asymmetric Heating," *Int. J. Heat Mass Transfer*, **28**, p. 207, (1985)

[26] D.G. Osborne, F.P. Incropera, "Experimental Study of Mixed Convection Heat Transfer for Transitional and Turbulent Flow Between Horizontal, Parallel Plates," *Int. J. Heat Mass Transfer*, **28**, p. 1337, (1985)

[27] S.D. Senturia, "Microsystem Design," Kluwer Academic Publishers, (2003)

[28] T. Reissman, E. Garcia, N. Lobontiu, Y. Nam, "Integrated Electrostatic Micro-Sensors for the Development of Modeling Techniques of Defects in the Actuation of Large Micro-electromechanical Systems (MEMS)," *Proc. of SPIE Microlithography*, (2006)

[29] E. Garcia, N. Lobontiu, Y Nam, "Architectures for Integration of Cellular Microscale Actuator Arrays," *Proc. of ASME IMECE*, (2003)

[30] E. Garcia, N. Lobontiu, Y. Nam, "Tuning the Static and Modal Response of Microcantilevers Through Lumped-Parameter Model-Based Design," *Proc. of ASME IMECE*, (2003)

[31] N. Lobonitu, E. Garcia, "Two Microcantilever Designs: Lumped Parameter Model for Static and Modal Analysis," *J. MEMS*, **13**, p. 41-50, (2004)

[32] N. Lobontiu, "Compliant Mechanisms: Design of Flexure Hinges," CRC Press, (2002)

This chapter originally appeared as:

Reissman, T., Lobontiu, N., Nam, Y., and Garcia, E. "Transfer Function Identification of Thermally-Actuated MEMS with Full Heat Transfer Analysis," *Journal of Micro and Nanosystems*, (submitted).